Optical Dislocations
and
Quantum Entanglement

Sumant S. R. Oemrawsingh

Optical Dislocations and Quantum Entanglement

PROEFSCHRIFT

ter verkrijging van
de graad van Doctor aan de Universiteit Leiden,
op gezag van de Rector Magnificus Dr. D. D. Breimer,
hoogleraar in de faculteit der Wiskunde en
Natuurwetenschappen en die der Geneeskunde,
volgens besluit van het College voor Promoties
te verdedigen op woensdag 15 september 2004
klokke 16.15 uur

door

Sumant Sukdew Ramanujan Oemrawsingh

geboren te Paramaribo, Suriname
op 12 juni 1977

By hundreds and then by thousands, behold, Arjuna, my manifold celestial forms of innumerable shapes and colours.

Behold the gods of the sun, and those of fire and light; the gods of storm and lightning, and the two luminous charioteers of heaven. Behold, descendant of Bharata, marvels never seen before.

See now the whole universe with all things that move and move not, and whatever thy soul may yearn to see. See it all as One in me.

Krishna, The Bhagavad Gita (11.5–7)

Aan de nagedachtenis van mijn vader
Aan mijn moeder

Contents

CHAPTER 1

Introduction

1.1   Optical dislocations

In 1974, John Nye and Michael Berry described dislocations in optical beams in a way that is almost equivalent to that used for dislocations that can occur in crystal structures [1]. There exist two types of dislocations. The first is the screw dislocation, named after the screw topology of the wavefronts. The second is the edge dislocation, that possesses the topology of two half-planes that are joined discontinuously, resulting in an infinitely long dislocation line or edge. Analogous to dislocations in crystals, an edge dislocation can also end in a screw dislocation, resulting in the so-called mixed screw-edge dislocation.

Optical modes with such dislocations can, as indeed any paraxial mode, be described as a superposition of the so-called Laguerre-Gauss modes. Many of these modes contain a screw dislocation or vortex at their centre. In 1992, Robert Spreeuw realised that the screw topology of the wavefronts causes the momentum density to possess an azimuthal component and that these beams therefore carry orbital angular momentum, a concept that is valid even on the single-photon level [2–4]. The quantum-mechanical orbital angular momentum operator has a discrete eigenvalue spectrum from $-\infty$ to ∞; the Laguerre-Gauss modes are eigenmodes of the orbital angular momentum operator.

Generation of orbital angular momentum is thus easily realised by imprinting a screw dislocation on a beam. The precise value of the orbital angular momentum that is obtained depends on many parameters of the experimental setup, as is discussed in this thesis. A more important point that will be discussed is the imprinting of a screw-edge dislocation. When a mode function contains a mixed screw-edge dislocation, it is described by an infinite number of orbital angular momentum eigenstates and as such lives in an infinite dimensional Hilbert space [5]. The resulting orbital angular momentum expectation value can assume *any* real value, i.e. integer and non-integer. The infinite dimensionality of the Hilbert space is of great

interest in the field of quantum information.

1.2   Quantum entanglement

In 1935, Albert Einstein, Boris Podolsky and Nathan Rosen (EPR) formulated a Gedanken-experiment to demonstrate the incompleteness of quantum mechanics [6]. They proposed that if two physical systems, such as photons, at some point in time interact with respect to a certain observable, the systems will become strongly correlated with respect to that observable. Although the value of the observable in each system is intrinsically undetermined, the *relation* between the values of the observable in the systems is correlated. This is fundamentally different from classical correlations, where the value of the observable in each system is already determined. After the two systems have moved away from each other, the strong, non-classical correlation still exists. A local measurement of the observable of one system must be a direct measurement on the other system according to quantum mechanics, regardless of the physical distance between the systems. According to EPR, this so-called spooky action at a distance ('spukhafte Fernwirkungen') can only be explained by assuming that quantum mechanics does not describe the full physical reality, as locality is violated; it has been theorised that there exist hidden variables whereby the non-locality is resolved.

In 1964, John Bell formulated a mathematical inequality to test the existence of these hidden variables, which is violated when there is no local theory that can describe a quantum experiment on such a so-called EPR pair of systems [7]. Since then, the experiment has been performed many times, most notably on an EPR pair of photons entangled with respect to their polarisation. Such a pair is obtained via the nonlinear optical effect of spontaneous parametric down-conversion. Violation of Bell's inequality has been conclusively established in many experiments [8].

The possible polarisations of a photon span a two-dimensional Hilbert space, consisting of, for example, horizontal and vertical polarisation. Both theory and experiment indicate that the entanglement of an EPR pair, i.e. its non-locality, can be stronger when entanglement is obtained for a high-dimensional property [9, 10]. A practical implementation of this idea suffers from an important drawback: the setup becomes much more complicated since cross-correlations between many analysers and detectors are required.

The final aim of the work described in this thesis is to investigate high-dimensional entanglement of photons, *without* increasing the complexity of the setup, by making use of the high-dimensionality of the orbital angular momentum Hilbert space through mixed screw-edge dislocations. To facilitate this, a great deal of the work focuses on the creation of optical dislocations and their connection to orbital angular momentum. A short outline of the work presented in this thesis is as follows.

- Chapter 2 describes a new setup to measure the transverse wave-vector correlations of twin photons that are produced in spontaneous parametric down-conversion. This scheme uses an intensified CCD camera as detection device as opposed to the traditional two point-detectors. Although the correlations are successfully established, the method does not provide enough information to truly analyse the orbital angular momentum state of the detected photon and establish entanglement.

- Chapter 3 provides a short overview of the subject of optical orbital angular momentum caused by screw dislocations. It starts with the description in paraxial optics and the Laguerre-Gauss laser modes, and briefly introduces orbital angular momentum in the quantum regime.

- Chapter 4 discusses how a device that imprints an *integer* vortex charge can be used to generate *non-integer* orbital angular momentum, i.e. a high-dimensional superposition of orbital angular momentum states. This is achieved by repositioning the device in the incident beam. To this end, the *intrinsic* orbital angular momentum of a laser beam is introduced and described. Experimentally obtained far-field intensity profiles are found to match our numerical calculations.

- Chapter 5 investigates the quality of another type of vortex-imprinting device, the spiral phase plate. With this device, one can generate non-integer orbital angular momentum by imprinting a mixed screw-edge dislocation on an optical beam. Again, far-field intensity profiles are compared to numerical calculations and we find that these devices are well suited for the purpose of generating high-dimensional superpositions of orbital angular momentum modes.

- Chapter 6 stresses the possibility of generating half-integer orbital angular momentum in an optical beam. It is also demonstrated that, after passing a beam through a spiral phase plate and thus acquiring topological complexities, the complementary spiral phase plate can in fact remove that topology again. We test the same spiral phase plates that are used in the last experiment, described in Chapter 8.

- Chapter 7 proposes a setup in which high-dimensional entanglement can be observed without an increasingly complicated detection scheme, predicting a violation of local realism that is stronger than can be achieved by the well-known Bell states. In the simple and elegant scheme that is used for observing the Bell states in polarisation entanglement, the polarisers are replaced with half-integer spiral phase plates.

- Chapter 8 describes the successful experimental implementation of the scheme proposed in Chapter 7 for observing beyond-Bell pairing of photons.

There is some overlap between the chapters, as most of them are in fact published papers. Consequently, the chapters can be read separately.

3

1. Introduction

CHAPTER 2

Two-dimensional wave-vector correlations in spontaneous parametric down-conversion explored with an intensified CCD camera

Utilising a new scheme with a single-photon-sensitive intensified CCD camera and a femtosecond laser, we have measured signal-idler correlations over the full cone of degenerate type-I spontaneous parametric down-conversion, thereby establishing wave-vector correlations in two dimensions. We discuss the key features of the camera that are important for its use in twin-photon correlation measurements.

2.1 Introduction

Quantum-information science is a rapidly developing field encompassing such diverse activities as quantum teleportation, quantum cryptography and quantum computing [11]. The key concept underlying these developments is quantum entanglement. A large fraction of the recent experimental work on quantum entanglement involves the use of entangled photons [12–15]. An important factor here is that entangled states of two photons can rather easily be generated by the second-order nonlinear optical process of spontaneous parametric down-conversion (SPDC). This involves splitting of a photon from a classical pump beam into two new photons, traditionally called signal and idler, while conserving energy and momentum. Another relevant factor is that single-photon detectors with high quantum efficiency are nowadays commonly available. These detectors are then employed in coincidence to record correlations of properties such as time [16], polarisation [11], and angular momentum [17] between the photons of a pair. This correlation can ultimately reveal non-classical effects and quantum entanglement.

For the study of spatially extended correlations, conventional single-photon detectors are not ideal, because they are point detectors, which possess small (typically 175-µm-diameter [18]) active areas, whereas the down-conversion state can have a much more extended spatial profile. A camera consisting of a two-dimensional (2D) array of point detectors offers an obvious advantage here. Specifically, all N pixels of an image can be cross correlated with one another, making one image equivalent to $N(N-1)/2$ measurements with two separate point detectors, which would have to be positioned differently for each measurement.

Such a camera has to possess single-photon sensitivity, sufficient quantum efficiency at the down-conversion wavelength, and a low dark count. The camera does not require coincidence circuitry, since the exposure itself acts as such a circuit; the exposure time therefore has to be as short as possible (of the order of nanoseconds).

Proper use of such a camera guarantees the ability to detect both the signal and the idler photon without any loss of spatial information. The idea of using a single-photon-sensitive camera was first explored by Jost *et al.*, who showed that an intensified charge-coupled device (ICCD) has sufficient sensitivity to register the photons generated in SPDC [19]. Their experiment brought to light the fact that it is not trivial to establish the inherent correlations of the twin photons generated in SPDC with such a camera.

In the present Chapter we show that an ICCD equipped with the newest generation intensifier and a fast gate option is exceedingly well suited for the study of spatial correlations of the photons generated in type-I SPDC. We use this setup to demonstrate the correlations between $\vec{k}_{s\perp}$ and $\vec{k}_{i\perp}$ over the full emission cone of degenerate pairs. Here $\vec{k}_{s\perp}$ and $\vec{k}_{i\perp}$ refer to the transverse components of the wave vectors of signal and idler, respectively.

2.2 Experiment

The objective of the experiment is to pump the down-conversion crystal with a short light pulse and simultaneously gate the ICCD camera's intensifier with a trigger pulse from the laser system. The camera operates as a single-photon-sensitive device only during this gate, which has a minimum length of 2 ns. During this gate time we look at a single photon pair
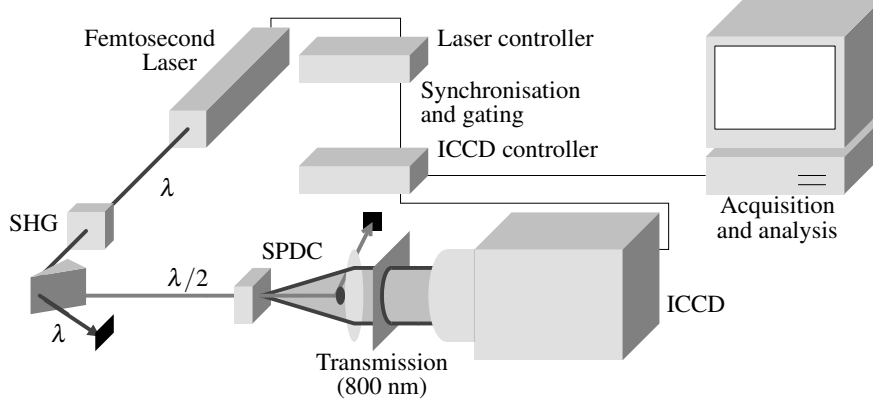
Figure 2.1: *Experimental setup. The key elements are a femtosecond laser and an intensified CCD camera, which are synchronised. The prism symbolises the filtering system used to remove the fundamental (λ) from the frequency-doubled pump ($\lambda/2$). In reality, this system consists of four harmonic separators and two prisms that compensate for one another's space-time distortions on the pump pulse. The filter in front of the camera selects signal and idler photons at or near degeneracy, at wavelength λ. SHG is the second-harmonic generation crystal and SPDC the crystal where the down-conversion process takes place.*

with, in principle, 512×512 single-photon detectors that are all operated in coincidence; the coincidence window is given by the gate time. Assuming that both photons liberate a photo-electron, all that remains is to read out the location of the pixels that they have activated. It is important to realize that the CCD has to be read out before the next photon pair is admitted into the system; this sets the speed of the experiment.

The laser system (see Fig. 2.1) is an amplified titanium-sapphire laser system (Coherent Vitesse-duo and RegA 9000), delivering 250-fs pulses at $\lambda = 800$ nm. The output is frequency doubled in a β-barium borate crystal of 0.5-mm length, after which the 400-nm light is thoroughly separated from the redundant fundamental by the use of four harmonic separators and two Brewster-angled prisms. This filtering scheme is symbolically denoted by a single prism in Fig. 2.1 (lower left). The blue light is then collimated to a spot of ∼2-mm diameter and used to pump a thin (0.5-mm) β-barium borate crystal cut for collinear degenerate type-I down-conversion. The crystal is tilted slightly such that the degenerate pairs do not coincide with the transmitted pump beam but rather come out of the crystal in a cone with a top half-angle of 5°. This cone of degenerate photons is selected by a spectral filter with 13-nm bandwidth, centred at 803 nm, and subsequently brought to a ring-like focus on the photocathode of the intensified CCD camera. A small mirror is attached to the centre of the imaging lens to intercept the pump beam and send it to a laser-beam dump.

The intensified CCD camera (Princeton Instruments PI-MAX 512HQ with 4th-generation intensifier) contains 512×512 pixels with an effective size of 24×24 μm^2 each. It has a GaAs photocathode, which is sensitive in the wavelength range 450–900 nm, and has a specified quantum efficiency of 30% at 800 nm. The dark count of the intensifier and CCD array combined is ∼8 units/(pixel/s). The amplification factor of the intensifier is such that a

single photo-electron generates a charge in a CCD pixel equal to approximately 80 units, well above the read-out noise of ~ 8 units. This allows us to set a discrimination level to impose values of 1 on the pixels that have detected a photon (active pixels) and 0 on the pixels that have not.

The experiment then consists of repetitively firing the laser and, with each shot, capturing the CCD image. Because the repetition rate of the experiment is set by the read-out time of the CCD, we use on-chip binning (5×5). At the expense of spatial resolution, this binning reduces the data stream, thereby speeding up the procedure. Note that binning does not affect our ability to discriminate between activated and non-activated bins of pixels, as the read-out noise per bin is still ~ 8 units. Using this approach, we run the camera at a frame rate of $30 \, \mathrm{s}^{-1}$.

To establish the photon correlations unequivocally it is important to avoid the generation of multiple pairs of photons in a single pump pulse. For this reason the pump energy is attenuated to a value of $\sim 50 \, \mathrm{nJ/pulse}$, corresponding to a generation rate of $\sim 0.1 \, \mathrm{pair/pulse}$ (implying a generation probability of 4.5×10^{-3} for two pairs/pulse and even less for multiple pairs). With an effective quantum efficiency (this value includes losses at various optical elements) of the setup of $\sim 20\%$ this generation rate implies that roughly 1 of every 250 images contains a detected correlated pair. The other images have no active bins, or only one, this bin being half of a generated pair. For this simple argument to apply, both the dark count of the camera and the stray light in the setup have to be so low that, within the gate time, they do not activate a single bin of the array. By intercepting the pump laser we have confirmed that the dark count is negligible. Only 1 out of every $25,000$ images contains an activated bin that is due to dark counts. The reason for this low dark-count rate is of course the short exposure time of 2 ns and the fact that we use a discrimination level. In contrast, stray light is far from negligible; we observe an activated bin approximately once every 100 images, i.e. approximately twice as often as we expect to detect a correlated signal-idler pair. Consequently, we detect pairs consisting of a stray photon and one of the signal-idler pair with somewhat larger probability than a quantum correlated signal-idler pair. The resulting false correlations give rise to substantial background in our data. The non-negligible probability of detecting a stray-light photon has an important additional consequence in that the quantum efficiency of photon detection is not simply related to the ratio of detected correlated pairs to detected singles. Aside from this, the correct quantum efficiency is found only when the number of detected single counts is divided by two, to compensate for the fact that the camera is one device, whereas the point detectors are two separate devices.

2.3 Acquisition, analysis, and results

We acquire approximately 436,000 images, most of which (99.5%) are, as mentioned above, completely empty or contain only one active bin; all these images are discarded. The majority of the remaining images contains only two active bins (see Fig. 2.2(a)). When these images are superposed, they display the well-known type-I down-conversion ring (see Fig. 2.2(b)). Apart from the location of the ring, this composite picture also shows us its width, a consequence of the finite bandwidth of the filter in front of the camera and of the bandwidth of the pump beam. Given the parameters of the setup, this ring thus tells us which bins of the
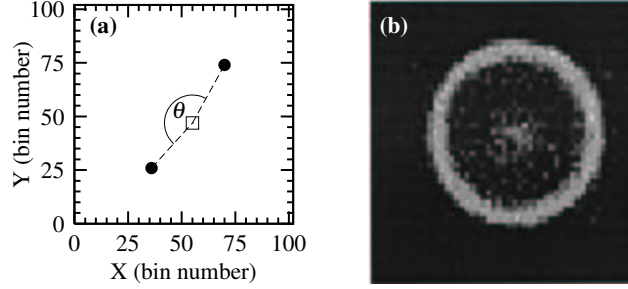
Figure 2.2: *(a) Single CCD frame, showing two active pixels (filled circles) and their relative angle θ subtended at the centre (square) of the type-I down-conversion ring. This centre is determined from (b) the superposition of multiple frames. The type-I down-conversion ring is clearly seen in this superposition of 90,000 single-frame measurements.*

camera can become activated by signal and idler photons. These pixels define a so-called region of interest. This region is useful, as it allows us to concentrate on the images that are relevant for our experiment. In addition, and this is important for further analysis, the composite picture helps to locate the position of the centre of the ring with reasonable accuracy. One does this by determining its centre of intensity, taking into account the statistical fluctuations in the ring.

For each of the relevant images ($\sim$ 0.4% of the original 436,000), we determine the angle θ subtended by the two bins at the centre of the ring (cf. Fig. 2.2(a)) by scanning each image, row by row, starting at the top. When the first active bin is located, the angle between it and the second one is determined in a counterclockwise direction. Thus we obtain angles from $0°$ to $360°$. We then make a histogram of these data as a function of angle θ, as shown in Fig. 2.3(a). The histogram shows a relatively narrow peak at an angle $\theta = 180°$ on top of an approximately constant background. This peak, which is simply a consequence of phase matching in the down-conversion process, has an excellent signal-to-noise ratio and exhibits a width of the order of $1°$, largely determined by diffraction. The constant background is caused mostly by the coincidence of a stray-light photon with a single down-conversion photon, as discussed above.

It is easy to show that a position error of the centre of the down-conversion ring will lead to incorrect values of the signal-idler wave-vector correlation angle θ. In this histogram these data will appear beside the main peak, at the expense of its height, always giving rise to an increased width of the correlation peak. It then follows that it is appropriate to adjust the position of the ring's centre until the correlation peak is at its narrowest. Note that this procedure can be followed only if the initial correlation histogram already shows a well-defined peak, as is the case here. No requirement is made for the value of the angle θ of the peak, its visibility, or its height.

So, to determine the location of the ring's centre accurately, we position the centre on various bins and, for each of these new positions, construct a histogram. We then select the histogram with the narrowest correlation peak, which is shown in Fig. 2.3(b). Compared with the results of Fig. 2.3(a), it indeed shows a narrower correlation peak and, consequently, a
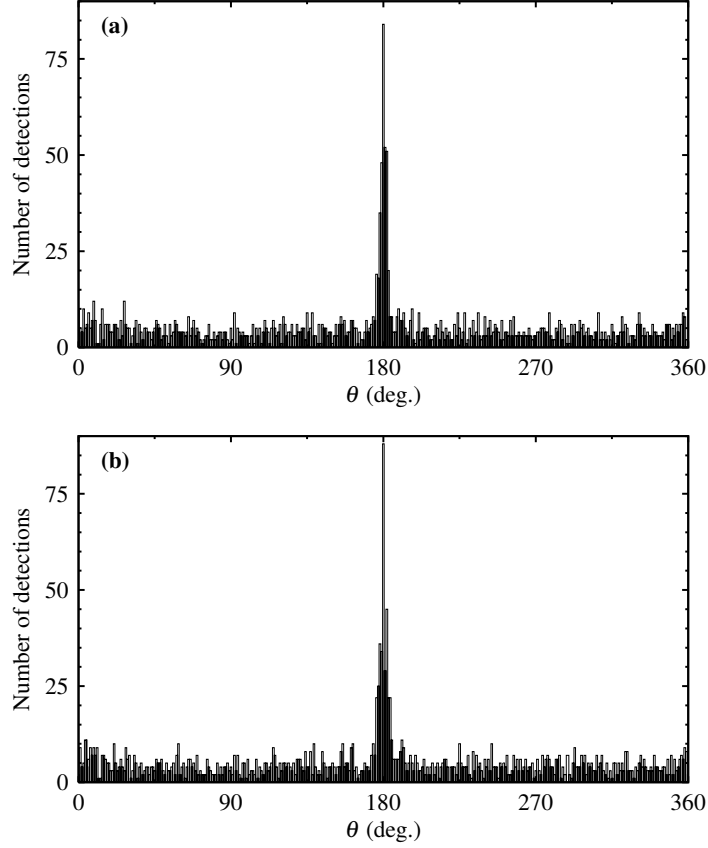
Figure 2.3: *(a) Histogram of angles θ subtended at the centre of the ring by the two photons detected simultaneously and (b) a histogram with a more accurately determined centre, which shows a slight improvement of the signal-to-noise ratio. The sharp peak at* 180° *shows the correlation of the true signal and idler photons. The noise floor is due to detected pairs when one photon originates from stray light.*

somewhat improved signal-to-noise ratio. The difference in position of the centre between the two histograms in Fig. 2.3 is approximately one bin.

Wave-vector correlations in type-I SPDC are not limited to the azimuthal degree of freedom. Wave-vector matching in the down-conversion process also gives rise to correlations of signal and idler photons in the radial coordinate. These radial correlations are, however, effectively washed out in our experiment as a result of the considerable bandwidth of our pump laser.

Figure 2.3, as discussed above, gives a one-dimensional representation of our 2D results. This 2D nature is highlighted in Fig. 2.4, which displays the active bins of all 230 pairs that lie within the central peak of the correlation diagram of Fig. 2.3(b). One observes that the distribution over azimuthal angles is more-or-less constant, as expected for type-I down-conversion. Figure 2.4 is the outcome of many experiments with identically prepared sys-
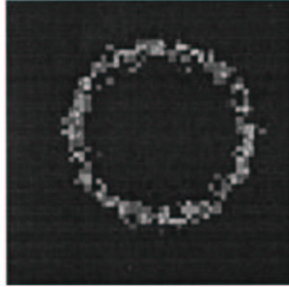
Figure 2.4: *Superposition of pairs that are contained in the narrow peak at 180° of the histogram shown in Fig. 2.3(b), representing the quantum-correlated pairs. Note that they lie evenly distributed over the ring.*

tems, each yielding a wave-vector-correlated photon pair in a plane through the pump beam. Inasmuch as many such planes are involved, it provides a demonstration of the 2D nature of the wave-vector correlation of the quantum state generated in type-I down-conversion.

2.4 Discussion

The results presented above demonstrate that the 2D aspects of degenerate SPDC can be successfully mapped with an ICCD camera and that the underlying signal-idler correlations can be established with excellent signal-to-noise ratio.

The measured coincidence-count rate, however, is much lower than what is nowadays commonly achieved with two point detectors and a coincidence circuit with a coincidence window of several nanoseconds. For instance, Kurtsiefer *et al.* [20] reported a rate of several tens of thousands of correlations per second. The coincidence window in our camera experiment, set by the exposure time, is of a magnitude comparable to theirs. Nonetheless, we measured only 1839 coincidences, of which 230 pairs were true twins, in approximately 4 h. The main cause by far for this huge reduction in the data-collection rate is the recovery time of the camera compared with that of the point detectors. The point detectors can recover from a detection event in less than a microsecond, whereas the camera (and associated computer) takes ~ 30 ms, because of the read-out. Additionally, point detectors have this dead time only after an actual detection event, whereas the camera has a dead time after every measurement. Because roughly 92% of the total amount of images were completely empty, this effect further reduces the collection speed of useful data.

As stated above, however, the camera has the advantage of a large field of view; point detectors need to be mode matched to the output of the crystal for each of the modes that needs to be studied, while the camera needs to be placed properly only once. Mode matching of point detectors is usually done by repositioning at least one of the detectors and the accompanying mode-matching optics, such as a lens or filter; doing so is inconvenient and time consuming.

The multiplex nature of the camera and the ability to integrate over time are aspects of a camera that are often seen as an advantage. The multiplexing advantage appears when

11

there is information in many pixels; in the present case it is of no use because we cannot afford to detect more than a single pair per image. Integration over time in an individual pixel (or bin), which in general is used to enhance a weak signal, is also of no use in our approach, because the signal per bin is either exactly 1 or 0. Integrating over time means an increase of the exposure time which, in essence, would lead to an increased number of dark counts and counts due to stray light, and therefore a higher probability of observing multiple pairs. Thus, both multiplexing and integration are of no use in the approach discussed in the present Chapter. However, we note that, in a related experiment on spatial correlations in down-conversion, which was not at the single-photon level, Jost *et al.* [19] did use both the multiplexing and integrating features of a camera by *a priori* assuming angular correlation between signal and idler photons and then focusing on their radial correlations. In such an approach, only intensity-fluctuation correlations (as opposed to photon correlations) can be studied; it therefore differs fundamentally from the method described here.

Finally, we discuss whether we could also have used a CW laser instead of a pulsed (femtosecond) laser. With such a setup the camera would be gated not by the laser but by a repetitive trigger generator. Obviously, this would not lead to an increased data-collection rate because this rate is entirely determined by the camera and its associated equipment and has nothing to do with the laser or the trigger generator. The question then is whether using a CW laser would result in an even lower data-collection rate, assuming that the trigger generator is not the limiting factor. The crucial quantity then is the pair production rate, which, in the experiment discussed above, is ~ 0.1 pair/exposure, i.e. 5×10^7 pairs/s. Based on the existing literature, we estimate that such a production rate can be realized. For instance, Kurtsiefer *et al.* [20] achieved a coincidence-count rate of 50,000/s by using a 50-mW pump and two point detectors. This would imply the need for a 50-W laser to obtain the required production rate. With a camera setup as opposed to the setup with two point detectors, however, photons in the entire down-conversion cone can be detected. Thus compensating for this by assuming that the generation rate is in fact ~ 25 times their coincidence-count rate, we find that a 2-W CW laser would be sufficient. When a CW laser is used, the overwhelming majority of the twin photons is generated during the read-out time (30 ms), but these photons go undetected, because the intensifier is turned off during the read-out. Assuming the detection of stray light can be sufficiently suppressed, we find that the experiment might also have been done with a CW laser. An advantage of that approach is that the narrow bandwidth of the pump would enable us also to observe radial correlations, and the noise may be reduced, since fluorescence and other nonlinear phenomena in our optics would be less likely to occur.

2.5   Summary and conclusions

In summary, we have shown that an intensified charge-coupled device camera with a fast-gate option provides an attractive detection system for observing spatially extended correlations of signal and idler photons in spontaneous parametric down-conversion. The measured signal-to-noise ratio is excellent, yielding results comparable in quality with those of experiments done with two discrete detectors. Such detectors do allow for much higher acquisition rates (of the order of a few megahertz), but a study of spatially extended correlations over the full detection plane with such detectors demands that the experiment be repeated for many

different positions of both detectors; to do this would be, in general, inconvenient and time consuming, thereby greatly lowering the effective acquisition rate. The basic advantage of the ICCD camera is that the mechanical scanning of two point detectors is replaced by the electronic read-out of the CCD pixels, but one must be willing to forgo a high acquisition speed.

Acknowledgements

CHAPTER 3

Orbital angular momentum of light

In this Chapter, we provide a brief overview of optical orbital angular momentum. The Laguerre-Gauss laser modes, that provide a convenient way of describing laser beams carrying orbital angular momentum, are introduced. Several generation techniques are discussed and finally, we briefly introduce the orbital angular momentum of light in the quantum regime.

The fact that electromagnetic radiation carries momentum is well known. Its linear momentum is associated with radiation pressure, and has many applications from fundamental physics to the applied sciences [21–24]. The angular momentum of electromagnetic radiation is usually associated with the polarisation of the optical beam. The transfer of this (spin) angular momentum of light to a material body has been measured in a landmark experiment by Beth [25] in the 1930's. More recently, it has been realised that the spatial structure of a paraxial beam can also give rise to angular momentum [2]. This orbital angular momentum (OAM) has attracted considerable attention over the past decade (for a recent review, see Ref. [26]). The transfer of the optical OAM of a light beam to a physical body has also been demonstrated, in experiments where small particles were brought into an orbiting motion [27, 28]. Recently, the OAM of beams has come under renewed scrutiny in the field of solitons [29, 30] and studies at the quantum level [17, 31, 32].

In this Chapter, a brief review of the orbital angular momentum of light is presented within the paraxial approximation. We shall restrict ourselves to cases where the optical OAM per energy quantum is equal to an integer times $\hbar$ (cf. Eq. (3.13)). The Laguerre-Gauss modes, which provide a convenient basis for describing beams containing orbital angular momentum, are discussed, as well as generation methods and some properties of the generated fields. Finally, OAM in the quantum regime will be briefly introduced.

3.1 The orbital angular momentum of a classical optical field

The orbital angular momentum of a system of massive, i.e. not massless, particles is well known. In a collection of massive particles, the total angular momentum density is defined by the pseudo-vector

$$\vec{j}(\vec{r}) = \vec{r} \times \vec{p}(\vec{r}),\tag{3.1}$$

where $\vec{r}$ is the vector (r, θ, z) from the chosen origin around which the total angular momentum density is measured to the point under consideration, and $\vec{p}(\vec{r})$ is the linear momentum density at that point. This angular momentum density can be separated into two parts when integrated over the volume of the system,

$$\begin{aligned}\vec{J} &= \int \vec{j}(\vec{r})d\vec{r} \\ &= \vec{L} + \vec{S},\end{aligned}\tag{3.2}$$

where $\vec{L}$ is the external and $\vec{S}$ is the internal angular momentum. The former is the orbital angular momentum associated with the motion of the particles around the origin, whereas the latter is called the spin angular momentum, reflecting the spinning motion of each particle about its centre of mass. When a particle is considered in its rest frame, its external momentum vanishes. When all internal and external forces in the system are central, the total angular momentum $\vec{J}$ is conserved.

The total angular momentum density for a transverse monochromatic electromagnetic field in vacuum averaged over a period, can be similarly defined [2],

$$\vec{j}(\vec{r}) = \vec{r} \times \vec{p}(\vec{r}) = \varepsilon_0 \vec{r} \times \left[\langle \vec{E}(\vec{r},t) \times \vec{B}(\vec{r},t) \rangle \right],\tag{3.3}$$

where $\vec{E}, \vec{B}$ are the electric and magnetic fields, respectively. In the absence of charged particles the total angular momentum is a conserved vector quantity [33], because of the invariance of the free Maxwell equations under spatial rotations. However, a separation as made for massive particles in Eq. (3.2), is in general impossible for electromagnetic radiation, as this would violate the transversality of the field [4, 34].

3.1.1 Paraxial beams

When the electromagnetic field is paraxial, e.g. a conventional laser beam, the field has a well-defined linear momentum (small transverse spread). Then, the separation of the total angular momentum along the propagation axis z into spin and orbital components does *not* violate transversality, so that

$$J = L + S, \tag{3.4}$$

where the z-components of the total angular momentum, the OAM and the spin momentum, respectively, are implied. Both L and S are now invariant under free-space propagation. For such a beam with a uniform polarisation described by the complex transverse unit vector $\vec{\sigma}$, we write the electric field (in cylindrical coordinates) as

$$\vec{E}(\vec{r}, t) = \vec{\sigma} u(\vec{r}) \exp(ikz - i\omega t) + c.c. \tag{3.5}$$

Here, the complex function $u(\vec{r})$ describes the field amplitude distribution in the paraxial approximation [2, 35]. For the z-component of the total angular momentum, only a single transverse plane needs to be considered, due to conservation during free-space propagation. We choose the plane $z = 0$ and separate the modulus and the phase factor, so that

$$u(\vec{\rho}) = \tilde{u}(\vec{\rho}) \exp[i\chi(\vec{\rho})], \tag{3.6}$$

where $\vec{\rho}$ is the transverse position vector, $\chi(\vec{\rho})$ is a slowly varying phase distribution and $\tilde{u}(\vec{\rho})$ is real. The *transverse* momentum density in that plane becomes [2]

$$\vec{p}(\vec{\rho}) = \frac{\varepsilon_0}{i\omega} \left[u^*(\vec{\rho}) \vec{\nabla} u(\vec{\rho}) - c.c. \right] - \frac{\varepsilon_0}{i\omega} \left(\hat{z} \times \vec{\nabla} \right) |u(\vec{\rho})|^2 (\vec{\sigma}^* \times \vec{\sigma})_z, \tag{3.7}$$

where $\vec{\nabla}$ is the transverse gradient operator, ω is the frequency of the optical field and $\hat{z}$ is a unit vector along the z-direction. In Eq. (3.7), the first term depends only on the gradient of the slowly varying phase $\chi(r, \theta)$ of the field (Eq. (3.6)). This gradient has transverse components that give rise to transverse optical momentum. The second term depends on the polarisation of the light and is completely phase independent. The z-component of the total angular momentum density can now be obtained by substituting Eq. (3.7) in Eq. (3.3).

As we are interested in paraxial beams, for which the z-component of the total *angular* momentum is separable, the last term in Eq. (3.7) is irrelevant, as follows from Eq. (3.3). For the paraxial mode functions u of Eq. (3.6), the z-component of the total angular momentum density $\vec{j}$ in the point $(\vec{\rho}, 0)$ becomes [2]

$$j_z(\vec{\rho}) = 2\frac{\varepsilon_0}{\omega} |u(\vec{\rho})|^2 \frac{\partial\chi}{\partial\theta} - \frac{\varepsilon_0}{i\omega} \left(\vec{\rho} \cdot \vec{\nabla} \right) |u(\vec{\rho})|^2 (\vec{\sigma}^* \times \vec{\sigma})_z. \tag{3.8}$$

Integration over the transverse plane then yields the z-component of the total angular momentum per unit length, J. The appearance of $\vec{\sigma}$ in the second term betrays its association with spin, i.e. with polarisation; this term will not be discussed here. The first term depends on the gradient of the slowly varying transverse phase distribution. After integration over $\vec{\rho}$, it can be considered as the z-component of the orbital angular momentum per unit length, L. This component, in general referred to as the optical OAM, is equal to

$$L = 2\frac{\varepsilon_0}{\omega} \int |u(\vec{\rho})|^2 \frac{\partial \chi}{\partial \theta} \, \mathrm{d}\vec{\rho}. \tag{3.9}$$

The transverse density of 'energy quanta' ($\hbar\omega$) of this field in the plane $z = 0$ is equal to the transverse energy density of the field, divided by the quantum of energy,

$$n(\vec{\rho}) = \frac{2\varepsilon_0 |u(\vec{\rho})|^2}{\hbar\omega}. \tag{3.10}$$

The average optical OAM per energy quantum becomes

$$\hbar \int \frac{\partial \chi}{\partial \theta} n(\vec{\rho}) \mathrm{d}\vec{\rho} \left/ \int n(\vec{\rho}) \mathrm{d}\vec{\rho} \right. \tag{3.11}$$

When the field function u in the plane $z = 0$ is given by

$$u(\rho) = \tilde{u}(\rho) \exp(i\ell\theta), \tag{3.12}$$

with $\tilde{u}$ a real function and ℓ integer, the optical OAM per energy quantum according to Eq. (3.11) will become

$$\hbar \frac{\int \ell n(\vec{\rho}) \mathrm{d}\vec{\rho}}{\int n(\vec{\rho}) \mathrm{d}\vec{\rho}} = \ell\hbar, \tag{3.13}$$

and is, as such, characterised by the number ℓ. Actually, the field described by Eq. (3.12) possesses a vortex at the origin; its charge Q is given by [36]

$$Q = \frac{1}{2\pi} \oint \mathrm{d}\vec{l} \cdot \vec{\nabla}\chi, \tag{3.14}$$

taken along a closed path $\vec{l}$ around the vortex where the phase χ of the field is analytical, yielding a value of ℓ. Note that the vortex charge needn't be conserved during free-space propagation [37]. In Fig. 3.1 the phase fronts for three different ℓ values are shown. The first is for $\ell = 0$, showing a plane phase distribution. The second shows a helix, the phase front for $\ell = 1$. This field is said to have a screw dislocation, as is obvious from its appearance. The strength of this dislocation is equal to ℓ, in this case unity. The average OAM contained in the field is $\hbar$ per energy quantum. The rightmost phase fronts represent the case where $\ell = 1/2$. This field contains a mixed screw-edge dislocation and carries an average OAM per energy quantum equal to $\hbar/2$. Such fields shall be discussed in Chapters 5 through 8. Throughout the rest of the present Chapter, we will only consider fields with integer values of ℓ. Note that Eq. (3.9) allows for field functions that do not contain a vortex, i.e. different from Eq. (3.12), while still carrying OAM. Such fields will *not* be discussed here, but have been studied by Courtial *et al.* [38].
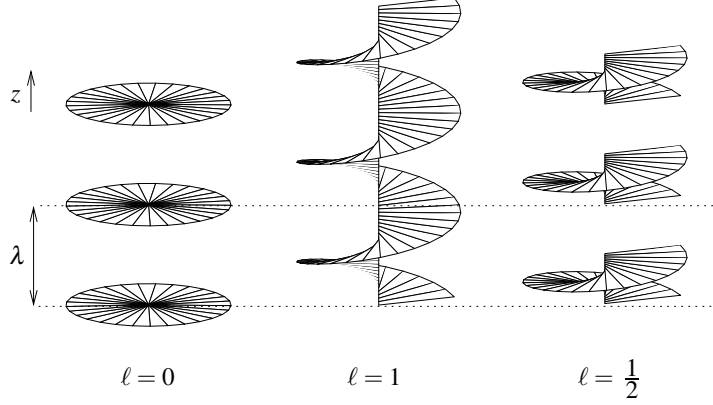
$\ell = 0$ $\qquad$ $\ell = 1$ $\qquad$ $\ell = \frac{1}{2}$

Figure 3.1: *Schematic figure showing iso-phase surfaces in three light beams, characterised by $\ell = 0$, $\ell = 1$ and $\ell = 1/2$. The first shows a plane phase distribution, only reaching the same phase after one wavelength of propagation. The second shows a helical structure, and demonstrates why such fields are said to possess a screw dislocation. The last picture shows the iso-phase surfaces for a field with a non-integer screw-dislocation strength.*

3.1.2 Intrinsic orbital angular momentum

When dealing with a massive point particle, the spin angular momentum is generally regarded as the intrinsic angular momentum, as it is the only non-vanishing angular momentum in the rest frame of the particle. The OAM of such a particle is usually considered extrinsic, meaning that its value depends on the choice of frame of reference.

The distinction between spin and orbital angular momentum that holds for massive point particles, namely the respective independence and dependence on the choice of origin, does not apply to paraxial beams. The spin angular momentum for paraxial beams is defined as their polarisation, while the orbital angular momentum depends on the spatial structure of the beam [39]. As such, it is possible for paraxial beams to possess an intrinsic OAM, i.e. an amount of OAM that does *not* vanish in the rest frame. A full explanation can be found in Chapter 4.

Interestingly, the occurrence of intrinsic optical OAM in paraxial beams does *not* require the construction of pathological beams. For instance, *all* modes of the natural basis for optical OAM, the Laguerre-Gaussian modes which will be discussed in the following subsection, possess intrinsic optical OAM. Using such Laguerre-Gauss beams, intrinsic optical OAM has been studied in experiments with particles trapped off-axis in optical tweezers [40].

3.1.3 The Laguerre-Gauss basis

A proper basis for a description of optical OAM in paraxial beams is provided by the Laguerre-Gauss modes, a complete orthonormal set of eigenmodes of the paraxial wave equation [41].
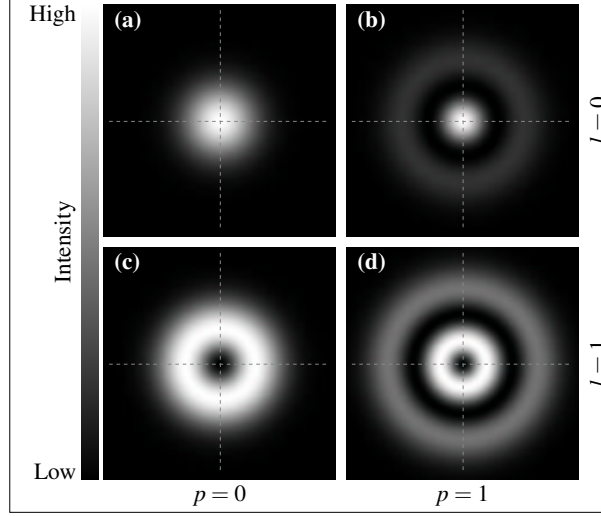
Figure 3.2: *Intensity profiles of four Laguerre-Gauss modes, illustrating their appearance. Each picture has been peak-normalised to enhance contrast. The profiles of the modes that contain orbital angular momentum, (c) and (d), have a dark centre.*

The general mathematical structure of such a mode is given by [2]

$$
\begin{aligned}
u_{lp}^{\mathrm{LG}}(r,\theta,z) = & \frac{C}{\sqrt{1+z^2/z_R^2}} \left[\frac{r\sqrt{2}}{w(z)}\right]^{|l|} L_p^{|l|} \left[\frac{2r^2}{w^2(z)}\right] \exp\left[\frac{-r^2}{w^2(z)}\right] \\
& \times \exp\left[\frac{ikr^2 z}{2\left(z^2+z_R^2\right)}\right] \exp\left(il\theta\right) \exp\left[-i\left(2p+l+1\right)\arctan\frac{z}{z_R}\right],
\end{aligned}
\tag{3.15}
$$

where z_R is the Rayleigh range of the beam, $w(z)$ the beam radius, $L_p^l(x)$ an associated Laguerre polynomial and C a normalisation constant. The indices l and p provide information about the OAM of the beam, and the number of off-axis radial nodes of the associated intensity profile, respectively. As a consequence of the phase factor $\exp(il\theta)$, the modes carry an OAM per photon equal to $l\hbar$, and, as such, also contain a helical phase structure as shown in the middle of Fig. 3.1 for the case $\ell = 1$. Thus the LG-mode index l is equal to the general OAM parameter ℓ. Several LG-mode intensity profiles are displayed in Fig. 3.2 to illustrate the meaning of the two indices. Note in particular that the modes with index $l = 1$ possess a dark centre, a true intensity zero, caused by the phase singularity or vortex at their centre. The intensity profile of LG modes do not change during propagation, aside from a scaling factor. Thus the dark centre will remain dark over the full propagation distance, making these beams ideal for trapping of e.g. neutral atoms [42] or Bose-Einstein condensates [43].

3.2 Generation of orbital angular momentum

As can be seen from Eq. (3.15), different values of the index l not only yield LG modes with different helical phase structures, their radial distribution is influenced by the index l as well. This implies that one LG mode cannot be converted to another by simply changing the phase distribution as a function of the azimuthal angle, a point that is demonstrated best by means of a mode expansion [5]. Nevertheless, this technique is often used to generate optical beams carrying OAM; it involves sending a fundamental Gaussian beam (u_{00}^{LG}) through a phase-modifying device. These devices have the ability to imprint a certain vorticity Q on the phase distribution of the incident beam, without converting between pure modes. Here, a short overview of the devices is given and their properties in relation to the OAM of the generated optical beam are mentioned.

3.2.1 Phase-shifting devices

The computer-generated phase hologram

The most popular technique for generating OAM in optical beams is the computer-generated phase hologram with a single edge dislocation [44], also called a fork grating [45] on account of its appearance. For a regular phase grating, the optical phase shift Φ is given by

$$\Phi(r, \theta) = \frac{1}{2} (\Phi_{max} - \Phi_{min}) \left[\sin\left(\frac{2\pi r \cos\theta}{a} \right) + 1 \right] + \Phi_{min}, \qquad (3.16)$$

in polar coordinates, where a is the grating constant and Φ_{max}, Φ_{min} are the maximum and minimum phase shifts imposed by the device, respectively. When considered in Cartesian coordinates, Φ thus depends on the x coordinate only. The result is that multiple diffraction orders will be generated.

For reasons of experimental convenience, binary gratings are most frequently used, the phase shift at a given point being given by

$$\Phi_{bin} = \begin{cases} \Phi_{min}, & \Phi(r, \theta) \leq \frac{\Phi_{max} + \Phi_{min}}{2} \\ \Phi_{max}, & \Phi(r, \theta) > \frac{\Phi_{max} + \Phi_{min}}{2} \end{cases} \qquad (3.17)$$

In the special case where $\Phi_{max} - \Phi_{min}$ is an integer multiple of 2π, no diffraction will occur. A standard *binary* phase grating can be seen in Fig. 3.3(a). Black and white indicate the two different phase shifts Φ_{min} and Φ_{max}.

To obtain the fork grating, a dislocation has to be added to the *continuous* standard phase grating (cf. Eq. (3.16)). The dislocation in the hologram is created by an additional dependence on the angle θ,

$$\Phi(r, \theta) = \frac{1}{2} (\Phi_{max} - \Phi_{min}) \left[\sin\left(\frac{2\pi r \cos\theta}{a} + Q_g \theta \right) + 1 \right] + \Phi_{min}, \qquad (3.18)$$

where Q_g is the vorticity that the grating imprints onto an incident field. Then, by applying Eq. (3.17), a binary phase hologram with a dislocation is obtained. In Fig. 3.3(b), such a hologram can be seen for $Q_g = 1$. The fork structure betrays the presence of the dislocation.
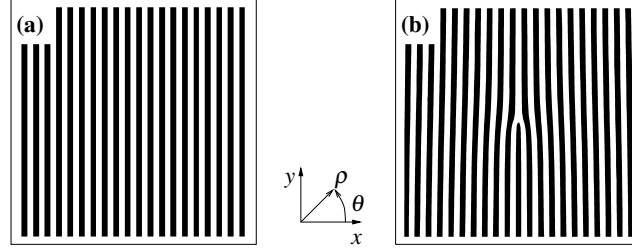
Figure 3.3: *(a) A standard binary phase grating ($Q_g = 0$), and (b) a binary phase grating containing a dislocation ($Q_g = 1$). Black and white indicate the two different phase shifts.*

Commonly, the binary fork grating is used in a configuration where the position of the fork ($r = 0$) is centred on an incident fundamental Gaussian beam. It then causes the mth diffraction order, considered along its own propagation axis z_m, to be multiplied by the phase factor $\exp(imQ_g\theta)$. This simple picture only holds for small diffraction angles, as the transverse amplitude distribution of the diffracted beam will be deformed for large diffraction angles. Thus in experiments, low diffraction orders are used. The phase factor appearing in these orders will cause the beams to carry an OAM expectation value per photon equal to $mQ_g\hbar$ along the z_m axis. If Q_g is an integer, the optical beams will be in a pure OAM mode, being composed only of u_{lp}^{LG} modes with mode index $l = mQ_g$. In Chapter 4, these devices are used in such a way that the position of the fork does *not* coincide with the centre of the incident Gaussian beam, and the OAM of the generated fields is investigated.

The spiral phase plate

A quite different device for generating beams carrying OAM is the spiral phase plate [5, 46–48]; it is shown in Fig. 3.4. This device can be treated in an analogous fashion to the aforementioned fork grating. The device imprints a vorticity Q_s onto an optical field, which is given by

$$Q_s = \Delta n \frac{h_s}{\lambda}, \tag{3.19}$$

where h_s is the step height of the device as shown in Fig. 3.4, Δn is the difference in refractive index between the plate and the surrounding medium, and λ is the vacuum wavelength of the incident light beam. The optical phase shift $\Phi(r, \theta)$ at an arbitrary position on the plate can then be written as

$$\begin{aligned} \Phi(r, \theta) &= Q_s\theta + \Phi_{\text{min}} \\ &= \frac{\Phi_{\text{max}} - \Phi_{\text{min}}}{2\pi}\theta + \Phi_{\text{min}}, \end{aligned} \tag{3.20}$$

the first term echoing the term in Eq. (3.18) that represents the dislocation. In contrast to the grating, the vorticity of the spiral phase plate is not fixed; instead, as betrayed by Eq. (3.19), it depends on external parameters ($\Delta n, \lambda$) that immediately reveal the chromatic nature of the device.
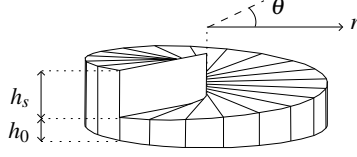
Figure 3.4: *A spiral phase plate. The plate imprints a helical phase onto an incident beam. The step height h_s plays an important role in the imprinted vorticity, whereas h_0 is provided for mechanical stability.*

The spiral phase plate acts a bit differently than the previously described hologram. While the hologram imprints a vorticity exclusively in the diffracted orders, with the charge depending on the order, the spiral phase plate only has a zeroth diffraction order; an incident fundamental Gaussian field is simply multiplied by the phase factor $\exp(iQ_s\theta)$. The resulting beam then propagates along the same axis as the incident beam, but will carry an OAM per photon equal to $Q_s\hbar$. In fact, the spiral phase plate is a fork grating with its spatial carrier frequency removed. The spiral phase plate and its use are extensively discussed in Chapters 5 through 8.

The spatially varying sub-wavelength grating

Recently, an additional technique for imprinting a helical phase structure on an optical beam has been introduced, based on a spatially varying sub-wavelength grating, exploiting the Pancharatnam-Berry phase [49]. The grating acts as a position-dependent uniaxial birefringent crystal, where the orientation of the slow and fast axes is determined by the orientation of the periodic pattern. Thus, the plate allows for local manipulations of the beam's polarisation state. When the parameters of the experiment are chosen properly, the polarisation of a circularly polarised beam incident on this plate, is inverted ($\sigma = +1 \leftrightarrow \sigma = -1$); due to the Pancharatnam-Berry phase acquired locally during this inversion, the beam is phase shifted as a function of the azimuthal angle. Therefore, the resulting field will also contain the phase factor $\exp(i\ell\theta)$, ℓ depending on the spatial structure of the grating within the incident beam's profile.

3.2.2 Mode converters

Whereas the previously described elements generate optical OAM, but can *not* generate optical beams in pure LG modes, the so-called mode converter [50] *can* do just that. It consists of two cylindrical lenses with focal lengths f and exploits the Gouy phase to generate the LG modes from other optical modes. Two versions have been described [50].

The first consists of two cylindrical lenses placed at a distance $f\sqrt{2}$ apart, inside a focused beam, as illustrated in Fig. 3.5(a). It converts an Hermite-Gaussian (HG) mode, u_{nm}^{HG} into an LG mode with indices $l = n - m$ and $p = \min(n,m)$. The HG modes are the Cartesian eigenmodes of the paraxial wave equations and therefore offer a complete basis just like the LG modes, although none of the individual HG modes contains OAM. The converter works only in the way described here when the symmetry axes of the transverse profile of the HG modes are rotated by $45°$ with respect to the transverse symmetry axes of the cylindrical

lenses. Similarly, an incident LG mode is transformed into an HG mode of which the axes are in the aforementioned orientation. This converter is called the '$\pi/2$ converter', based on the relative Gouy phase shift of each of the HG components that make up the resulting LG mode.
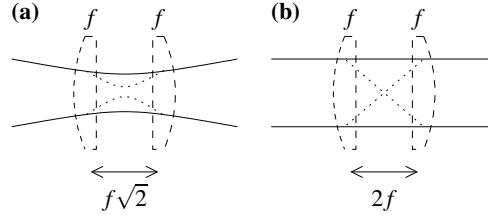

Figure 3.5: *The mode converters consisting of cylindrical lenses. In one transverse direction, the beam is allowed to pass without modification (solid), while in the direction where the two cylindrical lenses have a focal distance f (dashed), the beam is focused (dotted). (a) The $\pi/2$ converter is placed in a focused beam, the two lenses separated by a distance $f\sqrt{2}$. (b) The π converter, consisting of the two lenses separated by a distance $2f$, operates on a collimated beam.*

The second version is made by placing the two cylindrical lenses, a distance $2f$ apart, inside a collimated beam. This mode converter is called the 'π converter' and basically swaps the n, m indices of an incident HG mode. Thus, an incident LG mode u_{lp}^{LG} will have the sign of its vorticity inverted, resulting in u_{-lp}^{LG}. As such, it cannot generate OAM in a beam that did not contain any in the first place, in contrast to the $\pi/2$ converter. Note that in the ideal case, it is impossible for this converter to work due to the rotational symmetry of the LG modes, but in practice is found to be perfectly usable [50].

Both mode converters will acquire mechanical angular momentum when they impose or subtract OAM on optical beams. In a way, the π converter is equivalent to a conventional birefringent half-wave plate. The former is an astigmatic inverter of OAM, while the latter is a birefringent inverter of the spin angular momentum (polarisation). Thus an experiment equivalent to that performed by Beth in 1936 on spin angular momentum [25], namely the transfer of the angular momentum to the inverting device, should be possible. This has been attempted by Beijersbergen *et al.* [51], however without success.

It is important to note here that the mode converters cannot convert the fundamental Gaussian mode; both in the HG and in the LG basis, this mode is denoted by the indices $n = 0, m = 0$, so that $l = 0, p = 0$. Propagation of a beam in this mode through either converter will result in the same beam, carrying no OAM. The converters will only generate an LG beam carrying OAM when its input belongs to a certain subset of HG or LG beams, characterised by $n \neq m$.

3.3 Orbital angular momentum in the quantum regime

The separation of total angular momentum into a spin and orbital part (cf. Section 3.1) can also be made in the quantum regime, the commutation rules and eigenvalues being discussed extensively elsewhere [4]. Here, we provide a brief overview of the results.

3.3.1 The orbital angular momentum operator

For a single-photon state $|\psi\rangle$ in a paraxial mode, say an LG mode, the z-component of the OAM operator has the familiar appearance,

$$
\begin{aligned}
\hat{L} &= \left(\hat{\vec{r}} \times \hat{\vec{p}} \right)_z \\
&= \frac{\hbar}{i} \left(\hat{x} \frac{\hat{\partial}}{\partial y} - \hat{y} \frac{\hat{\partial}}{\partial x} \right) \\
&= \frac{\hbar}{i} \frac{\hat{\partial}}{\partial \theta},
\end{aligned}
\tag{3.21}
$$

in Cartesian and cylindrical coordinates, respectively. The wave function of the photon may then be written as

$$
\begin{aligned}
\langle r, \theta, z | \psi \rangle &= u(r, \theta, z) \\
&= \tilde{u}(r, \theta, z) \exp\left[i\chi(r, \theta, z) \right].
\end{aligned}
\tag{3.22}
$$

When $\chi(\theta) = \ell\theta$ with integer ℓ, this wavefunction describes the photon eigenstates of the OAM operator, with eigenvalues $\ell\hbar$.

While the OAM of classical beams can be measured when absorbed by small particles [40], the OAM of a single photon is difficult to measure, since it only contains an angular momentum of order $\hbar$. A clever technique to overcome this problem has been introduced by Leach *et al.*, and is based on a modified Mach-Zehnder interferometer [31], where, as usual, a single photon is allowed to interfere with itself. Thus the technique does not depend on any transfer of angular momentum to a body with mass, as in the classical case, but instead on examining the local phase distribution of the mode in which the photon resides. The interferometer sends the even OAM states to one output port, while the odd OAM states appear at the second output port. By cascading such interferometers in combination with vortex-generating devices and single-photon detectors, it is possible to determine the OAM value of an incoming photon in an integer basis.

3.3.2 Conservation of orbital angular momentum in spontaneous parametric down-conversion

A relatively simple method of generating single photons is by utilising the nonlinear optical phenomenon known as spontaneous parametric down-conversion (SPDC). In this process, a photon from a classical pump beam propagating along z is destroyed inside a crystal with a $\chi^{(2)}$ nonlinearity, and two photons, the signal and idler, are created. Naturally, both energy and momentum are conserved in this process, as well as the OAM along the z-axis [52, 53], at least in the paraxial approximation. These conservation laws are the only constraints for the creation of the two photons, neither restraining their *individual* energy, momentum, or angular momentum.

Most experiments involving SPDC are performed near frequency degeneracy. This means that the down-converted pair is projected onto a state where the frequency of both photons

is half the frequency of the pump beam[1]. This way, the signal and idler photons become identical and if the experiment is carried out sufficiently carefully, indistinguishable.

In general, the down-converted pair does not propagate collinearly, i.e. the propagation axes of the two newly created photons do not coincide with that of the pump beam. Instead, the down-converted photons are spread out, their frequency correlated with their propagation direction. Thus after filtering near degeneracy, the signal and idler photons travel along axes z_s, z_i that make angles (identical in magnitude, but opposite in direction) with the propagation axis z of the pump beam. In most experiments, the geometry of the setup is chosen so that these angles are small, such that the experiment is globally paraxial. It can be shown analytically that in this case, assuming that the crystal is thin enough, OAM during SPDC is conserved [54].

An early experiment [55] on OAM in SPDC led to the conclusion that OAM was *not* conserved in this process. The method of detection, however, was not based on quantum correlations between signal and idler photons, but instead investigated the appearance of the down-conversion 'beam', i.e. it brought forth its classical features instead of investigating the true quantum nature. In a subsequent experiment, now based on the detection of individual photon pairs, the quantum correlations of the photons' OAM were indeed measured, to reveal that the OAM during SPDC *is* conserved [17], as expected.

---

[1]During filtering in the frequency domain, part of the wavefunction is discarded. What remains is normalised and is from that point onwards considered to be the photon pair.

CHAPTER 4

The intrinsic orbital angular momentum of paraxial beams with off-axis imprinted vortices

We investigate the orbital angular momentum of paraxial beams containing off-axis phase dislocations, and put forward a simple method to calculate the intrinsic orbital angular momentum of an arbitrary paraxial beam. Using this approach we find that the intrinsic OAM of a fundamental Gaussian beam, with a vortex imprinted off axis, has a Gaussian dependence on the vortex displacement, implying that the expectation value of the intrinsic orbital angular momentum of a photon can take on a continuous range of values (i.e. integer and non-integer values in units of ℏ). Finally, we investigate both numerically and experimentally the far-field profiles of beams carrying half-integer orbital angular momentum per photon, these beams having been created by the method of imprinting off-axis vortices.

4.1 Introduction

While the orbital angular momentum (OAM) of light is often viewed as a property of a classical beam [2–5, 29, 30, 32, 40], it has recently received much attention at the quantum, i.e. single-photon, level [17, 31, 54, 56–58]. This is a consequence of the fact that OAM promises to provide a truly multi-dimensional alphabet to the field of quantum information [17], in the form of a qu*N*it. The OAM of a photon in its propagation direction is usually characterised by the integer ℓ (in units of $\hbar$), meaning that the expectation value of the photon's OAM equals $\ell\hbar$. Thus an absorber placed in the path of such a beam will acquire an angular momentum of $\ell\hbar$ times the number of absorbed photons. The integer ℓ enumerates the OAM states of the photon and thus the qu*N*it's levels.

The most widespread method of generating OAM in an optical beam, and in a beam of photons for that matter, is by imprinting one or more vortices on its transverse field distribution. The vortex charge Q of the resulting beam is defined as [36]

$$Q = \frac{1}{2\pi} \oint d\vec{l} \cdot \vec{\nabla}\chi,\tag{4.1}$$

where χ is the phase of the field, and the closed path $\vec{l}$ goes through points where χ is analytical and encircles all imprinted vortices; the vortex charge Q is integer-valued.

For analytical input beams, the output beam can also be described analytically when the vortex-imprinting device has a transmission function $t(r,\theta) = r\exp(i\theta)$ (in polar coordinates). The field will then contain an *analytical* vortex, also called an *r*-vortex, a concept which enjoys considerable popularity in literature [59–62]. If the incident beam is a fundamental Gaussian, the result for this type of vortex-imprinting device is a pure helical Laguerre-Gaussian beam, $u_{10}(r,\theta)$ (see below). Displacement of the device over (r_0,θ_0) with respect to the incident Gaussian beam, so that the transmission function becomes $t'(r,\theta) = r\exp(i\theta) - r_0\exp(i\theta_0)$, results in a superposition of two Laguerre-Gaussian modes, $u_{00}(r,\theta)$ and $u_{10}(r,\theta)$ [59].

In practice, however, generation of helical beams is accomplished by passing a fundamental Gaussian beam through a device that only modifies the phase and not the amplitude, i.e. the transmission is function $t(r,\theta) = \exp[i\chi(r,\theta)]$. A vortex can be obtained by choosing, for instance, $\chi(r,\theta) = \theta$ so that $t(r,\theta) = \exp(i\theta)$. We will refer to this type as a *phase* vortex, in literature also known as a point vortex [63–65]. It shares the phase structure but not the amplitude structure with the analytical vortex. An incident fundamental Gaussian beam results in superposition of many Laguerre-Gaussian beams, all with the same OAM [5]. A popular device for generating phase vortices is the hologram with a dislocation in its centre [44, 66], also called the fork hologram.

The topological charge of the imprinted vortex depends on the strength of the dislocation and the diffraction order of the hologram. When the dislocation is well centred with respect to the cylindrically symmetric incident beam, the diffracted beams are also cylindrically symmetric and carry no net transverse momentum relative to their symmetry axis. When the OAM is calculated around the symmetry axis of each beam, its value per photon in units of $\hbar$ represents the intrinsic OAM [39, 40] and is simply equal to the vortex charge Q multiplied by the order number m.

When the hologram, and thus the dislocation, is *not* centred with respect to the beam, thus generating an off-axis vortex, the far-field profile will, in general, not have cylinder symmetry [17, 65]. The propagation axis of the diffracted beam, which is defined as the axis with respect to which the field has no net transverse momentum, will change direction when the dislocation is displaced. It is, however, precisely this propagation axis that is required to calculate the intrinsic OAM of a beam [39]. Therefore, a calculation of the intrinsic OAM as a function of the hologram displacement becomes cumbersome, because for each displacement one first has to find the propagation axis of the beam.

In this Chapter, we will present an alternative method to calculate the intrinsic OAM of a beam that is diffracted off an off-axis-positioned fork hologram. Having introduced that method, we apply it to the case that the input beam is a fundamental Gaussian and show that the intrinsic OAM of a diffracted beam has a Gaussian dependence on the transverse displacement of the dislocation in the hologram relative to the centre of the input beam. The expectation value of the intrinsic OAM per photon in the mth diffraction order of a hologram with integer dislocation strength Q can thus take on *any value* $|\ell|\hbar < |mQ|\hbar$ (while its eigenvalue spectrum remains integer). Throughout this Chapter, we will only refer to the expectation value of the OAM; so, in spite of using the word 'photon', the treatment is essentially classical and 'photon' is only meant to be a convenient energy unit.

Note that in the present scheme, the non-integer character of the OAM is not imprinted in the fork hologram, but is caused by its off-axis use. Beams carrying non-integer OAM can also be generated by inserting a phase-modifying device on-axis in a Gaussian beam; in that case, the device must carry a mixed screw-edge dislocation and therefore a fixed non-integer dislocation strength. Examples thereof are spiral phase plates and fork holograms with half-integer dislocation strength (cf. Chapter 5 and Refs. [5, 67]). The method outlined in the present Chapter has thus added flexibility by the ability to simply tune the OAM. We will show that the OAM of the output beam calculated in the way presented here is intrinsic. In order to do so, we introduce a more general criterion for determining the intrinsic nature of OAM. Finally, we illustrate our theoretical work with experimental and calculated far-field patterns of beams that have OAM multiply imprinted in units of $\frac{1}{2}\hbar$ per photon, by stacking displaced holograms in the same Fourier plane.

4.2   Optical vortices and orbital angular momentum

Paraxial optical beams carry both spin and orbital angular momentum, where the former is connected to the polarisation of the light, and the latter to the transverse field distribution [2, 3]. For a classical, paraxial, monochromatic (frequency ω) beam with uniform polarisation, indicated by the transverse vector $\vec{\sigma}$, the electric field can be written as

$$\vec{E}(\vec{r},t) = \vec{\sigma}u(\vec{r})\exp\left(ikz - i\omega t\right) + c.c. \tag{4.2}$$

As OAM is a constant of propagation, we can, for the purpose of calculating the OAM, consider $u(\vec{r})$ in any transverse plane. We choose $z = 0$ so that we can write $u(r, \theta, 0) \equiv u(\vec{\rho})$, where $\vec{\rho} = (r, \theta)$ is the transverse position vector. As we are interested in the *orbital* angular momentum, we assume a linearly polarised field, so that the density of transverse linear

momentum is given by

$$\vec{p}(\vec{\rho}) = \frac{\varepsilon_0}{i\omega}\left[u^*(\vec{\rho})\vec{\nabla}u(\vec{\rho}) - c.c.\right],\tag{4.3}$$

where $\vec{\nabla}$ is the transverse gradient operator. The z-component of the OAM per unit length can be calculated as [2, 3]

$$
\begin{aligned}
L &= \int \left[\vec{\rho} \times \vec{p}(\vec{\rho})\right]_z \mathrm{d}\vec{\rho}\\
&= \frac{2\varepsilon_0}{i\omega}\int u^*(\vec{\rho})\left(\vec{\rho}\times\vec{\nabla}\right)_z u(\vec{\rho})\,\mathrm{d}\vec{\rho},
\end{aligned}\tag{4.4}
$$

where in polar coordinates, $\vec{\rho}\times\vec{\nabla} = \frac{\partial}{\partial\theta}$. As Eq. (4.3) reveals, the momentum density and thus the OAM are determined by the phase gradient of the field distribution $u(\vec{\rho})$. The OAM per photon is then

$$\ell\hbar = \frac{\hbar\omega}{2\varepsilon_0 \int |u(\vec{\rho})|^2 \,\mathrm{d}\vec{\rho}} L\tag{4.5a}$$

$$= \int u^*(\vec{\rho})\frac{\hbar}{i}\frac{\partial}{\partial\theta}u(\vec{\rho})\,\mathrm{d}\vec{\rho} \Big/ \int |u(\vec{\rho})|^2 \,\mathrm{d}\vec{\rho},\tag{4.5b}$$

where the denominator in Eq. (4.5a) is the field energy per unit length. Note that Eq. (4.5b) has the appearance of the quantum-mechanical expression for the expectation value of the z-component of the OAM of a wave function.

A convenient basis for describing the OAM of a paraxial beam is the complete orthonormal set of Laguerre-Gaussian (LG) modes [2, 41]. These cylindrically symmetric modes possess, relative to their symmetry axis, an OAM per photon that is integer-valued in units of $\hbar$. In the plane $z = 0$, an LG mode can be expressed as [5, 41]

$$u_{lp}^{\mathrm{LG}}(r,\theta) = C_{lp}^{\mathrm{LG}}\left(\frac{r\sqrt{2}}{w_0}\right)^{|l|}L_p^{|l|}\left(\frac{2r^2}{w_0^2}\right)\exp\left(-\frac{r^2}{w_0^2}\right)\exp\left(il\theta\right),\tag{4.6}$$

where C_{lp}^{LG} is a normalisation constant, $L_p^{(l)}(x)$ is a generalised Laguerre polynomial [68], the integers $l \in \{-\infty,\ldots,\infty\}$ and $p \in \{0,\ldots\infty\}$ are indices characterising the transverse profile of the mode, and w_0 is the beam waist radius. The vortex contained within an LG mode lies at the centre; it is caused by the exponential phase factor and has a charge equal to l (cf. Eq. (4.6)). The OAM per photon in units of $\hbar$ contained in this field is also given by l [2, 3], and is therefore always integer. Information regarding the radial profile of the mode is contained in the index p.

To calculate the OAM of a beam with any number of on- or off-axis phase vortices, one usually makes a mode decomposition [5],

$$u(\vec{\rho}) = \sum_{l=-\infty}^{\infty}\sum_{p=0}^{\infty}C_{lp}u_{lp}^{\mathrm{LG}}(\vec{\rho})\tag{4.7}$$

where C_{lp} are the coefficients of the LG components,

$$C_{lp} = \int_0^{\infty}\int_0^{2\pi}u(\vec{\rho})\left[u_{lp}^{\mathrm{LG}}(\vec{\rho})\right]^*\mathrm{d}\vec{\rho}.\tag{4.8}$$
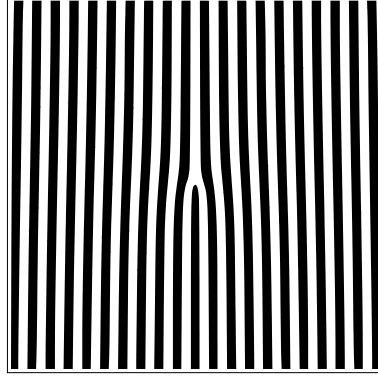
Figure 4.1: *A binary phase hologram with a dislocation in its centre. Black and white indicate the two values of the shift in phase imprinted on the incident field.*

The OAM per photon in units of $\hbar$, carried by the field $u(\vec{\rho})$, is then given by

$$\ell = \sum_{l=-\infty}^{\infty} \sum_{p=0}^{\infty} l \left|C_{lp}\right|^2,\qquad(4.9)$$

where the z-axis coincides with the symmetry axis of the LG modes. It is thus immediately clear that for a beam carrying an *off-axis* vortex, the expectation value of the OAM per photon is, in general, *non-integer* with respect to the chosen z-axis. This also shows that vortex charge and OAM are *not* the same concept. The topological charge of a vortex is completely independent of the chosen reference system and is thus independent of its position, while this is not always true for OAM. To further stress the difference, it is important to realize that an optical beam can in fact carry OAM in the absence of any topological charge [38].

4.3   The fork phase hologram

A fork phase hologram is basically a phase grating, carrying a fundamental reciprocal-lattice vector $\vec{g}$, with a phase distribution $\exp(iQ\theta)$ superimposed, Q being the topological charge to be imprinted in the first-order diffracted field. The factor $\exp(iQ\theta)$ manifests itself as a fork-like feature in the phase pattern of the hologram, giving rise to a screw dislocation in the non-zero diffraction orders. Figure 4.1 shows a binary variant of such a fork phase hologram, where the black and white in the figure indicate the two values of the phase shift, usually differing by π. When a fundamental Gaussian beam is perpendicularly incident on such a hologram, the various diffraction orders will pick up the azimuthal component of the hologram's phase distribution, such that the mth diffraction order will carry a phase factor $\exp(imQ\theta)$. When the incident beam and hologram are centred with respect to each other, each diffraction order is cylindrically symmetric around its own propagation axis. In this case, the propagation axis, i.e. the axis with respect to which the beam has zero transverse momentum, coincides with the diffraction axis z_m. The direction of the latter axis is solely determined by the reciprocal-lattice vector $\vec{g}$ of the hologram and the wavelength of the inci-

dent light, and is neither influenced by the hologram's topological component nor its position in the incident beam.

For a calculation of the OAM of a diffracted beam, we will use a coordinate system of which the *z*-axis is aligned with the diffraction axis introduced above. In this coordinate system, the input field becomes

$$u^{\text{in}}(\vec{\rho}) \to u_m^{\text{in}}(\vec{\rho}) \exp\left(-im\vec{g}\cdot\vec{r}\right), \tag{4.10}$$

where the vector $\vec{g}$ is the aforementioned reciprocal-lattice vector of the grating structure in the binary hologram.

The phase fronts of the diffracted beams are *helical* in this coordinate system, as a consequence of the dislocation in the hologram,

$$u_m^{\text{out}}(\vec{\rho}) = C_m u_m^{\text{in}}(\vec{\rho}) \exp\left(imQ\theta\right), \tag{4.11}$$

where the real constant $|C_m|^2$ represents the diffraction efficiency into the mth order, and we have assumed that the dislocation is positioned in the centre of the beam, at $\vec{\rho} = 0$. Applying Eq. (4.5b) to Eq. (4.11) yields an OAM per photon equal to $mQ\hbar$.

4.4 Off-axis vortices

When the fork hologram is displaced over a distance $|\vec{\rho}_v|$ in the transverse plane of the incident Gaussian beam, the centres of intensity of the diffraction orders in the far field shift. The direction of the *propagation* axis, i.e. the zero transverse-momentum axis, is thus changed, since it is defined as the axis that goes through the centre of intensity of the field in all transverse planes. As a result, the transverse momentum with respect to the previously defined *diffraction* axis is non-zero [39, 40], as indicated in Fig. 4.2. The fact that the orientation of the propagation axis depends on the displacement $\vec{\rho}_v$ of the fork hologram implies that to calculate the intrinsic OAM of the output beam for different values of $|\vec{\rho}_v|$, one would have to first determine the propagation axis for each value of the displacement.

Here, we will show that to calculate the intrinsic OAM of the diffracted beam, one may always use the diffraction axis, as long as a simple constraint is satisfied. The advantage of this approach is that the diffraction axis is fixed in a given experiment and is thus independent of the displacement of the hologram.

4.4.1 Intrinsic orbital angular momentum

In classical mechanics, the intrinsic angular momentum of a rigid body is obtained by taking a frame of reference where the origin lies in the centre of mass. Obviously, the *z*-component of the angular momentum is then also intrinsic. Tilting the *z*-axis over an angle α changes the calculated value of that component by a factor $\cos\alpha$. Thus when α is small, the *z*-component of the angular momentum is unaffected.

This approach can also be applied to the *z*-component of the OAM of a beam of light[1]

---

[1] It is important to realise that separation of the total angular momentum of a beam in a spin and orbital part can only be done for the component of the total angular momentum that lies parallel to (or at least makes a paraxial angle with) the propagation axis of the beam [3].
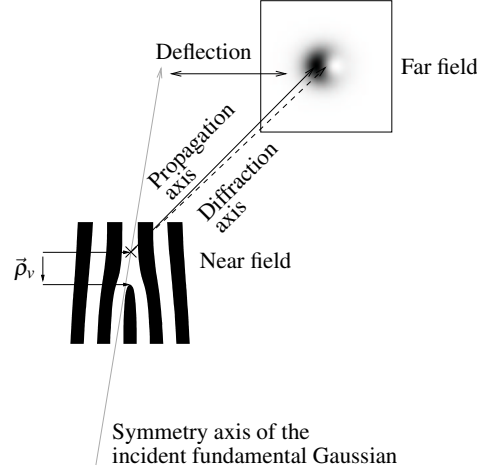
Figure 4.2: *Schematic illustration of an experiment where a fork hologram is positioned off-axis with respect to an incident Gaussian beam. The incident beam is off-centre in the near field, as indicated by the black cross that lies above the fork in the hologram. The diffraction axis (dashed line) does* not *coincide with the propagation axis, with respect to which there is zero net transverse momentum (solid black line). In the far field intensity profile, black and white indicate regions of high and low intensity, respectively.*

by choosing the origin of the frame in the centre of the beam in the near field, while the *z*-axis is chosen to be parallel to the propagation axis of the beam. It has been shown that the latter condition gives the freedom to arbitrarily choose the position of the origin, without influencing the value of the *z*-component of the OAM [39, 40]. We will show that, instead, we may choose to keep the origin fixed in the centre of the near-field intensity distribution, and tilt the *z*-axis over an angle α to align it to the diffraction axis.

Intrinsic orbital angular momentum of a paraxial optical beam

Let us assume an arbitrary, monochromatic paraxial beam of which the amplitude distribution in the plane $z = 0$ is described by the complex function $u(\vec{\rho})$, where the coordinate system S has been chosen so that the beam is centred at the origin and does not carry transverse momentum,

$$\int \vec{\rho} \, |u(\vec{\rho})|^2 \, \mathrm{d}\vec{\rho} = 0, \tag{4.12}$$

$$\int \vec{p}(\vec{\rho}) \, \mathrm{d}\vec{\rho} = 0. \tag{4.13}$$

Here, $\vec{\rho}$ indicates the transverse position and $\vec{p}$ is the transverse linear momentum density per unit length as given in Eq. (4.3). Thus, Eq. (4.12) fixes the origin of the reference frame in the centre of the intensity distribution, while Eq. (4.13) aligns the *z*-axis with the propagation axis of the field.

The z-component of the OAM per unit length in coordinate system S is then given by

$$L^0 = \int [\vec{\rho} \times \vec{p}(\vec{\rho})]_z \, \mathrm{d}\vec{\rho}. \tag{4.14}$$

Because of the definition of our coordinate system given in Eqs. (4.12,4.13), this is the intrinsic OAM. We will now study the effect of tilting and displacing the beam with respect to the reference frame.

When we tilt the field $u(\vec{\rho})$ over an angle α with respect to the z-axis, we obtain

$$u'(\vec{\rho}) = u(\vec{\rho}) \exp\left(i\vec{k}_0 \cdot \vec{\rho}\right), \tag{4.15}$$

neglecting the tilt-induced second-order deformation of the amplitude profile. Here, $\vec{k}_0$ represents the tilt and, in the paraxial approximation, the length of $\vec{k}_0$ is equal to α times the beam's wave vector. The transverse component of the momentum density per unit length of the tilted beam is given by

$$
\begin{aligned}
\vec{p}'(\vec{\rho}) &= \frac{\varepsilon_0}{i\omega}\left[u^*(\vec{\rho})\vec{\nabla}u(\vec{\rho}) - u(\vec{\rho})\vec{\nabla}u^*(\vec{\rho}) + 2i\vec{k}_0\left|u(\vec{\rho})\right|^2\right] \\
&= \vec{p}(\vec{\rho}) + \frac{2\varepsilon_0}{\omega}\vec{k}_0\left|u(\vec{\rho})\right|^2.
\end{aligned} \tag{4.16}
$$

The transverse displacement $\vec{\rho}_0$ of the field is accounted for by calculating the z-component of the OAM with respect to the point $\vec{\rho}_0$,

$$
\begin{aligned}
L' &= \int \left[(\vec{\rho} - \vec{\rho}_0) \times \vec{p}'(\vec{\rho})\right]_z \, \mathrm{d}\vec{\rho} \\
&= L^0 - \frac{2\varepsilon_0}{\omega}\left(\vec{\rho}_0 \times \vec{k}_0\right)_z \int \left|u(\vec{\rho})\right|^2 \, \mathrm{d}\vec{\rho},
\end{aligned} \tag{4.17}
$$

where two cross terms have vanished due to our initial constraints, given by Eq. (4.12) and Eq. (4.13). We find that, generally, the OAM L' of the tilted beam with respect to a point at a position $\vec{\rho}_0$ differs from L^0. It is also clear that, by a proper choice of $\vec{\rho}_0$ or $\vec{k}_0$, L' can be made to be equal to L^0.

One way to have $L' = L^0$ is to choose $\vec{\rho}_0$ equal to zero: the OAM should always be calculated with respect to the centre of the beam in the near field. In that case, the (paraxial) tilt of the beam with respect to the z-axis is irrelevant, i.e. the choice of z-axis is free.

The second way to have L' equal to the intrinsic momentum, is to align the z-axis so that it is parallel to the propagation axis of the beam, $\vec{k}_0 = 0$. Consequently, the field will not have a net transverse momentum. It then does not matter with respect to which transverse position $\vec{\rho}_0$ the OAM is considered; it is found to be intrinsic. This constraint where the transverse momentum of the beam is required to vanish has earlier been put forward by Berry [39].

From the calculation, a third and final method is found, namely by choosing $\vec{\rho}_0 \parallel \vec{k}_0$, independent of the magnitude of each of these vectors.

The first criterion that we introduced ($|\vec{\rho}_0| = 0$) gives us the freedom to use the diffraction axis for calculating the intrinsic OAM. Because the orientation of the diffraction axis is independent of the displacement of the hologram, we thereby have a very practical method to calculate the intrinsic OAM; this is the one we will use.

The orbital angular momentum of a Gaussian beam with an off-axis phase vortex

Having found a simple method to obtain the intrinsic value of OAM, we now proceed to calculate this quantity. We consider the case where a fundamental Gaussian beam intersects a fork phase hologram in its waist. The incident field is described by the function

$$u^{\text{in}}(\vec{\rho}) = B \exp\left(-\frac{|\vec{\rho}|^2}{w_0^2}\right),\tag{4.18}$$

where w_0 is the waist and where the constant B is the peak amplitude. We thus have chosen a frame where the position of the origin is fixed to the centre of the intensity distribution in the near field. The hologram has its dislocation at a transverse position $\vec{\rho}_v$ relative to the beam's centre. We wish to calculate the intrinsic OAM of the mth diffraction order, which is the OAM with respect to the centre of the beam. We use as integration variable $\vec{\rho}$ the position with respect to the vortex, so that $\vec{\rho} + \vec{\rho}_v$ is the position with respect to the beam. The mth-order diffracted beam is given by

$$u_m^{\text{out}}(\vec{\rho}) = C_m u_m^{\text{in}}(\vec{\rho} + \vec{\rho}_v) \exp\left(imQ\theta\right),\tag{4.19}$$

and the intrinsic OAM is given by

$$L_m^0 = \frac{2\varepsilon_0}{i\omega} \int u_m^{\text{out}*}(\vec{\rho}) \left[(\vec{\rho} + \vec{\rho}_v) \times \vec{\nabla}\right]_z u_m^{\text{out}}(\vec{\rho}) \, d\vec{\rho}.\tag{4.20}$$

When substituting Eq. (4.19), the gradient operator acting on the product $u_m^{\text{in}} \exp\left(imQ\theta\right)$ gives rise to two terms. The contribution to L_m^0 from the first term is simply equal to $C_m^2 L^{\text{in}}$, which vanishes since the input beam has zero OAM. In order to calculate the contribution from the gradient of the phase term $\exp\left(imQ\theta\right)$, it is convenient to apply the gradient operator in polar coordinates, which gives the identity

$$\left[(\vec{\rho} + \vec{\rho}_v) \times \vec{\nabla}\right]_z \exp\left(imQ\theta\right) = imQ\frac{\vec{\rho} \cdot (\vec{\rho} + \vec{\rho}_v)}{r^2} \exp\left(imQ\theta\right),\tag{4.21}$$

where $\vec{\rho} = (r, \theta)$ so that $r = |\vec{\rho}|$ and $r_v = |\vec{\rho}_v|$. Thus for the intrinsic OAM, we find the integral expression in polar coordinates

$$\begin{aligned} L_m^0 &= \frac{2\varepsilon_0}{\omega} C_m^2 mQB^2 \int_0^{2\pi} \int_0^{\infty} \exp\left(-2\frac{r^2 + 2rr_v\cos\theta + r_v^2}{w_0^2}\right)(r + r_v\cos\theta) \, dr \, d\theta \\ &= C_m^2 mQ\frac{\varepsilon_0}{\omega}w_0^2\pi B^2 \exp\left(-2\frac{r_v^2}{w_0^2}\right).\end{aligned}\tag{4.22}$$

We thus find that the intrinsic OAM of the output beam has a Gaussian dependence on the vortex displacement. This result is conceptually attractive: for large displacements r_v of the dislocation away from the beam's centre, the intrinsic OAM tends towards the OAM of the incident beam, which is equal to zero in the case considered here. In that limit, the imprinted vortex simply gives rise to a transverse linear momentum in the output beam.

When a beam of photons is diffracted by a hologram carrying an off-axis vortex, applying Eq. (4.5b) shows that each diffracted photon carries an intrinsic OAM equal to $mQ\hbar \times$
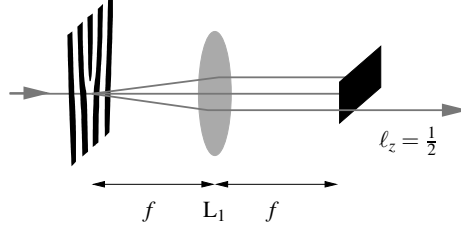
35

Figure 4.3: *Experimental setup for examining the far-field intensity profile of a $\ell = \frac{1}{2}$ beam. A fundamental Gaussian impinges on a displaced hologram, carrying a unity strength phase dislocation. The displacement between the centre of the hologram and that of the input beam equals $w_0\sqrt{\ln(2)/2}$ (cf. Eq. (4.22)), where w_0 equals the radius of the input beam. The lens L_1 with focal length f images the far field of the first diffraction order, while the other orders are blocked.*

$\exp\left(-2r_v^2/w_0^2\right)$. Consequently, the expectation value of the OAM of these photons, is no longer necessarily an *integer* multiple of $\hbar$. For instance, imprinting a vortex with charge unity ($Q = 1$), displaced by an amount $w_0\sqrt{\ln(2)/2}$ relative to the Gaussian input beam, yields an intrinsic OAM per photon equal to $\hbar/2$, i.e. $\ell = 1/2$, in the first diffraction order ($m = 1$); this can easily be found by using Eq. (4.5b) and Eq. (4.22) with $L^{\text{in}} = 0$. In the experiments that are discussed below, the photons carry an OAM with that expectation value.

4.5 Beams with $\ell = 1/2$

4.5.1 One off-axis vortex

The setup shown in Fig. 4.3 allows us to generate an $\ell = \frac{1}{2}$ beam by letting a fundamental Gaussian impinge on a hologram containing a single screw dislocation, displaced over a distance $w_0\sqrt{\ln(2)/2}$ relative to the centre of the input beam. Here, w_0 is the waist of the incident beam. The lens L_1 with focal length f assists in imaging the far field of the $\ell = \frac{1}{2}$ beam, which is the first diffraction order. A calculated near-field intensity profile is seen in Fig. 4.4(a), where the $\oplus$ symbol indicates the position of the dislocation, causing a vortex of charge $+1$ in the first diffraction order. The far-field intensity profile of this beam, at a wavelength of 633 nm, can be seen in Fig. 4.4(b), while the far-field pattern, as calculated by taking the Fourier transform of the near field, is shown in Fig. 4.4(c). The $\oplus$ symbol indicates the location of a $+1$ charged vortex in the far field. Both the calculated image and experimentally acquired image are peak-normalised to enhance their contrast. The experimental image agrees very well with the simple diffraction calculation. The centre of the intensity distribution in Fig. 4.4(c) does *not* coincide with the far-field position of the diffraction axis, indicated by the intersecting dashed lines; this $\ell = 1/2$ beam is a clear example of a beam where propagation and diffraction axes are not coincident.

As observed in both numerical calculations and experimental results, we find that the position where the *phase* vortex $\exp(imQ\theta)$ was imprinted in the near field does *not* coincide with that in the far field; it appears as if the position of the vortex rotates over $\pm 90°$ (depending on the sign of the vortex) around the diffraction axis when the beam propagates from the
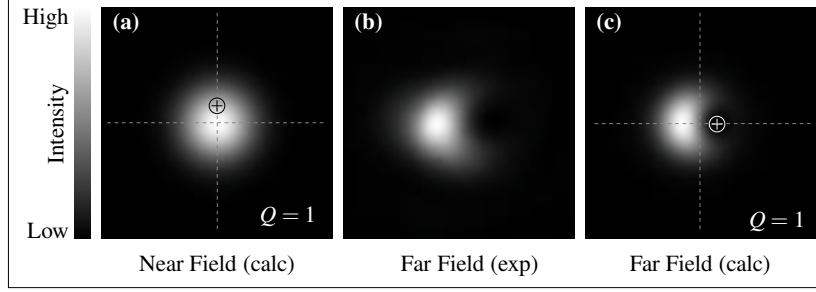
Figure 4.4: *Intensity profiles of an $\ell = 1/2$ optical beam, obtained in the setup of Fig. 4.3. (a) Calculated near-field profile, where $\oplus$ indicates the position of the vortex unity-charge in the near field. The intersection of the dashed lines indicates the centre of intensity. (b) The experimentally obtained far-field intensity profile, at a wavelength of 633 nm. (c) The calculated far-field profile, where the $\oplus$ indicates the position of a unity-charge vortex and the intersection of the dashed lines indicates where the diffraction axis crosses the far-field plane.*

near field to the far field. This is similar to the behaviour of a fundamental Gaussian with off-axis *analytical* vortices, i.e. a vortex with both amplitude and phase information [59].

Since we have chosen our frame of reference so that in the near field, its origin coincides with the centre of the intensity distribution and the beam is paraxial, we satisfy one of the three constraints as outlined in Section 4.4.1. Therefore the half-integer OAM in this experiment is intrinsic.

4.5.2 Two off-axis vortices

Because of applications in quantum information, there is currently considerable interest in beams containing multiple off-axis vortices [32]. Here, we will restrict ourselves to the case of two off-axis vortices, imprinted by phase holograms as described in the previous sections, which are displaced in the same or opposite direction relative to a fundamental Gaussian input beam. The displacement of each hologram in units of the beam's waist w_0 equals $\sqrt{\ln(2)/2}$. Consequently, each hologram imparts OAM to its first diffraction orders, equal to $|\ell| = 1/2$.

In the setup of Fig. 4.5, the $+1$ diffraction order of the first hologram acquires $\ell = 1/2$. It propagates towards the second hologram, passing through a telescope of unit magnification (lenses L_1 and L_2) and acquires additional OAM by being diffracted at the second hologram. The $+1$ diffraction order of this second hologram thus has $\ell = +1/2 + 1/2 = +1$, while the -1 diffraction order carries $\ell = +1/2 - 1/2 = 0$.

The inverting telescope has two effects: *(i)* it images the near field of the first hologram on top of the second, whereby the two phase dislocations are imprinted in the same transverse plane and *(ii)* it inverts the image of the first hologram. In the setup shown in Fig. 4.5, both the hologram dislocations are shifted upward relative to the incident beam, thereby suggesting that the phase dislocations become superposed. Because of the image inversion, the imprinted phase dislocations are in fact *not* superposed, but appear on opposite sides of the input beam.

Figure 4.6 shows the first diffraction orders of the second hologram. Each row shows,
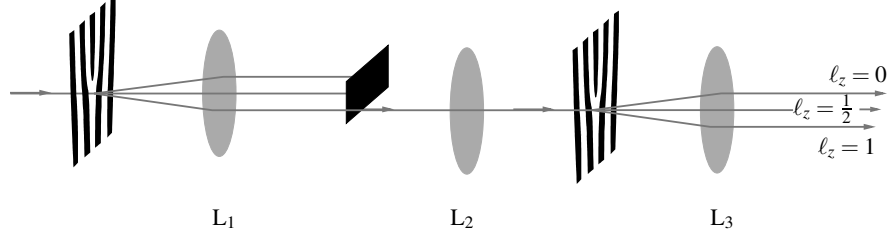
$\ell_z = 0$
$\ell_z = \frac{1}{2}$
$\ell_z = 1$

L_1 L_2 L_3

Figure 4.5: *Experimental setup for examining the far-field intensity profile of beams with two off-axis imprinted vortices. A fundamental Gaussian beam impinges on a hologram. Lenses L_1 and L_2 image the near field of the first diffraction order onto a second hologram. Lens L_3 then images the far-field intensity profiles of the three lowest diffraction orders onto a CCD camera. Both holograms are displaced with respect to the incident beam, so that both holograms each imprint a single vortex at the same location or at opposite locations.*

from left to right, *(i)* a calculated near-field distribution, where the imprinted vortices are indicated with the $\oplus$ and $\ominus$ symbols and the dashed lines indicate the centre of the beam, *(ii)* an experimentally obtained far-field intensity profile (at $\lambda = 633$ nm), and *(iii)* a far-field image as calculated by taking the Fourier transform of the theoretical near field. The top row shows the results for the -1st diffraction order of the second hologram. In the far field, the transverse intensity distribution forms a peculiar pattern (Fig. 4.6(b)), in excellent agreement with the result of our calculations (Fig. 4.6(c)). A calculation of the far-field phase distribution (not shown here) reveals that the two lobes in Fig. 4.6(c) have opposite phase. The bottom row shows the result for the $+1$ diffraction order of the second hologram. Here, the far field has a total vortex charge equal to 2, an OAM expectation value equal to $+1\hbar$ per photon and a dumb-bell-like transverse profile (Fig. 4.6(e)), that matches quite well with the result of our calculations (Fig. 4.6(f)).

When the second hologram in Fig. 4.5 is shifted downwards with respect to the beam, the phase dislocations in the near field of the second hologram will coincide. The results are shown in Fig. 4.7. The top row shows, for the $m = -1$ diffraction order, the calculated near field (Fig. 4.7(a)), an experimentally obtained far field (Fig. 4.7(b)) and a far-field profile calculated by Fourier transforming the calculated near field (Fig. 4.7(c)). The superposition of the two, oppositely-charged, vortices is indicated by the $\odot$ symbol. As the two vortices annihilate each other, a fundamental Gaussian is expected, and found, in the far field. The bottom row shows the same images for the $m = +1$ diffraction order. In the theoretical near field, the two vortices are combined to form one vortex of charge 2, indicated by the $\otimes$ symbol (Fig. 4.7(d)). The field will carry an OAM expectation value equal to $(\frac{1}{2} + \frac{1}{2})\hbar$ per photon and the far-field profile (Fig. 4.7(e)) also carries a single vortex of charge 2, greatly resembling the result of our calculations (Fig. 4.7(f)).

Finally, these experiments show that when two displaced vortices are embedded in the near field of an optical beam, simple arithmetic rules are obeyed with respect to the OAM generated by each individual vortex, the latter being predicted by Eq. (4.22). Evidently, this will hold also for the case where the number of vortices is larger than two.
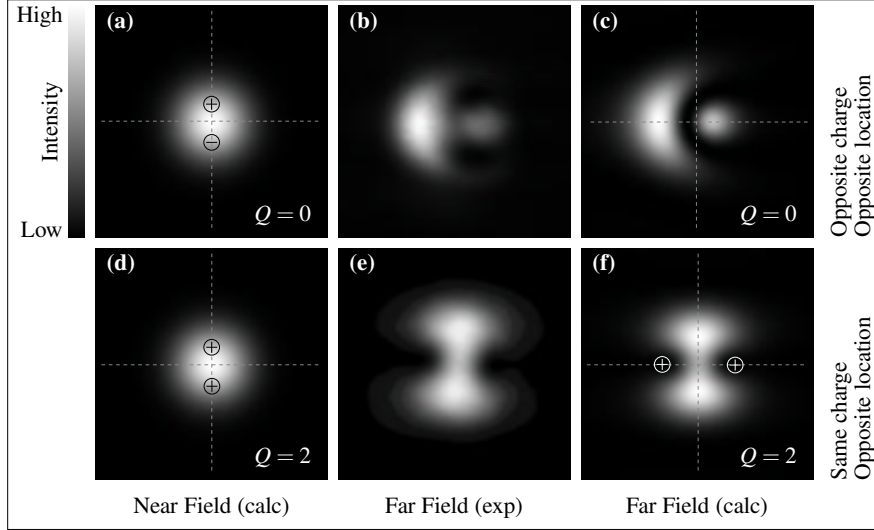
Figure 4.6: *Intensity profiles of beams with two off-axis vortices that are imprinted opposite to each other in a fundamental Gaussian beam. In the top row, the vortices have opposite charge, whereas in the bottom row, their charges are both positive. In each row, the first column shows a calculated near-field profile, where the intersection of the dashed lines indicates the centre of the beam, while the ⊕ (Q = +1) and ⊖ (Q = −1) symbols indicate the approximate positions of the positively and negatively charged vortices, respectively. The second column shows the experimentally obtained far-field intensity profile corresponding to the near fields shown in the first column. The last column shows far-field profiles that have been calculated by Fourier transforming the near fields. While (c) does not contain any vortices, the two lobes differ in phase by π.*

4.6 Conclusions

We have presented a study of the generation of optical OAM by imprinting a pure phase vortex *off-axis* in a fundamental Gaussian beam. In this context we have determined a practical method of finding the intrinsic OAM, which is useful for an arbitrary paraxial beam, as one only has to determine the near-field centre of the beam's intensity profile. We find that the intrinsic OAM of such a beam containing a single off-axis vortex is non-integer and decreases exponentially with the square of the displacement of the vortex from the centre of the beam in the near field. Note that this approach is fundamentally different from the approach using mixed screw-edge dislocation devices (cf. Chapter 5 and Refs. [5, 67]), as can be shown by performing a mode decomposition; when using the method outlined here, 5 LG components sufficiently ($\sim 88\%$) describe the $\ell = 1/2$ beam, in contrast to the 11 LG components required when using a device with a mixed screw-edge dislocation.

We have experimentally implemented our recipe for creating optical beams with non-integer intrinsic orbital angular momentum and we have compared the experimental far-field intensity profiles with those calculated using simple diffraction theory. Additionally, we have
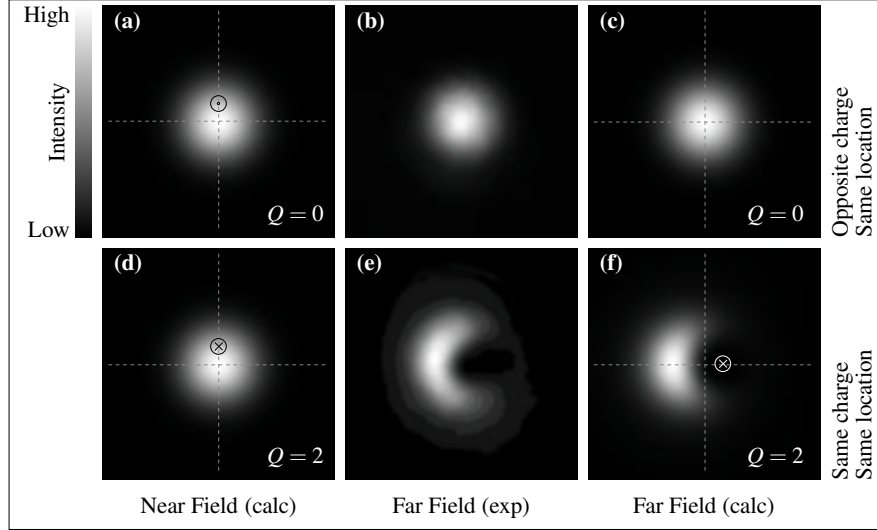
Figure 4.7: *Intensity profiles of beams with two vortices that are imprinted on top of each other in a fundamental Gaussian beam. In the top row, the vortices have opposite charge, thus effectively annihilating each other, whereas in the bottom row, their charges are positive, thus being summed. In each row, the first column shows a theoretical near-field profile where the intersection of the dashed lines indicates the centre of the beam and the ⊙ (Q = 0) and ⊗ (Q = 2) symbols indicate the approximate positions of the annihilated and summed vortices, respectively. The second column shows the experimentally obtained far-field intensity profiles corresponding to the near fields shown in the first column. The last column shows far-field profiles that have been calculated by Fourier transforming the near fields.*

experimentally embedded two vortices inside a fundamental Gaussian beam, each generating half-integer orbital angular momentum, resulting in an optical beam carrying integer orbital angular momentum. Again, these beams were investigated by comparing far-field diffraction profiles to the results of diffraction calculations and we found excellent agreement. We have also observed that the propagation of phase vortices seems similar to that of analytical vortices. Finally, we find that the contributions to the intrinsic orbital angular momentum of the individual vortices can indeed be summed to find the total, intrinsic orbital angular momentum of the beam.

Appendix

4.A The orbital angular momentum with respect to the vortex

We choose the origin of our coordinate system at the position of the dislocation, while the z_m-axis is parallel to the mth diffraction axis of the hologram. When the centre of an incident beam falls on top of the dislocation in the hologram, the mth diffraction order has acquired an OAM equal to $mQ\hbar$ per photon, as argued before. When the incident beam is now displaced with respect to the dislocation and thus with respect to the chosen origin, the OAM of both the incident and diffracted beams become, in general, different. When the incident field will have an OAM equal to L^{in} in the hologram reference frame, we intend to show that the mth-order diffracted beam contains an additional OAM equal to mQ per photon, which does *not* depend on the displacement of the beam.

For an incident beam in its own reference frame S in the plane $z = 0$, we describe the transverse field distribution by the complex function u^{in}. Assuming the incident field is *centred* on the hologram, we know that the mth diffraction order in S_m is given by

$$u_m^{\text{out}}(\vec{\rho},0) = C_m u_m^{\text{in}}(\vec{\rho},0)\exp\left(imQ\theta\right), \tag{4.23}$$

where applying Eq. (4.5b) yields $\ell_m = mQ$ for the OAM acquired after diffraction off the grating.

We now *displace* the incident beam along the transverse vector $\vec{\rho}_b$ in the plane $z = 0$ and calculate the OAM of this displaced beam with respect to the origin, which is also the location of the vortex. Applying Eq. (4.4), we find

$$
\begin{aligned}
L_m^{\text{out}} &= \frac{2\varepsilon_0}{i\omega}C_m^2 \int u_m^{\text{in}*}(\vec{\rho}-\vec{\rho}_b)\exp\left(-imQ\theta\right)\left(\vec{\rho}\times\vec{\nabla}\right)_z u_m^{\text{in}}(\vec{\rho}-\vec{\rho}_b)\exp\left(imQ\theta\right)\,\mathrm{d}\vec{\rho} \\
&= \frac{2\varepsilon_0}{\omega}C_m^2\left[\frac{1}{i}\int u_m^{\text{in}*}(\vec{\rho}-\vec{\rho}_b)\left(\vec{\rho}\times\vec{\nabla}\right)_z u_m^{\text{in}}(\vec{\rho}-\vec{\rho}_b)\,\mathrm{d}\vec{\rho} + \int mQ\left|u_m^{\text{in}}\right|^2\,\mathrm{d}\vec{\rho}\right] \\
&= C_m^2 L^{\text{in}} + 2mQ\frac{\varepsilon_0}{\omega}C_m^2\int\left|u_m^{\text{in}}\right|^2\,\mathrm{d}\vec{\rho}.
\end{aligned}
\tag{4.24}
$$

When applying Eq. (4.5b), we find that the OAM per photon of the diffracted field is the sum of the OAM per photon of the *incident* field in the hologram frame of reference, and the OAM per photon $mQ\hbar$ that has been acquired due to the dislocation of the hologram. As we intended to show, this additional OAM is independent of $\vec{\rho}_b$. A qualitative explanation is that when the displacement, i.e. the 'arm', increases, it is balanced by a reduction of transverse momentum of the output field, and the vector product of the arm and transverse momentum, i.e. the OAM, remains the same.

CHAPTER 5

Production and characterisation of spiral phase plates for optical wavelengths

We describe the fabrication and characterisation of a high-quality spiral phase plate as a device to generate optical vortices of low (3-5), specified charge at visible wavelengths. The manufacturing process is based on a molding technique and allows for the production of high-precision, smooth spiral phase plates, as well as for their replication. An attractive feature of this process is that it enables the fabrication of nominally identical spiral phase plates made of different materials, thus yielding different vortex charges. When such a plate is inserted in the waist of a fundamental Gaussian beam, the resulting far-field intensity profile shows a rich vortex structure, in excellent agreement with diffraction calculations based on ideal spiral phase plates. Using a simple optical test, the reproducibility of the manufacturing process is shown to be excellent.

5.1 Introduction

Optical waves possessing a helical phase distribution have been addressed in many studies [2, 40, 69], with applications in the cooling and trapping of neutral atoms [42], Bose-Einstein condensates [43], in the generation of vortex solitons [29, 30] and in the manipulation of small macroscopic particles [27, 28]. The helical phase distribution implies the presence of a phase singularity, also called an optical vortex, and is characterised by a locally vanishing intensity. In the vicinity of such a vortex, the complex field amplitude depends locally on the azimuthal angle θ through

$$u(r, \theta, z) = u'(r, z) \exp(iQ\theta), \tag{5.1}$$

where u' can be a complex function, r is the radial coordinate and z is the coordinate in the direction of propagation. Following a closed path around the vortex, the topological charge of the vortex is defined as [36]

$$Q = \frac{1}{2\pi} \oint \mathrm{d}\vec{l} \cdot \vec{\nabla} \chi, \tag{5.2}$$

where χ is the phase of the field. In most studies involving optical vortex fields, an optical beam in a cylindrically symmetric mode with a vortex in its centre is used. This is also the simplest example of such a field, and as such is fully described by Eq. (5.1).

Because photons in a mode of topological charge Q carry orbital angular momentum with expectation value $Q\hbar$ [5], photons in helical modes have recently attracted considerable attention. Issues that have been studied include conservation and entanglement of photonic orbital angular momentum in spontaneous parametric down-conversion [17, 54–58, 70]. The interest in the latter stems from the fact that a 'helical' photon represents a high-dimensional quantum system, thus allowing the construction of high-dimensional alphabets for quantum information [17].

Optical vortex beams can be generated quite easily by sending a higher-order Hermite-Gaussian laser beam through a combination of cylindrical lenses [2], or by diffracting a non-helical laser beam off a computer-generated hologram that itself carries a dislocation [44, 66, 71]. The latter method enjoys considerable popularity because such holograms are quite easy to fabricate. Another approach to the generation of vortex beams, involves the use of a spiral phase plate (SPP) [5, 46–48], which is the subject of the present Chapter.

5.2 Spiral Phase Plates

An SPP is an optical element that imposes an azimuth-dependent retardation on the optical field. In its simplest form, as shown in Fig. 5.1(a), it is a transparent plate of refractive index n, whose height is proportional to the azimuthal angle θ,

$$h = h_s \frac{\theta}{2\pi} + h_0, \tag{5.3}$$

where h_s is the step height and h_0 the base height of the device. This yields an azimuth-dependent optical phase delay,

$$\phi(\theta, \lambda) = \frac{2\pi}{\lambda} \left(\frac{(n - n_0) h_s \theta}{2\pi} + n h_0 \right), \tag{5.4}$$
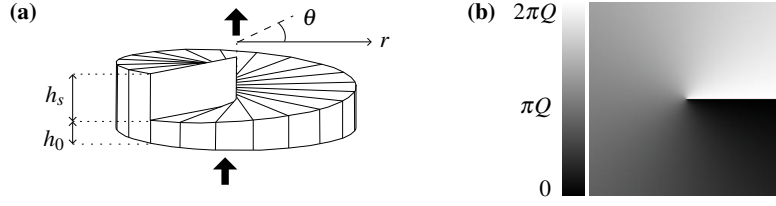
Figure 5.1: *(a) Sketch of the spiral phase plate. The top surface spirals upwards, from a height h_0 to $h_0 + h_s$. (b) The phase distribution that is imprinted onto the transverse plane of an incident beam. When Q is an integer number, the phase change at the transition from black to white is actually smooth. Otherwise, the sharp transition in gray level represents a phase discontinuity.*

with n_0 the refractive index of the surrounding medium. When such a plate is inserted in the waist of a Gaussian beam, where the phase distribution is plane, it imprints a vortex with charge $Q = h_s \left(n - n_0 \right) / \lambda$, thereby generating an output beam that carries orbital angular momentum per photon equal to $Q\hbar$. Note here that the value of Q depends both explicitly and implicitly (through the refractive index) on the wavelength of the incident light, betraying the chromatic nature of this device. The resulting phase distribution is visualised in Fig. 5.1(b).

To obtain a device able to generate beams with low values of Q, it is clear that the step height h_s of the plate should be of the order of the wavelength λ. Alternatively, the SPP can be made to be almost index-matched to its surroundings, $\Delta n = |n - n_0| \approx 0$. This approach has been followed in the original work on spiral phase plates for use in the optical regime by Beijersbergen *et al.* [5], for which $h_s \approx 0.7$ mm and $\Delta n \approx 9 \times 10^{-4}$. Index matching was achieved by immersing the SPP in a liquid, of which the refractive index was controlled by tuning the temperature. Density variations in the liquid were a major problem in that experiment. A more extreme example of this index-matching technique is provided by the recently developed SPP in the X-ray regime [47], for which $\Delta n \approx 4 \times 10^{-6}$. Here, the index matching occurs naturally.

Apart from issues related to index matching, the manufacturing difficulties of a SPP centre on *(i)* the steepness of the step, *(ii)* the central part of the SPP where, ideally, the height spirals up in a region with zero diameter, and *(iii)* the smoothness of the ramp. Indeed, the SPPs in the visible [5] and X-ray regime [47] did not have a smooth ramp, but were staircase-like. Only the first ever reported SPP had a smooth structure, but this was used at wavelengths far from the optical regime (10 µm) [46].

Here, we report on a novel manufacturing technique for SPPs for optical wavelengths based on state-of-the-art micro-machining and a molding process. Our technique is based on technologies originally developed at Philips Research Laboratories for the mass-fabrication of light-weight aspheres for the optical pick-up unit of compact-disc players [72]. In our case, it allows fabrication of multiple SPPs by replication from a master.

5.3 Production

The manufacturing technique is based on crafting a mold, which, naturally, is the 'negative' of the SPP we wish to produce. The mold is machined with a diamond tool in a piece of brass, using a modified version of the COLATH, a high-precision computer-driven lathe [73]. This lathe can be programmed to produce the surface that we require.
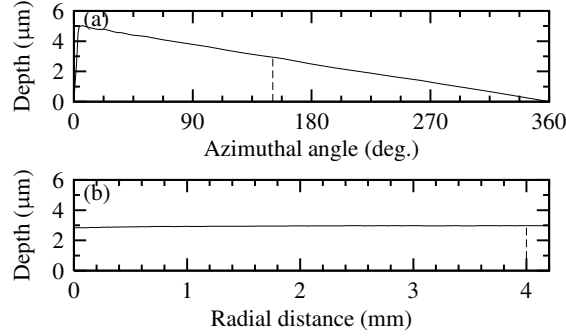

Figure 5.2: *Graphs, based upon high-accuracy data from the Zygo interferometric metrology system, demonstrating the quality of the mold. (a) The depth of the mold is plotted following an azimuthal path with a radius ≈ 4 mm, revealing a smooth ramp. The steepness of the step can also be seen clearly. There, the mold's depth increases from 0 μm to 5.07 μm over an azimuthal range of about 6°. The vertical, dashed line indicates the angular position at which the bottom graph was measured. (b) The depth of the mold is plotted along a radial path at an azimuthal angle $\approx 151°$. The deviation from the expected horizontal line is about 150 nm, which is considerably smaller than the optical wavelength where the device is designed to work (813 nm). The vertical, dashed line indicates the radial position at which the top graph was measured.*

Post-fabrication inspection of the mold is performed using a high-accuracy interferometric metrology system (Zygo); typical results are shown in Fig. 5.2. The two graphs displayed there, demonstrate the depth variations along a radial and azimuthal path across the mold, respectively. These measurements yield a value of the step height equal to 5.07 μm (design value 5.00 μm), a linear relation between the local depth h and the azimuthal angle, with a rms deviation of order 15 nm, and an azimuthal width of the step discontinuity of about 6°. Along a radial path of 4.2 mm length, the depth is seen to increase by ≈ 150 nm. Note that the mold thus deviates from its design by much less than half an optical wavelength in the visible regime. Naturally, in the central part where the height anomaly resides, deviations are larger, due to technological difficulties. The diameter of this anomaly in the mold is measured to be around 50 μm, very small compared to the overall diameter of the device (8.4 mm).

The mold is then used for the production of the SPPs, as shown in Fig. 5.3. It is first treated with stearic acid, thereby generating an anti-stick layer. Then, a 50 μm thick ring-shaped spacer is placed around the mold, whereupon the monomer of poly(ethylene glycol) dimethacrylate (PEG-DMA) is cast into the mold. A cover-glass plate, which has been treated with [γ-(Methacryloyloxy)propyl]trimethoxysilane to allow the polymer to attach to it, is then pressed onto the spacer, pushing out the excess monomer. Subsequently, the monomer
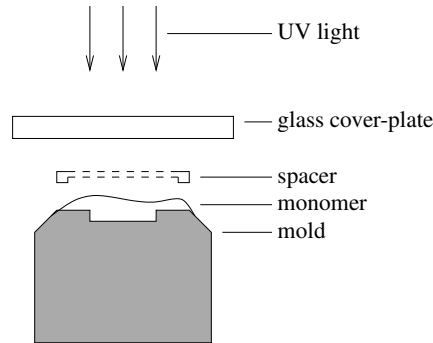
Figure 5.3: *Schematic overview of the production of a spiral phase plate. The monomer is cast into the mold and a spacer is placed around it. A glass cover-plate is pressed against the monomer and onto the spacer, after which the monomer is cured by illumination by UV light to a cross-linked polymer network.*

is cured using UV radiation from an EFOS Acticure equipped with a high-pressure mercury lamp, a fibre-optic waveguide and a filter with a transmission band of 320–390 nm. The curing takes 100 s at an intensity of 40 mW/cm^2, during which full conversion to a polymer is achieved. The usual curing requirement of a low-oxygen environment does not apply here since the monomer is sandwiched between cover plate and mold, and because it is exposed to high-intensity radiation. During the polymerisation process, the material usually shrinks (typical shrinkage in polymer-molding-process technology is roughly 3%). After release from the mold, we obtain a solid SPP with base height $h_0 \approx 50$ µm, step height $h_s \approx 5$ µm, and a refractive index at 632.8 nm of 1.495, firmly attached to a glass substrate. Naturally, any other polymer, possessing a different refractive index, can be used, yielding a SPP capable of generating a different vorticity at the same design wavelength.

5.4 Characterisation

Both the quality of the surface of the molded SPP and its transmission properties have been studied using a variety of optical methods.

An inspection of the device with the naked eye reveals that the surface is smooth, and that the step and central part where the height anomaly lies, are hardly visible. No air bubbles appear to be present inside the polymer, nor can an air layer between the glass and polymer be seen (this would betray itself by Newton's rings).

5.4.1 Reflection study

For a microscopic study of the surface, we use a phase-contrast microscope and illuminate the SPP from the top with an incandescent lamp and an interference filter ($\lambda = 549$ nm, $\Delta\lambda \approx 10$ nm), thus looking at reflected light. This method visualises height variations as interference fringes. We observe the angular spacing of the interference fringes over the SPP to be constant (see Fig. 5.4(a)), implying that the device's azimuthal ramp is linear, as
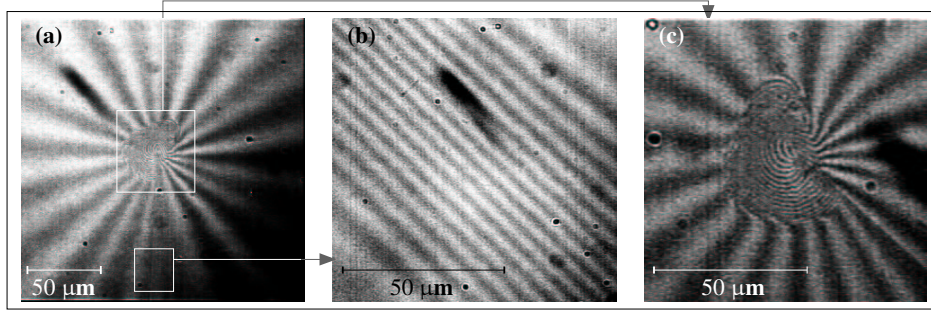
Figure 5.4: *CCD images captured with a phase-contrast microscope, looking at light (wavelength of 549 nm) reflected off the surface of a spiral phase plate, produced with the mold reported on in Fig. 5.2. (a) The fringe spacing remains constant over the angular direction of the plate. The centre is dominated by the finite size of the height anomaly. (b) Close-up of the step, located in the region indicated by the box at the bottom of (a). In reality, the part of the step that is shown in (b) lies much farther away from the centre of the device. The step has an angular width of about 6°. (c) Close-up of the height anomaly at the centre as suggested by the box in the middle of figure (a); the size of this anomaly is very small (≤ 50 μm, to be compared with the SPP's diameter of 8.4 mm). The small dots are not blemishes in the SPP , but rather in the imaging system.*

designed (cf. Eq. (5.3)). This is more clearly demonstrated by Fig. 5.5, where the fringes have been translated into height variations and plotted against their azimuthal position. From this data, we find the step height h_s to be $\approx 5.05 \pm .07$ μm. This measurement implies, surprisingly, that the polymer has either not shrunk or very little, much less than the value of 3%, assumed to be typical.

In order to study the step discontinuity of the SPP, we look at it far away from the centre. This is shown in Fig. 5.4(b), where we observe a fringe pattern in an angular width of 6°, where the height changes rapidly.

The area where the interference pattern is irregular, corresponds to the imperfect centre of the device, i.e. the region of the height anomaly. It can be seen clearly in the close-up of Fig. 5.4(c), and has approximately the same size as in the mold (≈ 50 μm). The error caused by this region of uncontrolled height is expected to be small, as long as the width of an incident beam is much larger than 50 μm.

5.4.2 Transmission study

The imprinted vorticity on a fundamental Gaussian beam is not apparent in the intensity distribution in the near field of the imprinting device. This is due to the fact that, although the beam has been phase shifted, the beam has only propagated over a few wavelengths thus has not had a chance to interfere with itself. A *far-field intensity pattern*, however, reveals all phase (and intensity) variations of the near field and enables us to probe the quality of the SPP [5]. Due to the chromaticity of the device, we expect that the vortex charge Q and therefore the far-field profiles vary as a function of the wavelength of the input beam. Therefore, we
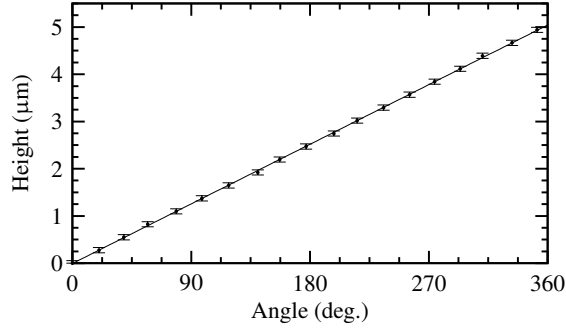
Figure 5.5: *Graph demonstrating the quality of the SPP's ramp. The angular position of each dark fringe on the ramp as occurring in Fig. 5.4(a) is measured, converted to a height and plotted as points in this graph. The line shows a linear fit, demonstrating the excellent linearity of the ramp.*

have recorded far-field profiles for our SPP at different input wavelengths. Here, we use as a bright white light source a combination of a femtosecond mode-locked Ti:Sapphire laser (Coherent Vitesse) and a micro-structured fibre of 1 m length with a 1.7 μm core diameter (Crystal Fiber A/S) [74]. The white light generated in the micro-structured fibre is spatially filtered using a single-mode fibre (Newport F-SA, cut-off wavelength of 400 ± 50 nm) to obtain a beam close to a fundamental Gaussian. Subsequently, this beam is spectrally filtered employing a set of narrow-band interference filters, each having a bandwidth ≤ 10 nm. Thus we obtain a quasi-monochromatic Gaussian beam of variable wavelength with good spatial coherence to study the phase-modifying effects of the SPP. This beam is made to pass through the SPP, after which the far field of the resulting beam is imaged onto a CCD camera. The results are shown in the top frame of Fig. 5.6[1]. As can be seen, the first two profiles (in Fig. 5.6(a),(b)) taken at wavelengths 540 nm and 674 nm, show zero-intensity spots lying close together near the centre, and one lying off-centre, to the right, all caused by phase singularities [5]. The former correspond to the integer part of the topological charge of the field. The latter, isolated phase singularity, corresponding to the non-integer part of the charge Q, has been pushed off-centre in the horizontal direction, a phenomenon that occurs due to the upwards oriented edge discontinuity in the near-field phase distribution [59]. The presence of this off-centre intensity zero leads us to conclude that for these wavelengths (540 nm and 674 nm), the step height of the phase plate gives rise to an optical phase jump that is *not* a multiple of 2π. The diffraction pattern observed at 813 nm, as seen in Fig. 5.6(c), shows a reasonably nice doughnut shape and does not display an off-centre isolated intensity zero. We can therefore conclude that at this wavelength, the optical phase jump is almost exactly equal to $2\pi Q$ with Q an integer number.

In order to better assess the quality of our device, we compare our results with calculated far-field patterns. To calculate these, we model the input beam as a Gaussian amplitude and plane phase distribution and let this beam impinge on an ideal (i.e. free of manufacturing constraints) SPP with vorticity Q. This ideal SPP is so thin that propagation aspects inside

---

[1]The imaging of these far-field profiles has been greatly improved some time after this experiment. A good example is given in Fig. 6.2.
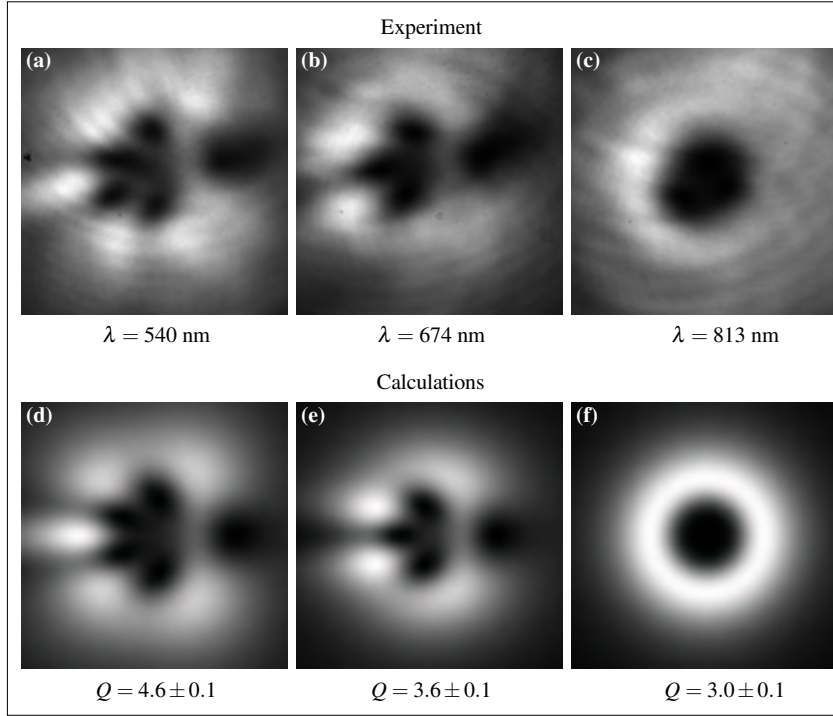
Figure 5.6: *Far-field diffraction patterns of fundamental Gaussian beams of different wavelengths, after having passed through the spiral phase plate with its step oriented upwards (top), and calculated far field diffraction patterns with different values of Q (bottom). Black and white correspond to low and high intensity, respectively. For each of the calculated patterns, the value of Q (given below the pattern) was adjusted so that they visually match the experimentally obtained diffraction patterns. The zero intensity spots near the centre and those to the right in both the experimental and calculated patterns correspond to phase singularities.*

the device can be ignored. The output field is then Fourier transformed, resulting in its far field. For each wavelength used in the experiment, such far-field intensity distributions were calculated and made to visually match the profile found in the experiment by adjusting the value of Q only. The results are shown in Fig. 5.6(d),(e),(f). We can conclude that the experimentally obtained images agree quite well with the calculations. The same experiment was repeated for an SPP produced in the same mold with a different polymer, yielding different vorticities. Also for this device, a good agreement with the calculations was achieved. Calculations that take the angular width of the step into account, reveal no fundamental changes in the structure of these far-field patterns, justifying the comparison of the experimental SPP device with an 'ideal' SPP device.

It is well known that replicated optics can exhibit considerable (stress-induced) birefringence. In order to assess whether the SPPs replicated with the presently used technology are birefringent or not, we have inserted one such device in an optical beam between two crossed

polarisers. Regardless of the orientation of the SPP in this setup, the intensity is measured to be less than $5 \cdot 10^{-5}$ of the incident intensity. We thus conclude that our SPPs are highly polarisation isotropic.
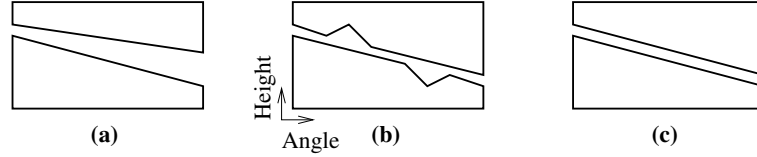
5.4.3 Reproducibility

Figure 5.7: *Diagram demonstrating how errors in the structure of the phase plates may be detected by combining devices from the same mold in such a way that, ideally, the effect of the two devices cancels. (a) If reproducibility is bad, e.g. each device shrinks differently during polymerisation, the devices will not complement each other. (b) If the ramp of one device contains a flaw, the second device will also contain that flaw, but at a different angular position. (c) Perfect devices and a perfect reproducibility are assumed; the SPPs complement each other.*

A last point that we checked is the reproducibility of the molding process. The idea is to use a SPP to imprint a certain vorticity onto a fundamental Gaussian beam and, by employing a nominally identical SPP with the same orientation but with opposite vorticity, to correct the phase pattern created by the first, positive vorticity plate, thereby reconstructing the original beam. Thus, when the SPPs do not complement each other, the original beam is not reconstructed, as illustrated in Fig. 5.7. An opposite vorticity SPP is easily obtained by fabricating a second device from the same polymer in the same mold, and then flipping it about the axis defined by the step, as shown in Fig. 5.8.
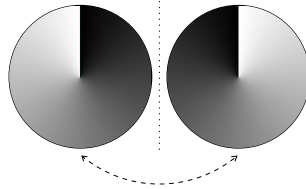

Figure 5.8: *Illustration of how to invert the vorticity of a SPP. The left device, with a clockwise vorticity as indicated by the gray-scale gradient, is flipped by $180°$ about the vertical dotted line, which is parallel to the step. The result is the device on the right, with a counter-clockwise vorticity.*

This procedure has been implemented in the following experiment. A HeNe laser beam is allowed to propagate through two of the previously specified SPPs (for which Q is non-integer at $\lambda = 633$ nm), placed in each other's near field with a f-$2f$-f telescope, as shown in Fig. 5.9. The resulting beam is then coupled into a single-mode fibre, only allowing a fundamental Gaussian beam to propagate, and the output power is measured. Without the SPPs, this power is measured to be 58% of the power emitted by the laser. With the SPPs
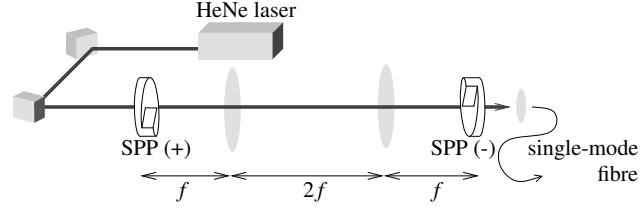
Figure 5.9: *Setup to test the reproducibility of the SPPs. A HeNe beam is allowed to propagate through two nominally identical, opposite-vorticity SPPs, placed in each other's near field. The output beam is coupled into a single-mode fibre. The beam intensity after the fibre is found to be 98% of the intensity in the case that there are no SPPs inserted in the beam.*

present and after correction for reflection losses of the SPPs, we find a value of 57% of the laser power. Naturally, the throughput is sensitive to the precise alignment of the two SPPs. For instance, if one SPP is translated in the transverse direction over a distance of 10% of the width of the incident beam, the throughput is decreased by a factor of approximately two.

From the normalised transmission of 0.98, we conclude that the optical beam after the second SPP is Gaussian. This is substantiated by measurements of the far-field profile (cf. Fig. 6.3). If the SPP would not have been reproducible, e.g. each device polymerised and shrunk differently, the transmission would not have been so high. This is illustrated in Fig. 5.7(a). The normalised throughput value of 0.98 may be used as a quantitative measure of the replication process, implying that the mold is extremely well-suited for reproducible production of SPPs.

This result supports our claim that the phase pattern imprinted by the SPP deviates only very little from the ideal. Namely, any flaw would occur in *both* SPPs at the *same* location. As one SPP is inverted by flipping it as shown in Fig. 5.8, the single flaw will occur at two different locations in the imprinted phase, as shown in Fig. 5.7(b). If then also the reproduction would be inaccurate, as suggested by the diagram of Fig. 5.7(a), the results in this experiment would be disastrous. The fact that the reconstructed beam has such high overlap with the original incident Gaussian beam, proves that the ramp is as smooth as it can be, and that reproduction of the SPP is accurate; thus the quality of the devices is excellent, approaching that of ideal SPPs.

This experiment also demonstrates that these SPPs are ideal for adding and subtracting vorticity from a field, thus providing the possibility of combining devices to generate lower-order optical vortices; a combination of two SPPs produced from the same mold, but made of polymers with slightly different refractive indices, can achieve exactly that.

5.5 Conclusions

We have described the production of a spiral phase plate with a smooth ramp, capable of generating optical beams of low-order vorticity. We have discussed both the manufacture of the mold and the fabrication of the plate itself. Several diagnostic methods were used to scrutinise the optical quality of the device and the smoothness of the surface, all leading to

the conclusion that the produced spiral phase plate is of very high quality. The replication process is excellent, producing identical plates with a modal accuracy of $> 98\%$ in a first try. Additionally, it allows for production of devices with different vorticity from the same mold, the vorticity depending on the choice of polymer. It then becomes possible to combine several plates to achieve, in principle, any desired topological charge. We are confident that these plates can be used in the study of phase singularities, and the orbital angular momentum of classical light and that of single photons.

Acknowledgements

CHAPTER 6

Half-integer spiral phase plates for optical wavelengths

We have fabricated high-quality, half-integer spiral phase plates for generating optical vortices at near-infrared wavelengths. When inserted in the waist of a fundamental Gaussian beam, such a device gives rise to a rich vortex structure in the far field. The near-perfect cancellation of the effect induced by two nominally identical phase plates shows that we have excellent control of the manufacturing process. The plates that are discussed in this Chapter are different from the ones presented in Chapter 5; these plates are used in the quantum-mechanical experiment described in Chapter 8.
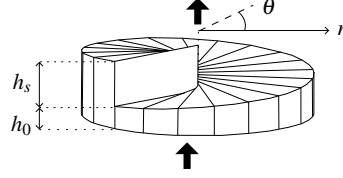
Figure 6.1: *Sketch of a spiral phase plate. The top surface spirals upwards, from a height h_0 to $h_0 + h_s$.*

6.1 Introduction

When the phase distribution of an optical beam is helical the beam carries orbital angular momentum along its direction of propagation. Such a beam contains a phase singularity, also called an optical vortex; the intensity vanishes at this singularity. In a transverse plane, the field can be written in the polar decomposition,

$$u(r,\theta) = |u(r,\theta)| \exp\left(i\chi(r,\theta)\right). \tag{6.1}$$

Following a closed path around the singularity, the topological charge of the vortex is defined as [36]

$$Q = \frac{1}{2\pi} \oint d\vec{l} \cdot \vec{\nabla}\chi, \tag{6.2}$$

where χ is the phase of the field. In most studies involving fields with a helical phase distribution, one uses an optical beam in a cylindrically symmetric mode with a vortex in its centre. Photons in such a mode carry orbital angular momentum (OAM) with expectation value $Q\hbar$, Q being integer valued [5]. Presently, such photons enjoy great popularity, since a helical photon can be viewed as a high-dimensional quantum system, allowing the construction of high-dimensional alphabets for quantum information [17]. This possibility has been the driving force behind studies of the conservation and entanglement of photonic orbital angular momentum in spontaneous parametric down-conversion [17,54–58].

Optical vortex beams can be generated quite easily by diffracting a non-helical laser beam off a computer-generated hologram that itself carries a dislocation [66, 71], or off a spiral phase plate (SPP) [5,46–48]. We have chosen the latter route.

An SPP is a transparent plate of refractive index n, whose height (thickness) is proportional to the azimuthal angle θ (see Fig. 6.1),

$$h = h_s \frac{\theta}{2\pi} + h_0, \tag{6.3}$$

where h_s is the step height and h_0 the base height of the device. When such a plate is inserted in the waist of a Gaussian beam, where the phase distribution is plane, it imprints a vortex charge $Q = h_s (n - n_0) / \lambda$; the output beam thus carries orbital angular momentum per photon equal to $Q\hbar$. The vortex charge that such a device imprints on an optical beam can be tuned by modifying either the optical step height $h_s(n - n_0)$ or the optical wavelength λ.

Due to this tunability it is simple to design an SPP so that, at a specific wavelength λ, the optical step height $h_s(n - n_0)$ is an *odd multiple* of $\lambda/2$. In the mode that arises when a

Gaussian beam is diffracted off such an SPP, the orbital angular momentum per photon has an expectation value that is half-integer. Since this mode can be expanded in Laguerre-Gaussian modes [5], the photon can be viewed as an *N*-dimensional quantum system, i.e. a qu*N*it; this explains our interest in the half-integer OAM case in particular. In the present Chapter we explore the use of a high-quality SPP for generating such photons.

The manufacturing requirements on a SPP as sketched in Fig. 6.1 are quite severe because *(i)* the physical step it carries should be infinitely steep, *(ii)* its height in the centre should spiral up in a region of zero diameter, and *(iii)* its surface should be completely smooth along the spiral. Additionally, to generate a beam with low vorticity, the optical step height $h_s(n - n_0)$ should be of order λ. The latter condition can be met in two ways: the step height h_s is on the scale of the wavelength, which sets very high requirements on the machining precision when the wavelength is in the visible, or the plate is almost (but not quite) index matched to the surrounding medium ($n - n_0 \approx 0$) [5, 47]. At visible wavelengths the latter approach requires liquid or solid immersion, resulting in an optical step height that is strongly temperature dependent [5].

A technique that meets the manufacturing challenges of an SPP for optical wavelength is photopolymerisation in a mold as used, for example, for compact disc lenses [75]. A strong point of this approach is that the use of a mold allows for the production of a large set of identical SPPs. Additionally, by using different polymers, it allows for the fabrication of SPPs that are geometrically identical but have variable optical step height. Here we present experimental results for SPPs fabricated with this technique.

6.2 Polymer SPP

In a replication technology such as photopolymerisation, the shape accuracy of the final product is determined by the precision of the mold that is used. In our case this mold is machined in a piece of brass in the complementary shape of the SPP, employing a diamond tool on a high-precision computer-driven lathe [73]. Inspection by optical interferometry shows that the mold is very close to ideal in terms of smoothness of the spiral. In the device's centre, obviously, the mold can not conform to the ideal because the diamond tool has a finite size. This gives rise to a central 'anomaly' with a diameter of ≈ 300 μm, very small compared to the overall diameter of the SPP (8.4 mm). Also the step is not infinitely steep; instead the step has an azimuthal width of $\approx 6°$.

Into this mold a pre-polymer of poly(ethylene glycol) dimethacrylate (PEG-DMA-875) is cast, which is then UV cured. This yields an SPP with a step height of $5.78 \pm .07$ μm. Using optical interferometry we find that the device has a vorticity at $\lambda = 813$ nm equal to $Q \approx 3.48 \pm 0.02$, very close to the design value $Q = 3.5$.

6.3 Half-integer spiral phase plate

The far-field diffraction pattern of the SPP inserted in the waist of an almost collimated Gaussian beam at $\lambda = 813$ nm is shown in Fig. 6.2. The picture on the left shows the intensity distribution (above) and a 3-D representation (below) of the experimental results while the
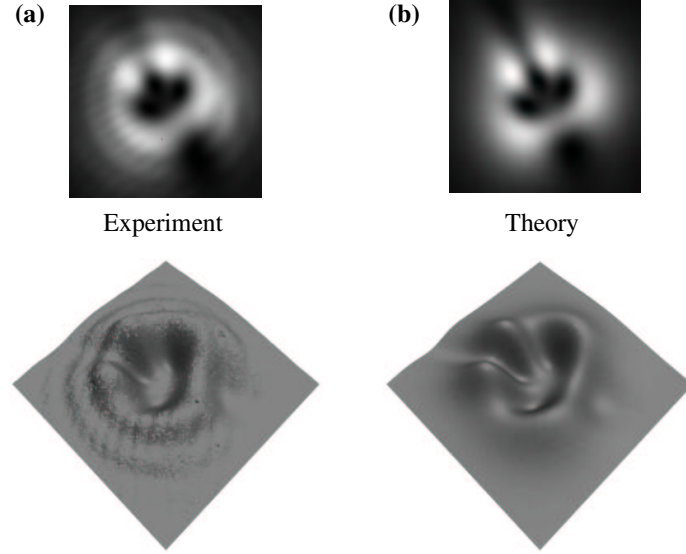
(a) **(b)**

Experiment   Theory

Figure 6.2: *Intensity profiles (above) and 3-D representations (below) of the far-field diffraction pattern of an $Q = 3.5$ spiral phase plate for a Gaussian input beam at $\lambda = 813$ nm. (a) The experimental result is shown on the left, while (b) the picture on the right shows the result of a diffraction calculation.*

picture on the right shows the corresponding results of a diffraction calculation for a blemish-free spiral phase plate with vorticity $Q = 3.5$. The intensity pattern is ring like with three slightly separated regions of very low intensity inside. Each of these regions surround a phase vortex. An additional vortex is found outside the high-intensity ring. Diffraction calculations show that the far-field position of the latter vortex provides a direct measure of the fractional part of the beam's vortex charge; in the present case this fractional part equals 0.5. The agreement between the experimental and calculated far-field patterns is excellent, demonstrating that our SPP is eminently suited for generating high-quality vortex beams.

The action of any non-dissipative optical element on a diffracting beam can be undone by inserting a conjugate optical element in the same Fourier plane as the first. Basically, this is a test of unitarity. The conjugate element of a fault-free SPP is another SPP with opposite helicity. This is simply an identical phase plate, oriented in reverse (e.g. the ramps of the two devices face each other). Ideally, the far field of the second SPP is then identical to that of the original beam. Because each SPP introduces a step in the phase of the transmitted light, it is important that the steps are perfectly aligned. This argument applies for any wavelength, independent of the value of Q.

To evaluate the unitarity of our non-ideal SPPs we send a Gaussian beam at $\lambda = 632.8$ nm through two oppositely oriented half-integer SPPs replicated in the same mold, positioned in each other's near field. The far-field of the second SPP is nicely round and is very well represented by a Gaussian intensity distribution (see Fig. 6.3). This is made quantitative by noting that this output field can be coupled into a single-mode fibre with almost the same efficiency as the original input field (0.98 coupling-efficiency ratio).
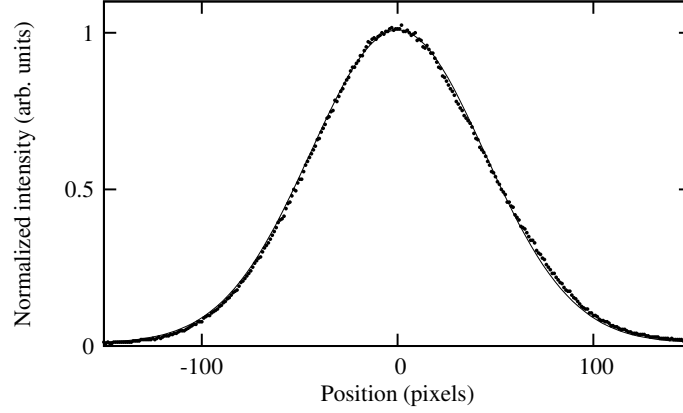
Figure 6.3: *Cut through the far-field profile of a Gaussian beam upon having passed through two oppositely-oriented half-integer, nominally identical spiral phase plates. The points show the experimental data; the curve represents a Gaussian distribution. The error bars are of the size of the individual points.*

These results strongly suggest that our SPPs indeed act as unitary optical elements. This implies that the non-ideal features (the anomaly at the centre, the residual surface roughness) of our SPPs do not play an important role. This experiment also demonstrates that our SPPs are ideally suited for adding and subtracting vorticity from a field, thus providing the possibility of combining devices to generate phase singularities with arbitrary dislocation strength; a combination of two SPPs, for instance produced from the same mold but made of polymers with slightly different refractive indices, can achieve exactly that.

6.4 Conclusions

We have employed the technique of UV embossing to craft spiral phase plates for visible wavelengths, designed to generate optical beams of low-order vorticity. These plates have, as a distinguishing characteristic, a half-integer vorticity. We have studied the diffraction properties of the resulting phase plates both individually, and as a matched pair. All tests indicate that the produced spiral phase plates are of very high quality and replicate very well. We are confident that these plates with half-integer vorticity can be of great use in the study of high-dimensional entanglement (cf. Chapters 7 and 8).

Acknowledgements

CHAPTER 7

Violation of local realism in a high-dimensional two-photon setup with non-integer spiral phase plates

We propose a novel setup to investigate the quantum non-locality of orbital angular momentum states living in a high-dimensional Hilbert space. We incorporate non-integer spiral phase plates in spatial analysers, enabling us to use only two detectors. The resulting setup is somewhat reminiscent of that used to measure polarisation entanglement. However, the two-photon states that are produced, are not confined to a 2×2-dimensional Hilbert space, and the setup allows the probing of correlations in a high-dimensional space. For the special case of half-integer spiral phase plates, we predict a violation of the Clauser-Horne-Shimony-Holt version of the Bell inequality ($S \leq 2$), that is even stronger than achievable for two qubits ($S = 2\sqrt{2}$), namely $S = 3\frac{1}{5}$.

7.1 Introduction

Recently, the orbital angular momentum (OAM) of light has drawn considerable interest in the context of quantum-information processing. The spatial degrees of freedom involved in OAM [2] provide a high-dimensional alphabet to quantum information processing (i.e. qu*N*its instead of qubits) [10, 17]. Additionally, since OAM is associated with the topology of the electromagnetic field, the use of this observable in quantum entanglement may lead to states that are inherently robust against decoherence [76].

The most popular OAM analyser when dealing with conservation, correlation and entanglement of OAM consists of a so-called fork hologram [45], i.e. a binary phase hologram containing a fork in its centre [66], together with a spatial-mode detector consisting of a single-mode fibre connected to a single-photon detector; such analysers have been used in the three-dimensional case, i.e. $N = 3$, by Vaziri *et al.*, [10]. In that experiment, proof of entanglement of the OAM degree of freedom of two photons was given by showing that a generalised Bell inequality was violated; this scheme requires 6 detectors, namely 3 in each arm, and one has to measure 3×3 coincidence-count rates [10] to perform a measurement for a single setting of the analysers.

In the present Chapter, we consider the use of spiral phase plates (SPPs) [5] instead of phase holograms in an OAM entanglement setup, enabling us to investigate high-dimensional entanglement with only *two* detectors. More specifically, we will consider SPPs that impose on an optical beam a *non-integer* OAM expectation value per photon, in units of $\hbar$ [5]. With such devices, combined with single-mode fibres to form quantum-state analysers, we propose to build an OAM-entanglement setup that is reminiscent of the usual setup to measure polarisation entanglement [77], where the rotational setting of the analysers (polarisers in that case) is varied. We will show that it is possible to identify SPP analyser settings, in the spirit of horizontally and vertically aligned polarisers, when using *half*-integer SPPs, allowing observation of high-dimensional entanglement ($N > 2$), in contrast to the polarisation case ($N = 2$). These claims are supported by calculations; we predict highly non-classical quantum correlations ($S = 3\frac{1}{5}$), i.e. stronger quantum correlation between two photons than the maximum correlation between two qubits ($S = 2\sqrt{2}$).

7.2 Spiral phase plates

A SPP, shown in Fig. 7.1(a), is a transparent dielectric plate with a thickness that varies as a smooth ramp, thus phase shifting an incident field linearly with the azimuthal angle θ [5]. As can be seen, the plate carries a screw discontinuity, expressed by the spiralling thickness, and an edge discontinuity, i.e. a radially oriented step with height h_s. The difference between the maximum and minimum phase shift is written as $2\pi\ell$, where ℓ is not necessarily integer; in fact, ℓ depends on the step height h_s, the difference in refractive indices of the SPP and surrounding medium, and the wavelength of the incident light [5]. Thus, a photon propagating through this plate will acquire an OAM with expectation value equal to $\ell\hbar$ [3,5]. Placing such a plate in the waist of Laguerre-Gaussian beam, the field in the exit plane just behind the plate will be described by

$$\langle r, \theta | \hat{S}(\ell) | l, p \rangle = u_{lp}^{\mathrm{LG}}(r, \theta) \exp(i\ell\theta), \tag{7.1}$$
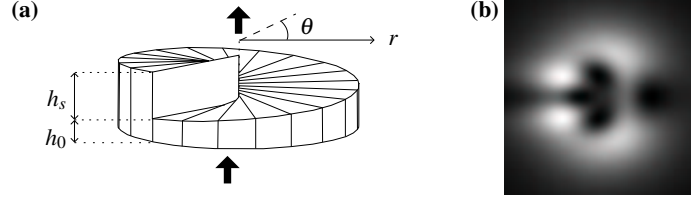
Figure 7.1: *(a) Schematic drawing of a SPP. The device shifts the phase of an incident beam proportional to the azimuthal angle θ. (b) A calculated far-field diffraction pattern of a fundamental Gaussian beam after propagating through an $\ell = 3\frac{1}{2}$ plate positioned in its waist plane, showing that rotational symmetry is broken. Black and white denote low and high intensity, respectively.*

where $|l, p\rangle$ are the Laguerre-Gaussian (LG) field states and $\hat{S}(\ell)$ is the operator representing the effect of the SPP on the input mode. Note that we have neglected the uniform phase shift that is caused by the SPP's base with height h_0, since it acts as a plane-parallel plate. By adding another plane-parallel plate with the appropriate thickness, the total phase shift of these two can be made equal to an integer multiple of 2π.

The function $u_{lp}^{\mathrm{LG}}(r, \theta)$ in Eq. (7.1) is the complex amplitude of the LG beam in its waist plane, given by [2]

$$
\begin{aligned}
\langle r, \theta | l, p \rangle &= u_{lp}^{\mathrm{LG}}(r, \theta) \\
&= C_{lp}^{\mathrm{LG}} \left(\frac{r\sqrt{2}}{w_0} \right)^{|l|} L_p^{|l|} \left(\frac{2r^2}{w_0^2} \right) \exp\left(-\frac{r^2}{w_0^2} \right) \exp(il\theta),
\end{aligned}
\tag{7.2}
$$

where w_0 is the waist radius, $L_p^l(x)$ an associated Laguerre polynomial [68] and C_{lp} a normalisation constant. In the paraxial limit, the LG free-space modes, enumerated by the (integer) indices l and p, form a complete basis of spatial modes. The LG index l, which should not be confused with the SPP's step index ℓ, is related to the OAM that is carried in that LG mode, namely $l\hbar$ per photon [2,3,5], while the index p provides information on the number of nodes along a transverse radius of the mode.

When placing a SPP in a beam in a single LG mode, the output will generally be in a *superposition* of LG modes and the beam profile will be no longer invariant under free-space propagation, due to the difference in Gouy phase of the individual LG components. For integer values of the step index ℓ of the SPP, the edge discontinuity is effectively absent and this superposition will only be with respect to the LG index p [5, 63]. In that case, the intensity distribution of the mode will be doughnut-shaped in the far field. For non-integer ℓ values, the edge discontinuity does not vanish and the superposition of modes will also be with respect to the index l, which is related to the OAM of the mode [5]. Such superpositions consist in principle of an infinite number of LG components. Effectively, this number is finite and increases with ℓ; as an example, if $\ell = \frac{1}{2}$, the overlap intensity with 11 LG components is 87%, while for $\ell = \frac{5}{2}$, 224 LG components are required to reach the same level of overlap[1].

---

[1]The LG components are enumerated by two indices, l and p, which enumerate the OAM mode and the radial distribution, respectively. Thus to find the OAM dimensionality, summation over p is required.

As SPPs with non-integer ℓ can *create* such high-dimensional superpositions of OAM modes, we anticipate that, when employed suitably, they can also *project* onto such superpositions. We therefore propose to incorporate such non-integer SPPs in analysers for OAM states living in a high-dimensional Hilbert space.

From a topological point of view, SPPs with non-integer ℓ imprint a mixed screw-edge dislocation on an incident field. The result is rotational asymmetry of the imprinted phase distribution and thus of the emerging field, which becomes visible in the far-field intensity profile (Fig. 7.1(b)). It is the orientation of the step in the transverse plane, that we wish to exploit as an analyser setting in a new bipartite entanglement scheme.

Since ℓ shall be chosen to have a non-integer value, it is important to realize that, when an incident field passes through an SPP in combination with its *complement* (i.e. a SPP with the same step height and orientation, but an *inverted* vorticity), the beam basically passes through a plane-parallel plate that shifts the phase of the field, in an azimuthally uniform way, by $2\pi\ell$,

$$\hat{S}^{\text{compl}}(\ell)\hat{S}(\ell) = \exp\left(i2\pi\ell\right)\hat{I}, \tag{7.3}$$

where $\hat{I}$ is the identity operator and where we keep the exponent since $\exp\left(i2\pi\ell\right) \neq 1$ for non-integer ℓ. It is convenient to identify the complementary SPP, which *physically complements* the SPP action, with the Hermitean conjugate $\hat{S}^{\dagger}(\ell)$ of the SPP operator, which *quantum-mechanically reverses* the SPP action. Since $\hat{S}(\ell)$ is unitary, it follows that

$$\hat{S}^{\text{compl}}(\ell) = \exp\left(i2\pi\ell\right)\hat{S}^{\dagger}(\ell). \tag{7.4}$$

As $\hat{S}^{\dagger}(\ell)$ and $\hat{S}^{\text{compl}}(\ell)$ only differ by a multiplicative phase factor we can again use a plane-parallel plate in the experiment to compensate for this phase factor. Similar to the uniform phase shift caused by the SPP's base h_0, we will neglect this phase shift as well, as it can be trivially dealt with. Henceforth, the operator for the compensating SPP, with inverted vorticity, will be represented by the operator $\hat{S}^{\dagger}(\ell)$.

7.3   Proposal for an experiment

In the experiment on OAM qutrits ($N = 3$), fork holograms were used [10]. Those holograms can only modify the OAM expectation value by an *integer* number[1], depending on the diffraction order of the hologram. It also required the use of *three* analysers in each arm of a spontaneous-parametric-down-conversion (SPDC) setup. In contrast, our proposed OAM-entanglement experiment uses *non-integer*-SPP-state detectors and only requires a *single* analyser-detector combination in each arm. This scheme is shown in Fig. 7.2; it has been inspired by the setup used in polarisation entanglement [77]. The SPPs that are inserted in the two arms should be chosen to obey conservation of OAM (see also Section 7.6). Thus, if the classical pump beam does not contain any OAM, a typical choice for the signal and idler SPPs would be to have step indices ℓ and $-\ell$ respectively, where, in our case, ℓ should have a non-integer value. The role of the lenses in signal and idler path, L_s and L_i respectively, will be discussed in Section 7.6. Finally, single-mode fibres are indicated by F_s and F_i.

---

[1]The OAM expectation value is integer when the fork hologram is used normally, i.e. centred. See Chapter 4 on how to use these devices such that the OAM expectation value becomes non-integer. There also exist holograms
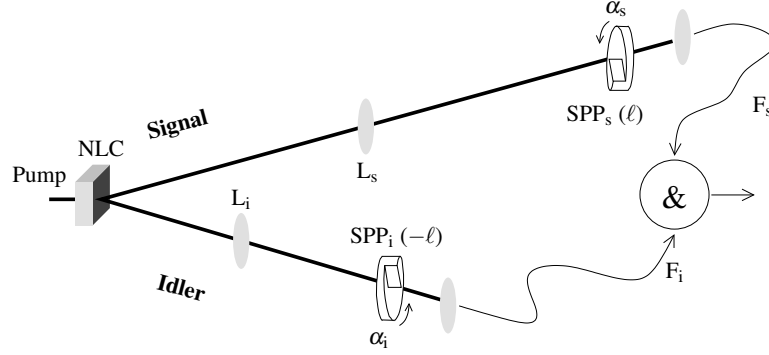
Figure 7.2: *Proposed experimental setup. A nonlinear crystal (NLC) splits a pump photon in a signal photon and an idler photon by the process of SPDC. In each path, a SPP (SPP$_{s,i}$) is inserted with a single-mode fibre F$_{s,i}$, together forming the analyser. The coincidence-count rate of detectors is measured as a function of the SPPs' angular settings α_s and α_i.*

By manipulating the transverse axes of our analysers, namely the SPP steps, we have access to various photon states that live in a high-dimensional OAM Hilbert space, as mentioned earlier. We may orient these edges arbitrarily in the transverse plane, as shown in Fig. 7.2, thus allowing their use as angular analysers. When combined with a single-mode fibre, the SPP with step index ℓ, set at an azimuthal angle α_s, projects the incident photon state out onto the OAM state with expectation value $-\ell$ with edge angle α_s. As we will argue in Section 7.6, the coincidence-count rate will depend, like in polarisation entanglement, only on the *relative* angle of the transverse axes.

We stress that, in spite of the superficial similarity between a polariser and a non-integer SPP, they are of course very different devices; for example, while polarisation corresponds to *alignment*, the SPP edge corresponds to *orientation*. In other words, with a polariser, one can analyse the alignment of the electrical field oscillation, either horizontal or vertical, thus yielding a periodicity of π when rotated. With a SPP with non-integer ℓ one can analyse the spatial orientation of a field, thus yielding a periodicity of 2π when rotated (see e.g. Fig. 7.1(b)). Thus we expect that the coincidence-count rate will have a periodicity of 2π when one of our analysers is rotated.

An equally important difference between the two cases is that, whereas polarisation Hilbert space is two dimensional, OAM Hilbert space is infinite dimensional. As we will see, this makes rotation of SPPs fundamentally different from rotation of a polariser. In order to address these aspects explicitly, we need a basis of the OAM Hilbert space that is suited for our purpose.

---

that can generate mixed screw-edge dislocations in optical fields, thus modifying the OAM expectation value by non-integer numbers. For these holograms, see Ref. [67].
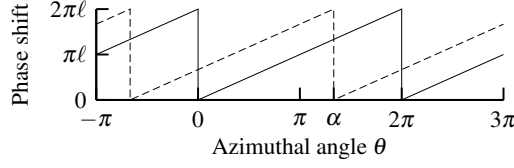
Figure 7.3: *Plot of the phase shift imprinted by a SPP as a function of the azimuthal angle. The solid line shows this shift for a plate with its edge oriented at $\theta = 0$, while the dashed line shows the phase shift for a plate with its edge at $\theta = \alpha$.*

7.4 Non-integer-OAM states

Our aim is to construct a complete, orthonormal basis that contains non-integer-OAM states as basis elements. To this end, we consider all states in the polar representation and separate the radial and angular parts, so that the arbitrary state $|r, \theta\rangle$ can be written as $|r\rangle|\hat{r}\rangle$, where we have introduced the *direction* (i.e. angular) ket $|\hat{r}\rangle$. This allows us to introduce a complete basis set of angular states, the eigenstates $|l\rangle$ of the OAM operator $\hat{L}_z$, so that $\hat{L}_z|l\rangle = l|l\rangle$. A Laguerre-Gaussian state can thus be separated into a radial and angular part, so that $|l, p\rangle = |\rho_{lp}\rangle|l\rangle$, where $|\rho_{lp}\rangle$ is the radial part of the state, which is of less importance in this Chapter. The OAM eigenstates can be transformed from integer to non-integer-OAM states. By applying a unitary operator to the integer-OAM basis, its completeness and orthonormality are conserved; the unitary operator that we use is the SPP operator, introduced in Eq. (7.1):

$$\langle\hat{r}|\hat{S}(\lambda)|l\rangle \equiv \langle\hat{r}|a_\lambda^{(l)}\rangle = \frac{1}{\sqrt{2\pi}}\exp\left[i(l+\lambda)\theta\right]. \tag{7.5}$$

The new basis $\left\{|a_\lambda^{(l)}\rangle\right\}$ has its components enumerated by l, each with OAM equal to $(l + \lambda)\hbar$, where $\lambda \in [0, 1)$ is a constant (not to be confused with the wavelength of the light). Different values of λ define different bases of OAM Hilbert space, each basis being complete and orthonormal.

As an example, passing a photon in a fundamental Gaussian mode $|0, 0\rangle = |\rho_{00}\rangle|0\rangle$ through a SPP with $\ell = \frac{2}{3}$, creates the state $|\rho_{00}\rangle|a_{2/3}^{(0)}\rangle$; sending this latter photon through a SPP with an aligned step and $\ell = -\frac{2}{3}$, combined with a single-mode fibre, then yields a detection probability of unity.

7.5 Orientation of the edge dislocation

Since we intend to rotate the non-integer SPPs, it is important to also have a description of the states that arise when the SPP is rotated while the coordinate system is fixed. To gain insight, we show in Fig. 7.3 the phase shift imposed by a SPP as a function of the azimuthal angle. The solid line represents the imprinted phase for a SPP with its edge oriented at an angle $\theta = 0$, while the dashed line corresponds to a SPP with edge orientation $\theta = \alpha$. We can now generalise the definition of the operator $\hat{S}(\ell)$ to the operator $\hat{S}(\alpha, \ell)$, which includes

the orientation α of the edge dislocation. We find

$$\langle \hat{r} | \hat{S}(\alpha, \ell) | l \rangle = \frac{1}{\sqrt{2\pi}} \exp\left[i(l + \ell)\theta\right] \begin{cases} \exp\left[i(2\pi - \alpha)\ell\right], & 0 \leq \theta < \alpha, \\ \exp\left(-i\alpha\ell\right), & \alpha \leq \theta < 2\pi, \end{cases} \tag{7.6}$$

where $\alpha, \theta \in [0, 2\pi)$. This also allows us to generalise the states $|a_\lambda^{(l)}\rangle$ with orientation $\theta = 0$ to states with arbitrary orientation, $|a_\lambda^{(l)}(\alpha)\rangle$. From Eq. (7.6), it is immediately clear that the complementary SPP operator $\hat{S}^{\mathrm{compl}}(\alpha, \ell)$ is equal to $\hat{S}(\alpha, -\ell) = \hat{S}^\dagger(\alpha, \ell)$.

Since the basis $\left\{ |a_\lambda^{(l)}(0)\rangle \right\}$ is complete, the states after rotation, $|a_\lambda^{(l)}(\alpha)\rangle$ can be written as a superposition of these basis states. Thus the decomposition of $|a_\lambda^{(l)}(\alpha)\rangle$ into the basis $\left\{ |a_\lambda^{(l)}(0)\rangle \right\}$ depends on the angle α. To illustrate this, we make a projection of a non-integer state oriented at $\theta = \alpha$, onto the same state with orientation $\theta = 0$. For this, we choose a SPP with step $\ell = j + \lambda$, where j is the integer part of the step (not to be confused with the integer LG index l), and $\lambda \in [0, 1)$, yielding the overlap amplitude

$$\begin{aligned} A_\lambda(\alpha) &= \langle a_\lambda^{(l+j)}(0) | a_\lambda^{(l+j)}(\alpha) \rangle \\ &= \langle l | \hat{S}^\dagger(0, j + \lambda) \hat{S}(\alpha, j + \lambda) | l \rangle \\ &= \frac{1}{2\pi} \left[2\pi - \alpha + \alpha \exp\left(i 2\pi\lambda\right) \right] \exp\left[-i(l + j + \lambda)\alpha \right], \end{aligned} \tag{7.7}$$

where $|l\rangle$ is the OAM operator eigenstate with eigenvalue l. The overlap probability is then

$$|A_\lambda(\alpha)|^2 = \left(1 - \frac{\alpha}{\pi} \right)^2 \sin^2(\lambda\pi) + \cos^2(\lambda\pi), \tag{7.8}$$

which depends neither on the integer part of the step index j nor on the OAM state l. For non-zero values of λ, this overlap function has a quadratic dependence on the orientation α. This function is plotted in Fig. 7.4 for various values of λ. It illustrates that, when $\lambda = 0$, the projection does not change, as expected. For values of $\lambda \neq 0$, the outcome of the projection is less trivial, with $\lambda = \frac{1}{2}$ providing an especially interesting case: when the state is rotated over $\alpha = \pi$ by rotating the SPP, the state is orthogonal to the non-rotated state. We will call the half-integer-OAM states $|a_{\frac{1}{2}}^{(l)}(0)\rangle$ and $|a_{\frac{1}{2}}^{(l)}(\pi)\rangle$ 'up' and 'down', respectively, referring to the orientation of the edge part of the dislocation. In principle, this orientational label can be used for *any* non-integer-OAM state, but for half-integer-OAM states it carries an analogy to fermionic spin, as our 'up' and 'down' states are orthogonal just like up and down spin $\frac{1}{2}$. In polarisation entanglement the comparable orientational labels are known as 'H' for horizontal and 'V' for vertical polarisation. To make our proposed OAM-entanglement setup maximally equivalent to the polariser setup, we focus from now on mainly on the case $\lambda = \frac{1}{2}$. Note that, as Eq. (7.8) is independent of j, any SPP with $\ell = j + \lambda$ may be used, as long as $\lambda = \frac{1}{2}$.

There is, however, a key difference between the half-integer-OAM states on the one hand and the fermionic-spin states or polarisation states on the other hand. Angularly intermediate states of the fermionic spin or of polarisation are a superposition of the two orthogonal basis states 'up' and 'down', or 'H' and 'V', so that the overlap function varies as $\sin^2 \alpha$. However,
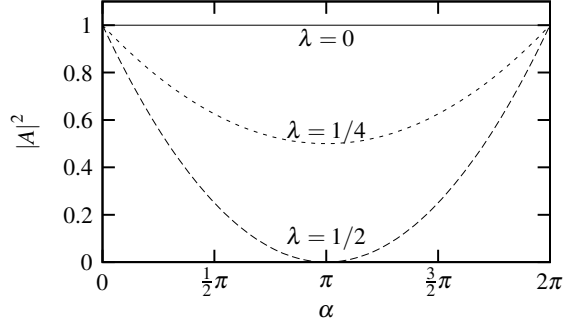
Figure 7.4: *The overlap (see Eq. (7.8)) between a non-integer-OAM state and the identical state rotated over α. When $\lambda = 0$, the states are identical aside from a trivial phase shift, due to the vanishing edge dislocation. For half-integer OAM, i.e. $\lambda = \frac{1}{2}$, the two states are generally different, leading to a parabolic dependence of their overlap; the two states are orthogonal when $\alpha = \pi$.*

from Eq. (7.8) we see that in the present case, the dependence of $|A|^2$ on α yields a *parabola*. Thus we conclude that, as the SPP is rotated from 'up' to 'down', the OAM state follows a path through Hilbert space that is *not* confined to the two-dimensional subspace spanned by the 'up' and 'down' states. Note that the OAM expectation value will be conserved along this path, as rotating the SPP has, of course, no effect on its step height, i.e. on ℓ.

7.6 Entanglement of half-integer-OAM states

When dealing with the entanglement of OAM states, issues of conservation of OAM during the spontaneous-parametric-down-conversion process arise. This conservation is discussed in many papers [17, 54, 57, 58, 70, 78, 79] and it seems that OAM is indeed conserved if two conditions are fulfilled, namely that the process occurs in *(i)* the paraxial limit, and *(ii)* the thin-crystal limit. In practice this is usually the case and we will therefore work within these limits.

The two-photon state can be described in the spatial polar representation as [80]

$$|\Psi\rangle = \int_0^{2\pi} \int_0^\infty r \, \mathscr{P}(r, \theta) \, |r, \theta\rangle_1 \, |r, \theta\rangle_2 \, \mathrm{d}r \, \mathrm{d}\theta, \tag{7.9}$$

where $\mathscr{P}(r, \theta)$ is the mode function of the pump beam. The photons are thus emitted from the same location at the exit plane of the nonlinear crystal. We restrict ourselves to a pump beam in a pure OAM mode so that $\mathscr{P}(r, \theta)$ can be written as $\mathscr{R}(r) \exp{(iq\theta)} / \sqrt{2\pi}$, where $\mathscr{R}(r)$ is the radial part of the pump mode function. We can now write the two-photon state in

the half-integer SPP basis $\left\{ |a^{(n)}_{\frac{1}{2}}(0)\rangle \right\}$, thus yielding

$$
\begin{aligned}
|\Psi\rangle =& \frac{1}{\sqrt{2\pi}} \int_0^\infty r\mathscr{R}(r) |r\rangle_1 |r\rangle_2 \, \mathrm{d}r \\
& \times \sum_{m,n=-\infty}^{\infty} \left[\int_0^{2\pi} \exp(iq\theta) \langle a^{(n)}_{\frac{1}{2}}(0)|\hat{r}\rangle \langle a^{(m)}_{\frac{1}{2}}(0)|\hat{r}\rangle \, \mathrm{d}\theta \right] \\
& \times |a^{(n)}_{\frac{1}{2}}(0)\rangle |a^{(m)}_{\frac{1}{2}}(0)\rangle \\
=& \frac{1}{\sqrt{2\pi}} |R\rangle \sum_{n=-\infty}^{\infty} |a^{(n)}_{\frac{1}{2}}(0)\rangle |a^{(q-n-1)}_{\frac{1}{2}}(0)\rangle,
\end{aligned}
\tag{7.10}
$$

where we have defined the radial ket,

$$
|R\rangle \equiv \int_0^\infty r\mathscr{R}(r) |r\rangle_1 |r\rangle_2 \, \mathrm{d}r.
\tag{7.11}
$$

We now continue to calculate the coincidence fringe that is expected in the proposed experiment. For the pump beam, we shall assume a fundamental Gaussian beam, so that $q = 0$ in Eq. (7.10). In the signal path we place an analyser consisting of a SPP with $\ell = j + \frac{1}{2}$ where j is an integer, with its orientation set to 'up' ($\theta = 0$), represented by $\hat{S}(0, j + \frac{1}{2})$, and a single-mode fibre. When the detector clicks, the signal state *before* passing through this analyser is collapsed to $\hat{S}^\dagger(0, j + \frac{1}{2})|0,0\rangle = |\rho_{00}\rangle |a^{(-j-1)}_{\frac{1}{2}}(0)\rangle$, where $|\rho_{00}\rangle$ is the radial part of the fundamental-Gaussian state.

Consequently, according to Eq. (7.10) with $l = 0$, the angular part of the idler state $|\psi\rangle_2$ is then collapsed to

$$
|\psi\rangle_2 = C|a^{(j)}_{\frac{1}{2}}(0)\rangle,
\tag{7.12}
$$

where

$$
C = \frac{1}{\sqrt{2\pi}} \left(\langle \rho_{00}|_1 \langle \rho_{00}|_2 \right) |R\rangle.
\tag{7.13}
$$

Thus when analysing the idler state with $\hat{S}(\alpha, j + \frac{1}{2})|0,0\rangle$ we obtain the projection

$$
B(\alpha) = C\langle a^{(j)}_{\frac{1}{2}}(\alpha)|a^{(j)}_{\frac{1}{2}}(0)\rangle.
\tag{7.14}
$$

Note that Eq. (7.14) has, aside from a pre-factor, exactly the same appearance as Eq. (7.7) with $\lambda = \frac{1}{2}$. The coincidence fringe is then given by the modulus squared,

$$
|B(\alpha)|^2 = |C|^2 \left(1 - \frac{\alpha}{\pi} \right)^2,
\tag{7.15}
$$

which is proportional to Eq. (7.8): we find a parabolic coincidence fringe.

The above reasoning to obtain the coincidence fringe $|B(\alpha)|^2$ is valid for any choice of the signal SPP orientation and only depends on the *relative* orientation α of the signal and idler SPPs. Thus a coincidence measurement on entangled OAM pairs using half-integer OAM analysers, will bring forth a coincidence fringe that is parabolic, regardless of the *individual* settings of the analysers.

7.7 The CHSH version of the Bell inequality

There have been several theoretical papers that address the generalisation of the Bell inequality [7] to quantify the violation of local realism of two N-dimensional particles (qu$N$its) [9, 10, 81–84]; an example of a qu$N$it is a spin-s particle with $2s + 1 = N$. It has been pointed out that in this case the use of m_s-sorting devices, such as Stern-Gerlach analysers, does *not* offer access to higher-dimensional quantum correlations, presumably because the action of a Stern-Gerlach analyser depends only on the alignment of its quantisation axis [9]. Instead of larger spin values ($s > \frac{1}{2}$), the use of spatial degrees of freedom together with Bell multiports has been advocated to gain access to the multi-dimensional aspects of entanglement [9]. We stress that all this is different from our proposed use of half-integer SPPs ($s + \frac{1}{2}$). These devices do *not* produce finite-N qu$N$its, but imprint the infinite OAM dimensionality of the (oriented) edge on a transmitted light field. Rotation of this edge is equivalent to a partial exploration of the complete Hilbert space along a certain path, namely an iso-OAM path; due to this complexity, it is not clear how a generalised Bell inequality could be applied to our case.

However, instead of using a generalised high-dimensional bipartite Bell inequality, it is allowed to use an inequality for lower-dimensional two-particle entanglement [84]. Thus we choose, as in the polarisation case, the inequality introduced by Clauser, Horne, Shimony and Holt (CHSH) for a measurement where the coincidence probability is expected to be a function of only $\alpha_s - \alpha_i$ [85]. When relabelling α_s and α_i as α_1 and α_2 (in no particular order), the CHSH inequality is given by [77, 86]

$$
\begin{aligned}
S =& E(\alpha_1, \alpha_2) - E(\alpha_1', \alpha_2) + E(\alpha_1, \alpha_2') \\
& + E(\alpha_1', \alpha_2') \leq 2.
\end{aligned}
\tag{7.16}
$$

The function E is specified, for the variables x, y, as [77, 87]

$$
E(x, y) = \frac{P(x, y) + P(x^\perp, y^\perp) - P(x, y^\perp) - P(x^\perp, y)}{P(x, y) + P(x^\perp, y^\perp) + P(x, y^\perp) + P(x^\perp, y)}.
\tag{7.17}
$$

The notation $x^\perp$ (and similarly for $y^\perp$) is used to indicate an analyser setting that analyses a state orthogonal to the state with setting x. Thus in our case, $x^\perp \equiv x + \pi$ and $y^\perp \equiv y + \pi$. $P(x, y)$ is the coincidence-probability function, which is equal to

$$
P(x, y) = |B(|y - x|)|^2 = C^2 \left(1 - \frac{|y - x|}{\pi}\right)^2.
\tag{7.18}
$$

As the periodicity in the present case is half that of the case of polarisation entanglement, we use the standard analyser settings for polarisation entanglement [77, 88] multiplied by a factor of two: $\alpha_1 = -\frac{1}{4}\pi$, $\alpha_1' = \frac{1}{4}\pi$, $\alpha_2 = -\frac{1}{2}\pi$, $\alpha_2' = 0$.

Substitution yields a CHSH-Bell parameter $S = 3\frac{1}{5}$. This is the key result of this Chapter; it indicates that in the case of entanglement of half-integer-OAM states, the maximum violation of the CHSH inequality, given by Eq. (7.16), is *stronger* than the maximum violation that is allowed in polarisation entanglement, namely $S = 2\sqrt{2}$. In other words, quantum non-locality of the photons in the proposed setup is stronger than the maximum achievable for two

qubits. To achieve this, only *two* detectors are required and only *one* coincidence-count rate is measured per analyser setting, in contrast to the OAM qu$N$it setup requiring N detectors and N^2 coincidence-count rates per analyser setting [9, 10].

7.8 Conclusions

In this Chapter we have put forward a novel approach to demonstrate high-dimensional entanglement of orbital-angular-momentum states. The proposed setup uses analysers that consist of non-integer SPPs and single-mode fibres, enabling detection of high-dimensional entanglement with only two detectors.

The key idea is to use the orientation of the edge dislocation in the SPPs. We specialise in the case of half-integer ℓ, so that the orientation of the edge as an analyser setting can, to a certain extent, be treated similarly as the axis of a polariser in polarisation entanglement. Instead of states with horizontal and vertical polarisation, we deal with 'up' and 'down' states, referring to the orientation of the edge dislocation. We analytically calculate the coincidence fringe in the entanglement setup and find it to be parabolic in shape, and periodic over 2π. When evaluating the well-known CHSH version of the Bell parameter, we find $S = 3\frac{1}{5}$, i.e. we predict beyond-Bell pairing of two photons. To observe this, we require only *two* detectors, as opposed to the standard multi-port approach [9, 10]. This economic exploitation of the spatial degrees of freedom seems to be a consequence of the singular nature of our half-integer SPPs, which implies, in principle, infinite dimensionality.

Acknowledgements

Appendix

7.A   Pure edge dislocation

In the present Chapter, we have seen that, for spiral phase plates with half-integer step index ℓ, i.e. imprinting a mixed screw-edge dislocation, the coincidence fringe in a twin-photon experiment is parabolic as a function of the relative orientation of the two radial edges, with visibility equal to 1. This then results in a value of the CHSH-Bell parameter equal to $S = 3\frac{1}{5}$.

An intriguing question we asked ourselves, after having performed the experiment described in Chapter 8, is whether there are other devices with optical singularities, besides the half-integer spiral phase plate, that, in a quantum experiment, will give rise to a similarly large value of the CHSH-Bell parameter. More to the point, can one design a twin-photon experiment that results in a value of the CHSH-Bell parameter larger than $2\sqrt{2}$, using devices that are simpler to produce and handle than the spiral phase plate discussed so far?

As we will see below, this question can be answered in a positive way, and the proposed device is surprisingly simple. It is a non-integer step phase plate carrying a straight edge dislocation, as shown in Fig. 7.5. Obviously, such a plate can be manufactured more easily
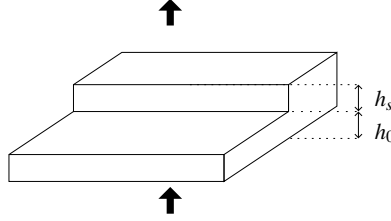

Figure 7.5: *Similar to the spiral phase plate in Fig. 7.1a), the non-integer step phase plate has its step height h_s chosen so that the phase shift due to the thick part is a non-integer multiple of 2π with respect to the thin part. The edge dislocation is chosen so that it goes through the centre of the field mode.*

than the spiral phase plates, whose production and characterisation is extensively discussed in Chapters 5 and 6.

Similar to the non-integer spiral phase plate, the non-integer step phase plate also transforms a pure orbital-angular-momentum state into a high-dimensional state, and contains an orientational degree of freedom, α, since it carries an analogous edge dislocation. We can therefore use a similar treatment to write a unitary operator for the plate's action,

$$\langle x, y | \hat{F}(\alpha, \phi) | l \rangle = \frac{\exp(il\theta)}{\sqrt{2\pi}} \times \begin{cases} \exp(i\phi), & \alpha \leq \theta < \alpha + \pi, \\ 1, \end{cases} \tag{7.19}$$

where $\alpha \in [0, \pi)$ represents the orientation of the step, ϕ the optical phase delay resulting from the step, $\theta \in [0, 2\pi)$ the azimuthal angle and $|l\rangle$ the orbital-angular-momentum eigenstates. For the special case $\phi = \pi$, Eq. (7.19) corresponds to the Hilbert transform [89, 90]. The definition of the unitary operator $\hat{F}$ as given in Eq. (7.19) can be extended for
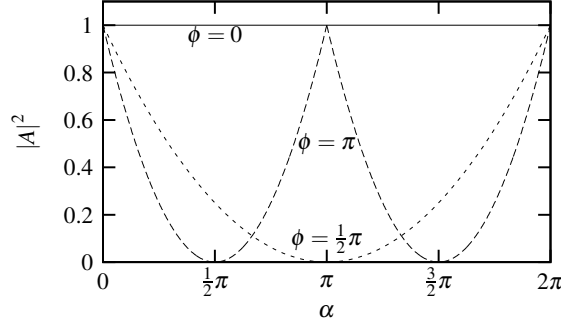
Figure 7.6: *The overlap (see Eq. (7.21)) between a state with an imprinted line dislocation, and the identical state rotated over α. When there is no dislocation ($\phi = 0$), the states are identical. For other phase differences ϕ, the two states are generally different; $\phi = \frac{1}{2}\pi$ and $\phi = \pi$ result in a continuous parabolic fringe.*

$\alpha \in [-\pi, \pi)$, seemingly complicating matters, but without any impact on the calculations ahead.

Since the operator $\hat{F}$ is unitary, we can define a new, complete basis $\left\{ |b_\phi^{(l)}(\alpha)\rangle \right\}$, where $\hat{F}(\alpha, \phi)|l\rangle = |b_\phi^{(l)}(\alpha)\rangle$. We can write the states after rotation $|b_\phi^{(l)}(\alpha)\rangle$ in terms of superpositions of the non-rotated states $|b_\phi^{(l)}(0)\rangle$, where the decomposition depends on the angle α. We can illustrate this by making a projection of such a state with $\alpha = 0$ onto the same state with $\alpha \neq 0$. The overlap amplitude thus becomes

$$
\begin{aligned}
A(\alpha) &= \langle b_\phi^{(l)}(0)|b_\phi^{(l)}(\alpha)\rangle \\
&= \frac{\alpha}{\pi}(\cos\phi - 1) + 1,
\end{aligned}
\tag{7.20}
$$

which is valid for values of $\alpha \in [-\pi, \pi)$. The overlap probability thus becomes

$$
|A(\alpha)|^2 = \left(\frac{\alpha}{\pi}\right)^2 (\cos\phi - 1)^2 + 2\frac{\alpha}{\pi}(\cos\phi - 1) + 1.
\tag{7.21}
$$

Figure Fig. 7.6 shows the intensity fringe as a function of α for three different values of ϕ. For clarity, we show the functions over the range $\alpha \in [0, 2\pi)$ instead of $\alpha \in [-\pi, \pi)$, which is allowed since α is periodic over 2π. The most interesting cases occur when $\phi = \pi$ and $\phi = \pi/2$, since the fringe becomes a parabola, periodic over π and 2π, respectively. The result is then, aside from the periodicity, identical to that for a half-integer spiral phase plate. Currently, we are involved in a further study of the intensity fringe for arbitrary values of ϕ.

A plate with an edge dislocation with phase difference π or $\pi/2$ can thus be used, similar to a spiral phase plate, to investigate entanglement. The setup would be identical to Fig. 7.2 with the spiral phase plates replaced by the edge dislocation devices discussed here. The calculation from two-photon state to coincidence fringe is the same as discussed in Section 7.6, using the states $|b_\pi^{(l)}(\alpha)\rangle$, or $|b_{\pi/2}^{(l)}(\alpha)\rangle$ instead of $|a_{1/2}^{(l)}(\alpha)\rangle$.

The CHSH-Bell inequality is violated maximally for these two-photon states, using the set of sixteen angles as used in polarisation entanglement for $\phi = \pi$, and the set as used for

the half-integer spiral phase plates for $\phi = \pi/2$. Both cases yield an CHSH-Bell parameter equal to $S = 3\frac{1}{5}$.

We note that, although this device is much easier to manufacture than the spiral phase plate, it would be only marginally more convenient to use in an experimental setup. It is true that whereas the spiral phase plate has a central *point* which has to be aligned with respect to the beam line and the other spiral phase plate's central point, this plate only has a central *line*. However, this eliminates only one degree of freedom (out of the twelve, see Fig. 8.8) from the tedious alignment procedure described in Chapter 8. Although many of the same problems would thus still occur in a setup where these step phase plates are used, it remains interesting to demonstrate high-dimensional entanglement by using such a simple device. The experimental implementation of this proposal, however, is outside the scope of this thesis, as is a comprehensive study to answer the question what the most general 'singular' device is, that produces $S = 3\frac{1}{5}$ (assuming that this is a universal result).

CHAPTER 8

A two-detector measurement of beyond-Bell photon pairing

In Chapter 7, we have shown theoretically that the use of spiral phase plates in state analysers may reveal an entanglement that is stronger than that of the polarisation Bell states. In this Chapter, we will discuss its experimental implementation. First, the Klyshko advanced-wave model is simulated in a classical experiment to obtain an idea of the difficulties involved in the quantum experiment. Then the actual quantum experiment is discussed, important issues regarding alignment and accuracy are highlighted and results are presented that confirm the theoretical predictions.

8.1 Introduction

The spiral phase plate (SPP) is a convenient device to generate orbital angular momentum in an optical beam. The physics becomes particularly interesting when the step height of the SPP is such that it imparts a non-trivial phase discontinuity on the beam. The orbital angular momentum per photon in units of $\hbar$ is then non-integer and the generated mode is a high-dimensional superposition of orbital-angular-momentum modes [5].

In Chapter 7, a scheme has been proposed to exploit the high-dimensional character of these modes for entanglement purposes. The idea is to use a setup that is similar to that of polarisation entanglement, with the polarisers replaced by *half-integer* SPPs combined with single-mode fibres (cf. Fig. 7.2). To measure a coincidence fringe, one of the SPPs is rotated around its centre; here the orientation of its step acts as an analyser setting. The resulting coincidence fringe is predicted to be parabolic as a function of the relative setting of the signal and idler analysers. The most exciting feature of this proposal is that *high-dimensional* entanglement can be explored with only *two* detectors. It is predicted to yield a violation of the Clauser-Horne-Shimony-Holt (CHSH) version of the Bell inequality that is *larger* than that for the well-known twin-photon Bell states [85], thus showing stronger non-local behaviour. Photons that show this strong violation of the Bell inequality are thus entangled 'beyond Bell'.

In the present Chapter, we implement the proposed scheme to observe this beyond-Bell entanglement. To this end, we first test an analyser consisting of a SPP and single-mode fibre in a classical setup. We then discuss the entanglement setup and finally report the results.

8.2 Testing the analyser

In the quantum experiment as proposed in Chapter 7, the non-local quantum correlations are explored by measuring the coincidence fringe in a spontaneous-parametric-down-conversion setup that incorporates a SPP in the signal beam and a complementary SPP in the idler arm. In such a setup, entanglement is conveniently described by the 'advanced-wave' model introduced by Klyshko *et al.* as a model for two-photon optics [91]. Based on a Green's function approach in which the nonlinear crystal, when pumped by a laser beam, can be treated as a 'geometrical-optics reflection' mirror for the advanced wave, this model allows for replacement of the quantum setup (cf. Fig. 7.2) by a classical setup where a beam propagates from the signal detector towards the idler detector via the nonlinear crystal. This setup can be unfolded, by properly taking the 'reflective' properties of the crystal and pump into account. In this advanced-wave model, the two-photon coincidence fringe, i.e. the fourth-order-field-correlation function, has exactly the same shape as the second-order-field-correlation function of a classical optical beam that follows the path of the advanced wave. The two-photon coincidence fringe can thus be mimicked in a classical setup; the latter is ideally suited to test the use of SPPs in the quantum setup.

Applying this advanced-wave model to the twin-photon setup shown in Fig. 7.2, we first build the classical equivalent, shown in Fig. 8.1. We inject a laser beam into a single-mode fibre, thereby creating a fundamental Gaussian beam. The latter is made to propagate as a collimated beam through a half-integer SPP with step index ℓ. We analyse the field created in
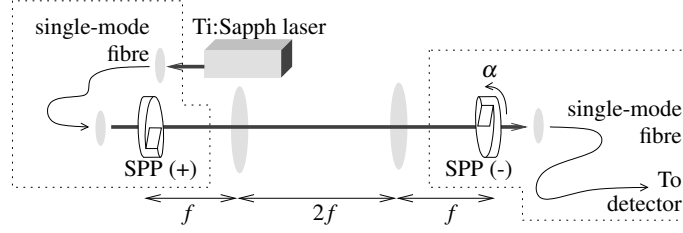
Figure 8.1: *The classical setup used to test the analyser. The optical elements in the dotted box on the left prepare the laser beam in a SPP mode. The dotted box on the right contains the SPP mode analyser. The lens system images the first SPP onto the second SPP. The relative orientation of the step edges of the SPPs can be varied.*

this way using a second SPP, which is the complement of the first SPP, oriented at angle α, in combination with a single-mode fibre. In the Klyshko model, this analyser is the classical equivalent to the analysing elements in the idler path of the two-photon setup. The output of the fibre is measured as a function of the orientation angle α of the second SPP. Ideally, this experiment yields a fringe, given (when properly normalised) by

$$|A(\alpha)|^2 = \left(1 - \frac{\alpha}{\pi}\right)^2 \sin^2\left(\ell\pi\right) + \cos^2\left(\ell\pi\right), \tag{8.1}$$

as derived in Eqs. (7.7) and (7.8). For any non-integer ℓ, this represents a parabolic function of α with a minimum at $\alpha = \pi$. The visibility of the fringe, defined as if the fringe were sinusoidal[1], is maximal (unity) when ℓ is half-integer. Calculation of the CHSH version of the Bell parameter (cf. Eq. (7.16)) as a function of ℓ (see Fig. 8.2) shows that for integer values of ℓ, the CHSH-Bell parameter equals zero, while half-integer values of ℓ yield the maximum value of the CHSH-Bell parameter, i.e. $S = 3\frac{1}{5}$; this is the reason for designing the SPPs to have half-integer ℓ values.

Our test of the analyser then consists of performing the experiment just described and comparing the measured fringe with the prediction of Eq. (8.1), and using the SPPs inves-
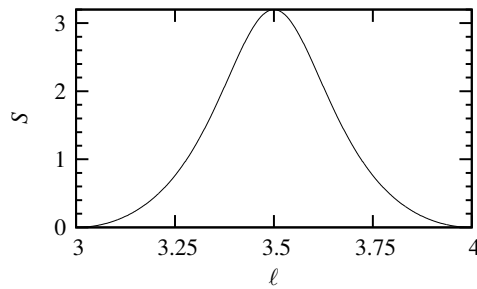
Figure 8.2: *Graph indicating the dependence of the CHSH-Bell parameter S on ℓ. S is maximised to a value of 3.2 when ℓ is half-integer.*

---

[1]The standard definition for the visibility of any two-mode interference pattern is $V = (I_{\max} - I_{\min})/(I_{\max} + I_{\min})$, where $I_{\max}$ and $I_{\min}$ are the maximum and minimum intensities, respectively. Here, we use coincidence counts per second instead of the intensity.
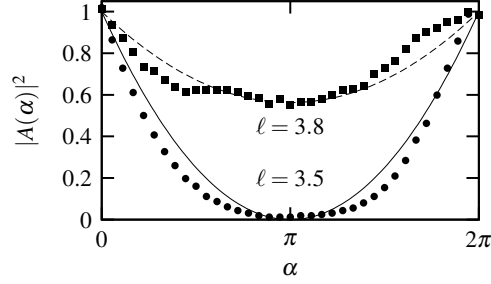
Figure 8.3: *Results obtained for the setup shown in Fig. 8.1 using the SPPs discussed in Chapter 6. When $\ell = 3.5$, a parabola with 100% visibility is expected (solid curve). The data (circles) show good agreement with the theory and have a 97.6% visibility. The experiment is repeated for a different wavelength, where $\ell = 3.8$. The experiment (squares) reveals that the visibility is reduced, in accord with theory (dashed curve).*

tigated in Chapter 6. The dotted box to the left shows how the input field is prepared, as described above, using a single-frequency titanium-sapphire laser. A $4f$ telescope images the plane of the first SPP onto the second SPP which has the opposite step index (ℓ-value) and is part of the analyser that we wish to test. When the latter SPP is aligned with the first SPP ($\alpha = 0$, taking the inverting telescope into account), the far field has a nice Gaussian profile, as has been shown in Fig. 6.3.

The analyser consists of this second SPP and a single-mode fibre, as shown in the dotted box on the right in Fig. 8.1. The output of the fibre is normalised to that obtained when both SPPs are removed. When the edge dislocations of the two SPPs are well aligned, the normalised output is found to be 98% (see Chapters 5 and 6). When we now rotate the analyser SPP relative to the first SPP, we obtain the results shown in Fig. 8.3. The circles give the data for $\lambda_1 = 813$ nm where $\ell = 3.5$, while the squares show the results for $\lambda_2 = 738$ nm ($\ell = 3.8$). The solid and dashed curves give the predictions of Eq. (8.1) for $\ell = 3.5$ and $\ell = 3.8$, respectively. We find that the experiment agrees well with the predicted parabolic dependence. Note that the data for $\ell = 3.8$ contains additional features. We attribute those to the fact that, for the $\ell = 3.8$ case, we are more sensitive to minute misalignments in the setup than for the $\ell = 3.5$ case. The experiment for $\ell = 3.8$ forms an important part of our test of the analyser. By observing a parabolic fringe with reduced visibility, in agreement with theory, we ensure that our result at $\ell = 3.5$ is not caused by walk-off effects during rotation of the second SPP.

This test indicates that with our SPPs, the scheme for observing beyond-Bell pairing of photons is feasible. Note, however, that in this classical experiment, only *one* SPP is required to rotate, namely the SPP that is incorporated in the analyser. In the quantum experiment, *both* SPPs are required to rotate in order to measure an CHSH-Bell parameter. As we will see, this additional requirement causes severe complications.

8.3 The quantum experiment

The quantum experiment makes use of a setup that has been built by Dirk Voigt for polarisation entanglement. For the purpose of the present experiment, the SPPs are inserted into the signal and idler paths and, during the actual measurements, the polariser orientations are fixed along the β-barium borate (BBO) crystalline axes.
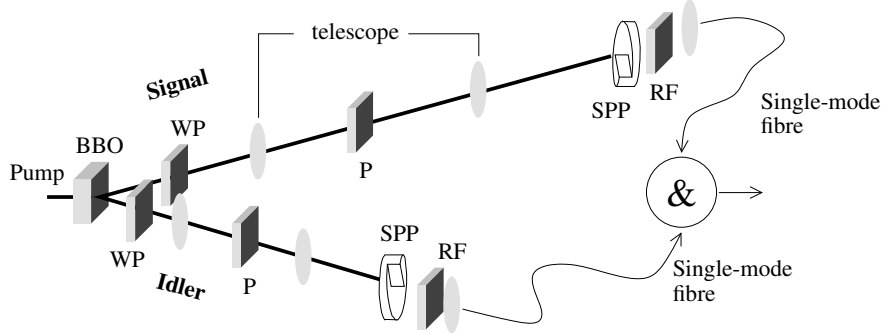

Figure 8.4: *The quantum setup. In each path one encounters a wave plate (*WP*) for walk-off compensation, a telescope that images the near field of the nonlinear crystal onto the SPP, a polariser (*P*) and a red filter (*RF*) to eliminate stray pump light. The down-converted light is focused with a microscope objective onto a single-mode fibre and coincidence counts are measured.*

The experimental setup is shown in Fig. 8.4. The pump laser is a krypton-ion laser tuned to a wavelength of 406.7 nm, delivering a power of 54 mW. The pump beam is weakly focused on the nonlinear crystal (BBO), with a full width at half maximum of 1.0 mm. The crystal is 1.0 mm thick and is cut for type-II collinear spontaneous parametric down-conversion. It is tilted so that the opening angle between the paths of entangled photons is $6°$. In each path, a 0.5 mm-thick wave plate (BBO) is positioned, for walk-off compensation.

To make the setup identical to the one discussed in Chapter 7 (cf. Fig. 7.2), we wish to position the previously discussed analysers in the near field of the crystal. By inserting a properly focused $2\times$-magnifying telescope into each path, as shown in Fig. 8.4, the crystal plane is imaged onto the plane where the SPPs will be positioned. Note that there is no constraint on the diameter of the pump spot at the crystal as is usual in the ghost-imaging experiments [92], due to the near-field imaging. The only requirement is that the crystal generates enough transverse momentum spread to contain these high-dimensional OAM states with some probability.

We do not use interference filters to select the down-converted light at the degenerate frequency because we have experienced that these modify the beam profile in an uncontrolled way. In the present experiment this is more troublesome than usual, because of the large momentum spread of the half-integer fields, illustrated in Fig. 8.5. Instead, we use red-transmitting colour-filters (transmission for $\lambda > 715$ nm) and estimate that, in combination with the spectral filtering implied by the numerical aperture of each path, the down-converted light is filtered to a bandwidth less than 10 nm, centred at the degenerate wavelength ($\lambda = 813$ nm).
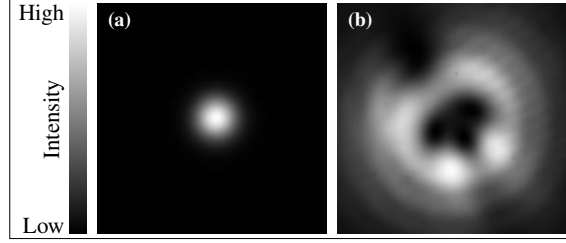
Figure 8.5: *Far-field intensity profiles illustrating the difference in momentum spread of different modes. (a) The narrow far-field distribution of a fundamental Gaussian beam (ℓ =0) shows its small momentum spread. (b) The far field of an ℓ =3.5 mode has a significantly larger profile, indicating that the beam contains a large momentum spread. Both images are obtained from the experiment with identical scaling.*

Each analyser unit consist of a microscope objective (NA= 0.25, 40× magnification factor), a single-mode fibre (NA= 0.12, 5 µm core diameter), and a SPP. As each analyser unit possesses 12 knobs, we need to adjust 24 knobs, which are not independent, to properly align the setup. Therefore, we only provide an outline of the alignment procedure here, while a detailed description can be found in the appendix.

In the first stage of the alignment procedure (for details, see Section 8.A.2), the SPPs are absent and a diode laser beam is injected in the fibres from the back side. The focus of the microscope objective in each analyser unit is adjusted so that the laser beam has a waist at the (future) position of the SPP and thus, because of the imaging system, also at the crystal plane. We then disconnect the diode laser and replace it by a single-photon-counting module (Perkin-Elmer SPCM-AQR-16) for each fibre, whereupon we commence the second stage of the alignment procedure (for details, see Section 8.A.2); both the transverse position of the detection units (without SPP) as that of the fibre-tips are scanned to optimise for coincidence counts and after that, for polarisation entanglement. With a coincidence window of 2 ns, we obtain a coincidence-count rate of the order of 30 counts per second and a polarisation entanglement visibility of 95% and 92% in the crystal (H,V) and 45° basis, respectively. This high degree of polarisation entanglement shows that the use of RG filters for wavelength selection is affordable. The orientations of the polarisers are then fixed in the crystal basis and are not changed any more.

In the third stage of the alignment procedure (for details, see Section 8.A.3), we introduce the SPPs in the signal and idler paths. To facilitate this, we first reconnect the auxiliary diode laser to the detector side of each fibre and, using a CCD camera and imaging optics, mark the transverse position of the laser beam (without SPP) in the near and far fields of the SPP, so that the detection mode is accurately defined. The SPP is then put into place while observing both the SPP and laser beam in the near field. As the transverse position of the SPP in the laser beam is difficult to gauge in the near field, we align on the symmetry of the far-field profile of the SPP mode (see Fig. 8.9), which, as it turns out, is quite sensitive to the alignment. This procedure is followed for each of the two detection units separately. After this, the transverse position of one SPP is fine-tuned by observing the coincidence-count rate, which is about 13 events per second when both analysers are set to the same orientation.
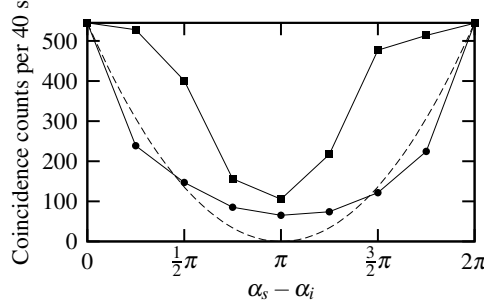
Figure 8.6: *While a measurement for the first setting of the idler SPP resembles a parabola with low visibility (circles, solid lines), the measurements for the other three settings of the idler SPP do not; the latter lead typically to heavily deformed parabolas, one of which is also shown here (squares, solid lines), together with the expected theoretical result (dashed curve). The value for the CHSH-Bell parameter S in this case was found to be less than 2.*

The setup is now ready. To obtain a value of the Bell parameter, as described in Chapter 7, the idler SPP needs to be set in four different orientations, for each of which four settings of the signal SPP are required. For all sixteen combinations, the coincidence counts have to be measured and from Eq. (7.16) the Bell parameter can be calculated. After having aligned the setup with the procedure described above, it is straightforward to measure a coincidence fringe with a parabolic appearance for one of the four settings of the idler SPP, although the visibility is only 79%. This can be seen in Fig. 8.6, where we have plotted the coincidence-count rate for eight settings of the signal SPP, to enable a better comparison with the theoretical fringe. For the other three settings of the idler SPP, however, the coincidence fringe is far from parabolic, as illustrated by the failed measurement in Fig. 8.6. Such measurements yield an CHSH-Bell parameter S ranging from 0.8 to 1.8, suggesting a behaviour that can be explained by a local theory. The reason for the failure of this experiment is that the alignment has to be performed with even more care.

After many, fruitless time-consuming attempts to further adjust the setup to yield an CHSH-Bell parameter S larger than 2, we were forced to conclude that the positioning of the SPPs is so critical that the method outlined here has insufficient sensitivity. When analysing the experimental problems, it became clear that, apart from issues relating to the pointing stability of the pump beam as disclosed by the BeamLok indicator, the most important remaining difficulties arise from the fact that the setup is bipartite. Whereas in the classical test described in Section 8.2, the two SPP's can be easily aligned with respect to the *single* beam line and the analyser fibre, as well as with respect to each other, this can not be done in the quantum experiment, since it has *two* beam lines, which is of course essential for testing non-locality. Here, we can align the two beam lines with respect to each other by maximising the coincidence counts. However, each SPP can only be aligned relative to its own beam line, and *not* with respect to the other SPP, notwithstanding the fact that this relative alignment is of extreme importance, as we have learned from the classical test. The protocol for the alignment of each SPP with respect to its own beam line in combination with the protocol for aligning the two beam lines with respect to each other gives only indirect information on the
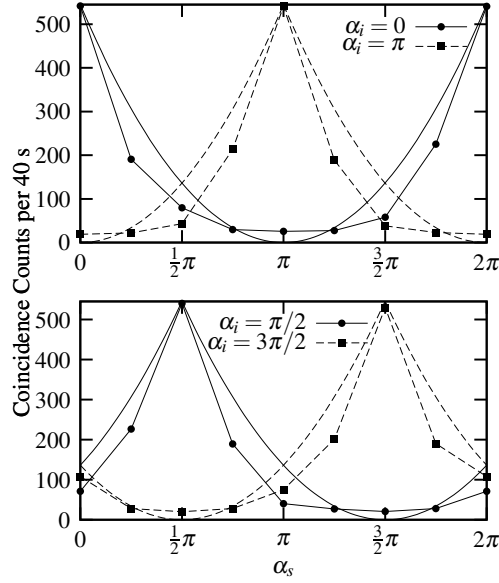
Figure 8.7: *The set of fringes as a function of the signal-SPP orientation α_s, that yield $S = 3.0 \pm 0.1$. The top graph shows the fringes with the idler-SPP orientation $\alpha_i = 0$ (circles, solid lines) and the expected parabola (solid curve), and $\alpha_i = \pi$ (squares, dashed lines) and the expected half parabolas (dashed curve). The bottom graph shows the fringes for $\alpha_i = \frac{\pi}{2}$ (circles, solid lines) and for $\alpha_i = \frac{3\pi}{2}$ (squares, dashed lines) and the theoretically expected curves (solid curve and dashed curve, respectively). The visibility of all fringes is about 91%.*

relative alignment of the two SPPs.

We therefore developed an even more detailed alignment procedure (for details, see Section 8.A.5). With that very tedious procedure (taking ~ 2 weeks), the coincidence fringes became parabolic with good visibility for *all* settings of the idler SPP.

Using this procedure, we obtained the set of four coincidence fringes as a function of the signal SPP orientation α_s, that is shown in Fig. 8.7. The visibility of these fringes is about 91% and they yield a value of the CHSH-Bell parameter equal to $S = 3.0 \pm 0.1$. The quoted error in S is based upon the Poissonian behaviour of the coincidence counts in each of the sixteen measurements. These errors are then propagated through the CHSH-Bell equation (cf. Eq. (7.16)). This value is two standard deviations above the value corresponding to the Bell states, namely $2\sqrt{2}$.

To verify that the beyond-Bell violation can be measured reproducibly, we have realigned the whole setup two times from scratch and performed repeated measurements of the CHSH-Bell parameter, each time with an effort as large as the original, yielding $S = 2.93 \pm 0.06$ and $S = 3.07 \pm 0.06$, four standard deviations above the maximum value for the Bell states. In this set of measurements, the standard deviation is smaller, as we had more coincidence counts and a slightly longer interval in which to measure. The error could be decreased even more by taking a longer measurement interval, were it not for the beam stability effectively

limiting the time of measurement to typically 15 minutes for one parabola.

8.4 Conclusions

We have experimentally investigated the beyond-Bell pairing of twin photons in spontaneous parametric down-conversion, in a setup containing only two analysers and detectors. In the experiment described here, we have obtained a violation of the CHSH-version of the Bell inequality several times, up to a value of $S = 3.07 \pm 0.06$, a value that is four standard deviations above what can be achieved by using twin-photon Bell states.

Acknowledgements

Appendix

8.A Alignment procedure

8.A.1 The analyser unit

The analyser unit that is used in the quantum setup has many knobs, as can be seen in Fig. 8.8, twelve of which have to be adjusted. The central element of the unit is the microscope objective for coupling light into the single-mode fibre. This objective can be aligned to the beam line of signal or idler with the actuators X_u and Y_u, whereby the entire unit is displaced. Relative to this microscope objective, the tip of the single-mode fibre can be positioned by the actuators X_f, Y_f and Z_f. The combination of fibre and objective define a beam line. The purpose of the remaining knobs of the analyser is to position the SPP, contained in a tilt stage (T_x, T_y) and its rotation axis (R) relative to the beam line. The transverse position of the SPP relative to its rotation axis is adjusted by the axes X_s and Y_s, while the SPP's rotation axis is positioned relative to the beam line by the actuators X_r and Y_r. In very early stages of the experiment we used a manual rotation stage (R); this was later replaced by a motorised rotation stage (Newport PR50 series, 0.01° resolution), in each unit. Additionally, the actuators X_u and Y_u, as shown in Fig. 8.8, of the unit placed in the signal path were later replaced by motorised actuators (Newport 850G series, 1.0 µm resolution), to facilitate electronic scanning of the position of the unit.

In the quantum experiment, we use two SPPs that are, in principle, identical, having been made from the same mold (see Chapters 5 and 6). However, one of the SPPs is slightly wedged because of an inaccuracy in positioning the spacer during the molding process (cf. Fig. 5.3). Consequently, it deflects a beam that propagates through it and rotating this SPP steers the transmitted beam. We will come back to this point in Section 8.A.4. To simplify our experiment, we use the wedge-free SPP in the signal analyser, i.e. the analyser that is rotated to measure a single coincidence fringe, while the wedged SPP is included in the idler analyser. The latter SPP is thus only rotated to sample four different coincidence fringes required to calculate the value of the CHSH-Bell parameter.

8.A.2 Alignment of the unit without the spiral phase plate

The preliminary alignment of the entire setup is done by observing the type-II-down-conversion cones at the degenerate wavelength, with an intensified CCD camera positioned in the far field of the nonlinear crystal. The intersections of these cones define two beam lines, the paths of the entangled photons. Each of these beam lines is marked by three pinholes, after which a HeNe laser beam is sent through these pinholes for alignment purposes. Subsequently, the walk-off compensation optics, polariser and telescope in each beam line is aligned relative to the HeNe beam, and the analyser units are positioned appropriately.

In the *first* stage of the alignment of the analysers, when the SPP is not yet included in the analyser units, a diode laser is connected to the output of one of the single-mode fibres. The focus of the fibre tip (Z_f) is adjusted, so that the beam emerging from the microscope objective has a weak focus in the plane where the SPP will be mounted. This is done by
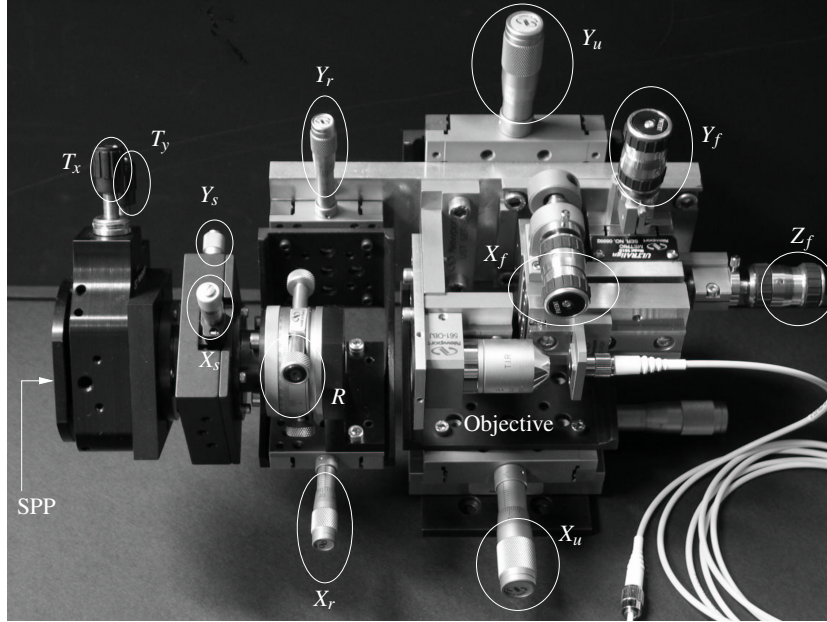
Figure 8.8: *The analyser unit, photographed by Dirk Voigt. The SPP is mounted in a tilt stage (T_x, T_y), which can be translated in the transverse plane (X_s, Y_s). The orientation of this system can be varied with a rotation stage (R). The rotation stage can be translated in the transverse plane with respect to the microscope objective (X_r, Y_r). The fibre position can also be adjusted with respect to the objective (X_f, Y_f and Z_f). Finally, the whole unit can be translated in the transverse plane (X_u, Y_u). For the final experiment, the manual actuators X_u and Y_u of the unit placed in the signal beam have been replaced by stepper-motors.*

imaging the far field of this plane onto a CCD and minimising the diameter of the measured spot, thereby minimising the transverse momentum spread in the SPP plane. From this point on, the focusing is not changed any more. This procedure is repeated for the other analyser unit.

In the *second* stage of the alignment, the single-photon-counting modules are connected to the output of the single-mode fibres and the transverse position of the fibre tip (X_f, Y_f) of both analysers is adjusted for a maximum number of coincidence counts. After this, the *signal* analyser unit as a whole is systematically scanned in the transverse plane (X_u, Y_u, motorised actuators), thereby generating two-dimensional images of both the single and coincidence counts. Because these images represent the near field of the crystal plane, they should both display a Gaussian profile. We compare the profiles and if their positions do not match, the transverse position of the *idler* analyser (X_u, Y_u, manual actuators) is adjusted until they do match. In this way, both analyser units are positioned so that they are centred on the down-converted light, and look at the same spot on the crystal. The position of the fibre tips (X_f, Y_f) is tweaked to investigate whether the number of coincidence counts can be enhanced. In practice, this step gives a null result; it ensures that we are still aligned to the proper photon
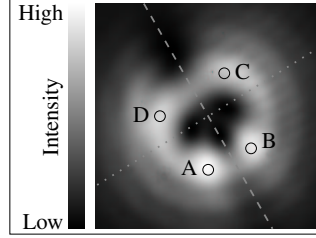
Figure 8.9: *A typical far-field profile that is used to align the SPP. We symmetrise this profile with respect to the dashed line and the intensity at the positions marked A,B,C and D, are measured relative to each other and compared to numerical calculations. Also important is the position of the intersection of the dashed and dotted lines; it must be positioned at the far-field centre of the Gaussian beam when the SPP was absent, as recorded earlier.*

pairs. The coincidence fringes that are obtained when rotating one polariser have a visibility of 95% in the crystal basis and around 92% in the 45°-basis. The photons are thus well entangled with respect to their polarisation. The orientation of the polarisers is then fixed in the crystal basis. The fact that the SPPs are completely polarisation isotropic, as reported in Chapter 5, ensures that this choice of polarisation orientations will not affect the measurement of the spatial entanglement, once the devices are inserted.

8.A.3 Alignment of the spiral phase plate

The *third* and final stage of the alignment is the most critical. Before the SPPs are included in the analyser units, the diode laser is reconnected to the output of the fibres. Its beam profile in the near and far fields of the SPP plane is recorded on a CCD camera, for later use. After this, the SPP is mounted in the unit. Now, we must align three axes relative to each other, namely *(i)* the propagation axis of the down-converted light, *(ii)* the axis around which the rotation stage rotates and *(iii)* the axis of the SPP, around which the surface of the plate spirals.

First, we set the SPP axis parallel to the rotation axis. To this end, we use the HeNe laser, which marks the down-conversion paths, to tilt the SPP (with axes T_x, T_y) in such a way that when it is rotated, the reflection of the HeNe beam off the SPP does not rotate. Note that the angle between the rotation axis and the propagation axis is not very critical as long as the angle between them is small. When this part of the alignment has been done satisfactorily, the HeNe laser is switched off. The SPP axis is now parallel to the rotation axis.

The next task is to have the centre of the SPP coincide with its rotation axis and with the centre of the beam line, so that the SPP can rotate around its own centre *and* is positioned in the centre of the fibre mode. This turns out to be tricky. Using the diode laser and the CCD camera, the near and far fields of the SPP are recorded. In the near field, the central part of the SPP as well as the diode beam can be seen, and are made to overlap by adjusting the SPP position (X_s, Y_s). Subsequently, the SPP is rotated over 180° (R). As, in general, the SPP centre does not coincide with the rotation axis, the centre of the SPP rotates away from the centre of the beam. We then use the positioning of the rotation axis (X_r, Y_r) to move the centre of the SPP *halfway* towards the centre of the beam. After this, the SPP is rotated back

to its previous orientation and again, the SPP position (X_s, Y_s) is adjusted until the centre of the SPP coincides with the centre of the beam profile. Several iterations are required until the three axes overlap. However, it turns out that in the *near field*, the sensitivity to misalignment is not sufficiently high, as witnessed by measuring oddly-shaped coincidence fringes. Thus the alignment steps are repeated while observing the *far field* and looking at its symmetry with respect to the dashed line shown in Fig. 8.9. Also, the intensity distributions on both sides of the dotted line are made similar to calculated far-field profiles. Subsequently, the SPP is rotated in several steps over 360°, to make sure that as the pattern rotates, the intensity distribution within the pattern is not altered.

8.A.4   Wedge compensation

As discussed earlier, the SPP that is included in the idler unit is wedged. Upon insertion of this SPP, the far-field profile as observed with the auxiliary diode laser and the CCD, is therefore displaced with respect to the far field that was recorded without the SPP. Consequently, the idler analyser will detect photons with a different transverse momentum than the polarisation-entangled photons it was aligned to. Additionally, rotating this SPP results not only in a re-orientation of the far-field profile, but also in a displacement. Thus for *each* orientation *separately*, i.e. after *any* rotation of the idler SPP, the wedge of this SPP must be compensated by adjusting the fibre tip in the transverse plane (X_f, Y_f). We do this by positioning the point in Fig. 8.9 that is marked by the intersection of the dashed and dotted lines at the coordinates of the centre of the far-field distribution, which was recorded when the SPP was absent. Note that if the compensation is done with insufficient accuracy, the coincidence fringe has the appearance of that of the curve indicated by the squares in Fig. 8.6.

This wedge compensation must be performed for each of the four settings of the idler analyser, in order to obtain a proper value of the CHSH-Bell parameter. After having performed all these alignment steps, the value of the *S*-parameter hovers around 1.8, whereby the CHSH-Bell inequality is not violated. The reason for this is that not all four settings of the idler SPP yield a parabolic fringe as a function of the signal SPP's orientation.

8.A.5   Fine-tuning of the alignment

As discussed on p. 81, the alignment procedure as described so far, was not accurate enough. By performing numerical simulations on a misaligned setup, we were able to reproduce the faulty coincidence fringes and deduce that the transverse position of the SPP, i.e. the position of the SPP axis with respect to both the rotation and propagation axes, is the most critical one.

We therefore return to the alignment of the signal SPP as discussed in Section 8.A.3. The diode laser is reconnected to the output of the single-mode fibre and the resulting far-field profile is observed. Instead of only looking at the symmetries of the profile, we also study the relative intensities at specific points, marked A, B, C and D in Fig. 8.9, and compare those with the results of numerical calculations. We again adjust the position of the SPP (X_s, Y_s) and that of the rotation stage (X_r, Y_r) at angles (R) of 0° and 180° respectively, trying to match the relative intensities at the chosen points with the calculated values. We have noticed that, most probably due to small imperfections in the SPP, points A and C are always somewhat

stronger than points B and D. Therefore, we only compare the relative intensities of points A and C, and those of points B and D, separately. We note that the sensitivity of the far-field pattern to small adjustments of the SPP's transverse position is just adequate (but no more than that) to do this job properly.

For each of the four idler SPP settings, the wedge is compensated as described in Section 8.A.4, *and* the position of this SPP is adjusted in the same way as the position of the signal SPP, by balancing the intensities at the specific points marked in Fig. 8.9. Note that as we do this for each of the four orientations of the idler SPP, we only need to make the SPP axis coincide with the beam axis; the rotation axis is not important for the idler analyser. By taking these steps, we managed to obtain an CHSH-Bell parameter S larger than 2, though not larger than $2\sqrt{2}$, which is our aim.

Yet another step to improve the alignment is required. It is made in the course of adjusting the position of the idler SPP for each of the four settings of the idler analyser. After having accurately positioned the transverse position of the idler SPP by studying the far-field profile, the detectors are reconnected to both analysers and coincidence counts are observed with the two SPP steps aligned parallel (by rotating the signal SPP). We then fine-tune the position of the idler SPP to optimise coincidence counts. This optimisation procedure is followed for each orientation of the idler SPP. This step may seem to be controversial, as we align one analyser with respect to the other and are basically optimising coincidence counts in *each* basis separately. One could argue that in this way, any value of the CHSH-Bell parameter S may be obtained. This alignment is, however, done with great discretion, which is confirmed by reconnecting the diode laser and estimating how large the transverse adjustments have been. The adjustments turn out to be very small, as the relative intensities of the specific points A,B,C and D in the far-field profile are now off by at most 5%. This compares favourably with the earlier results that differed from theory by approximately 8%. The additional alignment step has therefore at most marginally affected the overall setup.

Having fine-tuned the setup in this way for each setting of the idler SPP, we acquire for each such setting a parabolic coincidence fringe with a visibility $\geq 91\%$. with such fringes, we obtain values of the CHSH-Bell parameter above or close to 3.0.

Bibliography

[1] J. Nye and M. Berry, 'Dislocations in wave trains', Proc. R. Soc. London A **336**, 165–190 (1974).

[2] L. Allen, M. W. Beijersbergen, R. J. C. Spreeuw, and J. P. Woerdman, 'Orbital angular momentum of light and the transformations of Laguerre-Gaussian laser modes', Phys. Rev. A **45**, 8185–8189 (1992).

[3] S. J. van Enk and G. Nienhuis, 'Eigenfunction description of laser beams and orbital angular momentum of light', Opt. Commun. **94**, 147–158 (1992).

[4] S. J. van Enk and G. Nienhuis, 'Commutation rules and eigenvalues of spin and orbital angular momentum of radiation fields', J. Mod. Opt. **41**, 962–978 (1994).

[5] M. W. Beijersbergen, R. P. C. Coerwinkel, M. Kristensen, and J. P. Woerdman, 'Helical-wavefront laser beams produced with a spiral phaseplate', Opt. Commun. **112**, 321–327 (1994).

[6] A. Einstein, B. Podolsky, and N. Rosen, 'Can quantum-mechanical description of physical reality be considered complete?', Phys. Rev. **47**, 777–780 (1935).

[7] J. Bell, 'On the Einstein-Podolsky-Rosen paradox', Physics **1**, 195–200 (1964).

[8] R. A. Bertlmann and A. Zeilinger, eds., *Quantum [un]speakables – from Bell to quantum information* (Springer-Verlag, Berlin, 2002).

[9] D. Kaszlikowski, P. Gnaciński, M. Żukowski, W. Miklaszewski, and A. Zeilinger, 'Violations of local realism by two entangled *N*-dimensional systems are stronger than for two qubits', Phys. Rev. Lett. **85**, 4418–4421 (2000).

[10] A. Vaziri, G. Weihs, and A. Zeilinger, 'Experimental two-photon, three-dimensional entanglement for quantum communication', Phys. Rev. Lett. **89**, 240401 (2002).

[11] D. Bouwmeester, A. Ekert, and A. Zeilinger, *The physics of quantum information* (Springer-Verlag, Berlin, 2000).

[12] A. Zeilinger, 'Experiment and the foundations of quantum physics', Rev. Mod. Phys. **71**, S288–S297 (1999).

[13] L. Mandel, 'Quantum effects in one-photon and two-photon interference', Rev. Mod. Phys. **71**, S274–S282 (1999).

[14] F. De Martini, M. Fortunato, P. Tombesi, and D. Vitali, 'Generating entangled superpositions of macroscopically distinguishable states within a parametric oscillator', Phys. Rev. A **60**, 1636–1651 (1999).

[15] D. Klyshko, *Photons & nonlinear optics* (Gordon and Breach Science Publ., New York, 1988).

[16] D. C. Burnham and D. L. Weinberg, 'Observation of simultaneity in parametric production of optical photon pairs', Phys. Rev. Lett. **25**, 84–87 (1970).

[17] A. Mair, A. Vaziri, G. Weihs, and A. Zeilinger, 'Entanglement of the orbital angular momentum states of photons', Nature **412**, 313–316 (2001).

[18] Perkin-Elmer Optoelectronics, 'Single photon counting module SPCM-AQR series datasheet', (2001).

[19] B. M. Jost, A. V. Sergienko, A. F. Abouraddy, B. E. A. Saleh, and M. C. Teich, 'Spatial correlations of spontaneously down-converted photon pairs detected with a single-photon-sensitive CCD camera', Opt. Express **3**, 81–88 (1998).

[20] C. Kurtsiefer, M. Oberparleiter, and H. Weinfurter, 'High efficiency entangled photon pair collection in type II parametric fluorescence', Phys. Rev. A **64**, 023802 (2001).

[21] A. Ashkin, 'Applications of laser radiation pressure', Science **210**, 1081–1088 (1980).

[22] V. G. Minogin and V. S. Letokhov, *Laser light pressure on atoms* (Gordon and Breach Science Publ., New York, 1986).

[23] A. P. Kazantsev, G. I. Surdutovich, and V. P. Yakovlev, *Mechanical action of light on atoms* (World Scientific, Singapore, 1990).

[24] P. Meystre, *Atom optics* (Springer-Verlag, Berlin, 2001).

[25] R. A. Beth, 'Mechanical detection and measurement of the angular momentum of light', Phys. Rev. **50**, 115–127 (1936).

[26] L. Allen, S. M. Barnett, and M. J. Padgett, *Optical angular momentum* (Institute of Physics Publishing, Bristol, 2003).

[27] H. He, M. E. J. Friese, N. R. Heckenberg, and H. Rubinsztein-Dunlop, 'Direct observation of transfer of angular momentum to absorptive particles from a laser beam with a phase singularity', Phys. Rev. Lett. **75**, 826–829 (1995).

[28] M. E. J. Friese, J. Enger, H. Rubinsztein-Dunlop, and N. R. Heckenberg, 'Optical angular momentum transfer to trapped absorbing particles', Phys. Rev. A **54**, 1593–1596 (1996).

[29] W. J. Firth and D. V. Skryabin, 'Optical solitons carrying orbital angular momentum', Phys. Rev. Lett. **97**, 2450–2453 (1997).

[30] M. Soljačić and M. Segev, 'Integer and fractional angular momentum borne on self-trapped necklace-ring beams', Phys. Rev. Lett. **86**, 420–423 (2001).

[31] J. Leach, M. J. Padgett, S. M. Barnett, S. Franke-Arnold, and J. Courtial, 'Measuring the orbital angular momentum of a single photon', Phys. Rev. Lett. **88**, 257901 (2002).

[32] G. Molina-Terriza, J. P. Torres, and L. Torner, 'Management of the angular momentum of light: preparation of photons in multidimensional vector states of angular momentum', Phys. Rev. Lett. **88**, 013601 (2002).

[33] J. D. Jackson, *Classical electrodynamics* (John Wiley, New York, 1975), 2$^{\text{nd}}$ edition.

[34] C. Cohen-Tannoudji, J. Dupont-Roc, and G. Grynberg, *Photons and atoms* (John Wiley, New York, 1989).

[35] H. Haus, *Waves and fields in optoelectronics* (Prentice-Hall, Englewood Cliffs, NJ, 1984).

[36] J. F. Nye, *Natural focusing and fine structure of light* (Institute of Physics Publishing, Bristol, 1999).

[37] G. Molina-Terriza, J. Recolons, J. P. Torres, L. Torner, and E. M. Wright, 'Observation of the dynamical inversion of the topological charge of an optical vortex', Phys. Rev. Lett. **87**, 023902 (2001).

[38] J. Courtial, K. Dholakia, L. Allen, and M. J. Padgett, 'Gaussian beams with very high orbital angular momentum', Opt. Commun. **144**, 210–213 (1997).

[39] M. V. Berry, 'Paraxial beams of spinning light', in 'International conference on singular optics', (M. S. Soskin, ed.), volume 3487 of *SPIE Proceedings*, 6–11 (SPIE-International Society for Optical Engineering, Bellingham, WA, 1998).

[40] A. T. O'Neill, I. MacVicar, L. Allen, and M. J. Padgett, 'Intrinsic and extrinsic nature of the orbital angular momentum of a light beam', Phys. Rev. Lett. **88**, 053601 (2002).

[41] A. E. Siegman, *Lasers* (University Science Books, Mill Valley, California, 1986).

[42] S. Kuppens, M. Rauner, M. Schiffer, K. Sengstock, W. Ertmer, F. E. van Dorsselaer, and G. Nienhuis, 'Polarization-gradient cooling in a strong doughnut-mode dipole potential', Phys. Rev. A **58**, 3068–3078 (1998).

[43] E. M. Wright, J. Arlt, and K. Dholakia, 'Toroidal optical dipole traps for atomic Bose-Einstein condensates using laguerre-gaussian beams', Phys. Rev. A **63**, 013608 (2000).

[44] I. Basistiy, M. S. Soskin, and M. V. Vasnetsov, 'Optical wavefront dislocations and their properties', Opt. Commun. **119**, 604–612 (1995).

[45] G. F. Brand, 'Phase singularities in beams', Amer. J. Phys. **67**, 55–60 (1999).

[46] S. C. Tidwell, G. H. Kim, and W. D. Kimura, 'Efficient radially polarized laser beam generation with a double interferometer', Appl. Opt. **32**, 5222–5229 (1993).

[47] A. G. Peele, P. J. McMahon, D. Paterson, C. Q. Tran, A. P. Mancuso, K. A. Nugent, J. P. Hayes, E. Harvey, B. Lai, and I. McNulty, 'Observation of an X-ray vortex', Opt. Lett. **27**, 1752–1754 (2002).

[48] C. Rotschild, S. Zommer, S. Moed, O. Hershcovitz, and S. G. Lipson, 'Adjustable spiral phase plate', Appl. Opt. **43**, 2397–2399 (2004).

[49] G. Biener, A. Niv, V. Kleiner, and E. Hasman, 'Formation of helical beams by use of Pancharatnam-Berry phase optical elements', Opt. Lett. **27**, 1875–1877 (2002).

[50] M. W. Beijersbergen, L. Allen, H. E. L. O. van der Veen, and J. P. Woerdman, 'Astigmatic laser mode converters and transfer of orbital angular momentum', Opt. Commun. **96**, 123 (1993).

[51] M. W. Beijersbergen, *Phase singularities in optical beams*, Ph.D. thesis, Universiteit Leiden (1996).

[52] N. Bloembergen, 'Conservation of angular momentum for optical processes in crystals', in 'Polarisation, Matière et Rayonnement', (C. Cohen-Tannoudji, ed.), 109–119 (Presses Universitaires, Paris, 1969).

[53] N. Bloembergen, 'Conservation laws in nonlinear optics', J. Opt. Soc. Am. **70**, 101–108 (1980).

[54] S. Franke-Arnold, S. M. Barnett, M. J. Padgett, and L. Allen, 'Two-photon entanglement of orbital angular momentum states', Phys. Rev. A **65**, 033823 (2002).

[55] J. Arlt, K. Dholakia, L. Allen, and M. J. Padgett, 'Parametric down-conversion for light beams possessing orbital angular momentum', Phys. Rev. A **59**, 3950–3952 (1999).

[56] M. J. Padgett, J. Courtial, L. Allen, S. Franke-Arnold, and S. M. Barnett, 'Entanglement of orbital angular momentum for the signal and idler beams in parametric down-conversion', J. Mod. Opt. **49**, 777–785 (2002).

[57] H. H. Arnaut and G. A. Barbosa, 'Orbital and intrinsic angular momentum of single photons and entangled pairs of photons generated by parametric down-conversion', Phys. Rev. Lett. **85**, 286–289 (2000).

[58] E. R. Eliel, S. M. Dutra, G. Nienhuis, and J. P. Woerdman, 'Comment on 'orbital and intrinsic angular momentum of single photons and entangled pairs of photons generated by parametric down-conversion'', Phys. Rev. Lett. **86**, 5208 (2001).

[59] G. Indebetouw, 'Optical vortices and their propagation', J. Mod. Opt. **40**, 73–87 (1993).

[60] F. S. Roux, 'Dynamical behavior of optical vortices', J. Opt. Soc. Am. B **12**, 1215–1221 (1995).

[61] M. J. Padgett, J. Arlt, and N. Simpson, 'An experiment to observe the intensity and phase structure of Laguerre-Gaussian laser modes', Amer. J. Phys. **64**, 77–82 (1996).

[62] M. S. Soskin, V. N. Gorshkov, M. V. Vasnetsov, J. T. Malos, and N. R. Heckenberg, 'Topological charge and angular momentum of light beams carrying optical vortices', Phys. Rev. A **56**, 4064–4075 (1997).

[63] N. R. Heckenberg, R. McDuff, C. Smith, H. Rubinsztein-Dunlop, and M. J. Wegener, 'Laser beams with phase singularities', Opt. Quant. Elec. **24**, 5951–5962 (1992).

[64] D. Rozas, C. T. Law, and G. A. Swartzlander, 'Propagation dynamics of optical vortices', J. Opt. Soc. Am. B **14**, 3054–3065 (1997).

[65] Z. S. Sacks, D. Rozas, and G. A. Swartzlander, 'Holographic formation of optical-vortex filaments', J. Opt. Soc. Am. B **15**, 2226–2234 (1998).

[66] I. Basistiy, V. Y. Bazhenov, M. S. Soskin, and M. V. Vasnetsov, 'Optics of light beams with screw dislocations', Opt. Commun. **103**, 422–428 (1993).

[67] M. V. Vasnetsov, I. V. Basistiy, and M. S. Soskin, 'Free-space evolution of monochromatic mixed screw-edge wavefront dislocations', in 'International conference on singular optics', (M. S. Soskin, ed.), volume 3487 of *SPIE Proceedings*, 29–33 (SPIE-International Society for Optical Engineering, Bellingham, WA, 1998).

[68] M. Abramowitz and I. A. Stegun, eds., *Handbook of mathematical functions* (Dover, New York, 1965).

[69] A. Y. Bekshaev, M. V. Vasnetsov, V. G. Denisenko, and M. S. Soskin, 'Transformation of the orbital angular momentum of a beam with optical vortex in an astigmatic optical system', JETP Lett. **75**, 127–130 (2002).

[70] H. H. Arnaut and G. A. Barbosa, 'Reply by Arnaut and Barbosa', Phys. Rev. Lett. **86**, 5209 (2001).

[71] V. Y. Bazhenov, M. S. Soskin, and M. V. Vasnetsov, 'Screw dislocations in light wavefronts', J. Mod. Opt. **39**, 985–990 (1992).

[72] J. Andrea, 'Mass-production of diffraction limited replicated objective lenses for Compact-Disc players', in 'Micromachining of Elements with Optical and Other Submicrometer Dimensional and Surface Specifications', (M. Weck, ed.), volume 803 of *SPIE Proceedings*, 3–7 (SPIE-International Society for Optical Engineering, Bellingham, WA, 1987).

[73] T. G. Gijsbers, 'COLATH, a numerical controlled lathe for very high precision', Philips Tech. Rev. **39**, 229–244 (1980).

[74] A. V. Husakou and J. Herrmann, 'Supercontinuum generation of higher-order solitons by fission in photonic crystal fibers', Phys. Rev. Lett. **87**, 203901 (2001).

[75] J. G. Kloosterboer, 'Network formation by chain crosslinking photopolymerization and its applications in electronics', Adv. Polym. Sci. **84**, 1–61 (1988).

[76] J. Preskill, 'Battling decoherence: the fault-tolerant quantum computer', Phys. Today **52**, 24–30 (1999).

[77] P. G. Kwiat, K. Mattle, H. Weinfurter, and A. Zeilinger, 'New high-intensity source of polarization-entangled photon pairs', Phys. Rev. Lett. **75**, 4337–4341 (1995).

[78] G. A. Barbosa and H. H. Arnaut, 'Twin photons with angular-momentum entanglement: phase matching', Phys. Rev. A **65**, 053801 (2002).

[79] J. P. Torres, Y. Deyanova, L. Torner, and G. Molina-Terriza, 'Preparation of engineered two-photon entangled states for multidimensional quantum information', Phys. Rev. A **67**, 052313 (2003).

[80] J. Visser and G. Nienhuis, 'Interference between entangled photon states in space and time', Eur. Phys. J. D **29**, 301–308 (2004).

[81] N. D. Mermin, 'Quantum mechanics versus local realism near the classical limit: a Bell inequality for spin s', Phys. Rev. D **22**, 356–361 (1980).

[82] A. Peres, 'Finite violation of a Bell inequality for arbitrarily large spin', Phys. Rev. A **46**, 4413–4414 (1992).

[83] T. Durt, D. Kaszlikowski, and M. Żukowski, 'Violations of local realism with quantum systems described by N-dimensional Hilbert spaces up to $N = 16$', Phys. Rev. A **64**, 024101 (2001).

[84] D. Collins, N. Gisin, N. Linden, S. Massar, and S. Popescu, 'Bell inequalities for arbitrarily high-dimensional systems', Phys. Rev. Lett. **88**, 040404 (2002).

[85] J. F. Clauser, M. A. Horne, A. Shimony, and R. A. Holt, 'Proposed experiment to test local hidden-variable theories', Phys. Rev. Lett. **23**, 880–884 (1969).

[86] A. Peres, *Quantum theory: concepts and methods* (Kluwer Academic Publishers, Dordrecht, 1993).

[87] A. Garuccio and V. A. Rapisarda, 'Bell's inequalities and the four-coincidence experiment', Nuovo Cimento **65A**, 269–297 (1981).

[88] J. F. Clauser and M. A. Horne, 'Experimental consequences of objective local theories', Phys. Rev. D **10**, 526–535 (1974).

[89] A. N. Oppenheim and R. W. Shafer, *Digital Signal Processing* (Prentice-Hall, Englewood Cliffs, New Jersey, 1975).

[90] S. N. Khonina, V. V. Kotlyar, M. V. Shinkaryev, V. A. Soifer, and G. V. Uspleniev, 'The phase rotor filter', J. Mod. Opt. **39**, 1147–1154 (1992).

[91] A. V. Belinskii and D. N. Klyshko, 'Two-photon optics: diffraction, holography, and transformation of two-dimensional signals', Sov. Phys.–JETP **78**, 259–262 (1994).

[92] D. V. Strekalov, A. V. Sergienko, D. N. Klyshko, and Y. H. Shih, 'Observation of two-photon "ghost" interference and diffraction', Phys. Rev. Lett. **74**, 3600–3603 (1995).

Summary

The aim of the research described in this thesis, is to investigate the quantum entanglement of spatial degrees of freedom of photons, by using optical dislocations. In this summary, we explain the main subjects of this thesis, namely 'optical dislocations' and 'quantum entanglement', and clarify related concepts such as 'photons'.
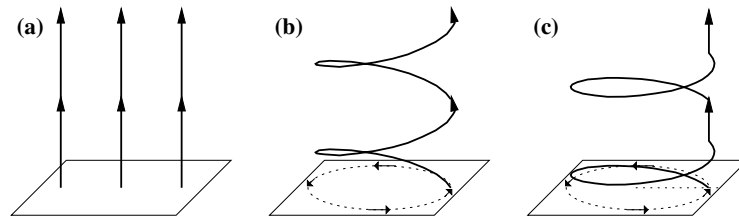
Figure 8.1: *The analogy between a water surface and the behaviour of a beam of light. (a) A perfectly plane surface corresponds to a parallel beam of light. (b) A vortex in the surface (dotted curve, direction of rotation is indicated by the small arrows) makes the rays spin around the core of the beam. (c) When a broken vortex occurs in the surface, the rays of light spin around, jump up and spin again, and so on. The break (dotted horizontal line) in the vortex (dotted curve) is located in the centre of the beam towards the right.*

Optical dislocations

Waves in light

In classical physics, light is considered as a wave phenomenon. If we imagine a light beam propagating upwards, we can consider a horizontal plane through this beam as a water surface. If the surface is perfectly plane, it corresponds to a beam of light in which the rays of light are all parallel. This is schematically shown in Fig. 8.1(a). A certain wave pattern in the water surface corresponds to a certain behaviour of the light beam during propagation. It is possible that dislocations occur in the water surface. In this thesis, we mainly examine beams containing dislocations. The dislocations manifest themselves as a change in the beam profile when the beam propagates.

Dislocations

The vortex

A well-known dislocation in a water surface is the whirlpool or vortex. In the centre of the vortex, the surface is dislocated; while the water spins around the vortex, there is no movement of water in the vortex core itself. Vortices can also occur in light beams. While the beam propagates, the light spins around the dislocation, as depicted in Fig. 8.1(b), and illustrates why the vortex is also called a screw dislocation. Such a dislocation can be generated in a beam with a spiral phase plate (cf. Fig. 8.2(a)). When a normal beam (with a profile as shown in Fig. 8.2(b)) propagates through the spiral phase plate, the centre of the beam, where the vortex is located, becomes dark (cf. Fig. 8.2(c)).

In Chapter 4, we research the relation between the 'velocity' with which the light spins around the vortex, and the position where the vortex is created in the beam. It appears that when the vortex is created farther away from the beam's centre, the light will spin slower. We also investigate what happens with the light when two vortices, either spinning in the same or opposite directions, are generated inside a beam of light, and study the beam profile after it has propagated over a large distance.
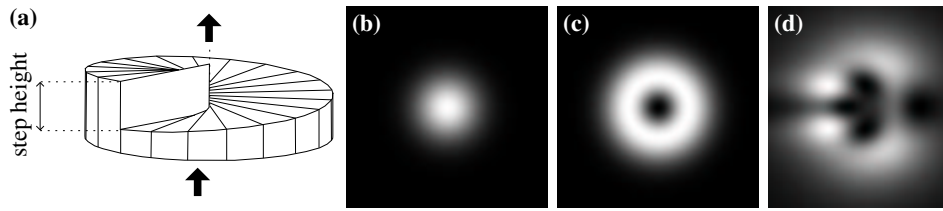
Figure 8.2: *Vortices in light beams. (a) A spiral phase plate can make two types of vortices, depending on the step height. (b) A normal light beam has a simple profile. (c) The profile of a beam containing a vortex, far away from the spiral phase plate, looks like a doughnut, while (d) the profile of a beam containing a broken vortex looks more complicated (the doughnut has been broken).*

Since spiral phase plates (cf. Fig. 8.2(a)) are an important part of the research, obtaining plates of excellent quality was of great importance. In Chapter 5, a new method of fabrication of high-quality spiral phase plates is discussed. We also report on the various tests that we have performed on the produced spiral phase plates, and notice that it is possible to generate *another* dislocation, namely the broken vortex.

The broken vortex

Depending of the step height of the spiral phase plate (indicated in Fig. 8.2(a)), it is possible to generate a so-called mixed screw-edge dislocation, or broken vortex, in a light beam. There is no analogy of a broken vortex in a water surface. It differs from a normal vortex in that the light spins around once, then jumps on, then spins around once again, and so on, as illustrated in Fig. 8.1(c). The broken vortex is explored in Chapters 5 and 6. After a light beam containing such a broken vortex has propagated, the beam profile has a complicated pattern (cf. Fig. 8.2(d)). The agreement with theoretical predictions and the experimental results is excellent. Chapter 6 shows it is experimentally feasible to remove the broken vortex from the light beam again, by generating an identical broken vortex, but with an opposite spinning direction, in the beam. The experiment shows that the produced spiral phase plates are indeed of excellent quality.

Quantum entanglement

Light as a wave-particle

Up to now, we have considered light as a wave. Quantum mechanics provides an entirely different description of light. Light is broken up into the smallest discrete quantities of energy, as if they were particles. These 'quanta' are called photons.

These photons, as every particle in quantum mechanics, behave in a remarkable way; a single particle behaves like a wave and as such, it can spread out over a large volume of space. However, when trying to detect this particle, it can only be found at a single position at a given time. As this is hard to imagine, we illustrate this with a seismic wave that originates in a small earthquake in the east of the Netherlands (cf. Fig. 8.3). As the seismic wave
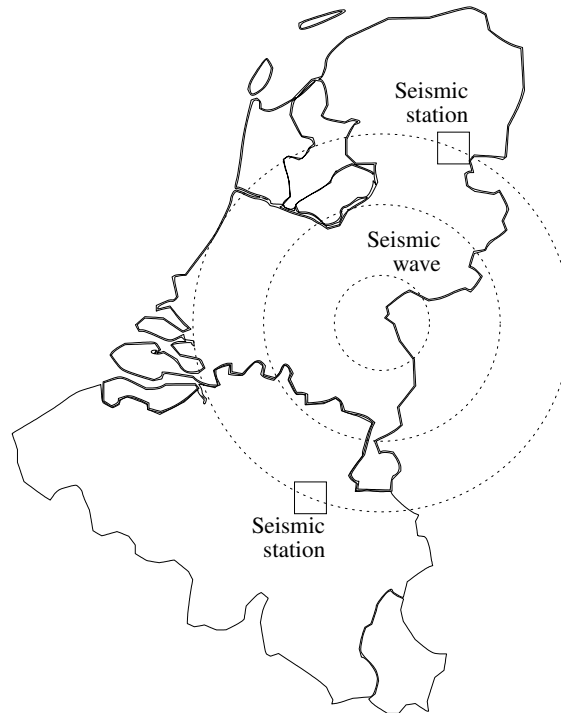
Figure 8.3: *A seismic wave originating in the east of the Netherlands. This wave will be detected by both seismic stations as the wave passes them. If the seismic wave would have been a quantum phenomenon, such as a photon, only one of the stations would detect it, after which the wave would immediately cease to exist.*

expands, it will pass the seismic stations in the Netherlands and Belgium, where it will be detected. However, if this seismic wave would have been a photon, just one station would be able to actually measure it, and not all of the stations, as is normal with seismic waves. As soon as the 'quantum mechanical earthquake' is detected by one of the seismic stations, it would completely disappear. As earthquakes are not quantum, they will be detected by all stations without disappearing immediately after detection. However, photons *are* quantum mechanical particles and therefore behave differently: as a wave, to describe how they spread out, and as a particle, to explain detection; one particle can only be detected by one station.

Before detection, the wave nature of the photon describes how it spreads out in space. Actually, the wave describes the *probability* of detecting the particle at a specific position. The photon can be said to be in multiple states at the same time, where every state describes a possible path. This is called superposition. For a classical particle, such as a soccer ball or a marble, this is impossible. The probability to find that the marble at a specific position is not spread out in space, as the marble has a well-determined position at any given time; the marble will always be in only one state, as it can only follow one path at a time. Thus it is difficult to imagine a photon in a superposition state. Nevertheless, this phenomenon is of fundamental importance to the quantum-mechanical part of this research.
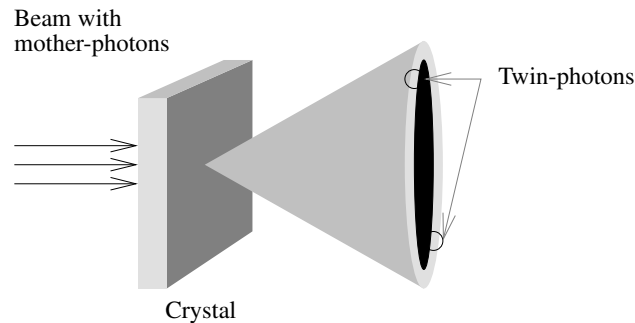
Figure 8.4: *The conversion of a mother-photon into twin-photons, inside a crystal. The twin-photons leave the crystal in the shape of a cone. During detection, the twin-photons are localised on the ring opposite to one another.*

Entanglement

Although a photon also has a particle nature, it is possible, under the right circumstances, to split the photon into two photons. During this process, the 'mother-photon' (e.g. an ultra-violet photon) is converted into two 'daughter-photons' (e.g. infrared photons). This process occurs in a certain crystal, and is named 'spontaneous parametric down-conversion'. An important condition for this process to occur, is that the energy of the daughter-photons together is equal to the energy of the mother-photon. Of course, there are many ways to distribute the energy over the two daughter-photons. The most interesting case occurs when each daughter-photon receives exactly half the energy of the mother-photon; the daughter-photons then become 'identical twins'. In the process described in Chapter 2, these twin-photons are emitted from the crystal in the shape of a conical beam. The profile of this beam is a ring, as shown in Fig. 8.4. The wave nature of each of the twin photons covers the ring, but when detected, each photon will be found on its own specific position on this ring.

Since these photons are born at the same moment under identical conditions, they are strongly correlated with respect to various properties. In Chapter 2, we demonstrate one of these properties; the twin-photons will always be detected on opposite sides on the ring, no matter which of the two is detected first (cf. Fig. 8.4).

The result is that the spatial information of each photon individually, e.g. if it contains a dislocation, is not determined before detection. Only the spatial information of the twin-photon *pair* is fixed. Thus each of the twin-photons is in a superposition of spatial states, in such a way that the spatial state of the *pair* is conserved. For instance, each of the twin-photons is in a superposition of dislocation states, such as vortices. If one of the photons after detection, appears to possess a vortex spinning clockwise, the other photon will immediately fall out of the superposition into a state where it contains a vortex that spins counter-clockwise. Even though the photons have moved away from each other, measuring one photon means implicitly measuring the other photon at that same instant in time. It is as though the photons, while physically separated, are still connected somehow; they are *entangled*.

This quantum entanglement is a highly counter-intuitive phenomenon. This is due to the fact that a *local* event, i.e. an event that is limited only to the part of space where one

photon resides, *still* influences the other photon, which is in an entirely different part of space. Entanglement is often seen as the evidence of the fact that quantum-mechanical states can be 'non-local'; in this case, the state in question describes *two* photons that are separated by an *arbitrarily large* distance, but possess a common history where they have interacted, such as their birth. A stronger entanglement indicates a stronger non-local behaviour of the state.

In the past 20 years, entanglement has been measured many times and thus non-locality has been proven. A quantitative measure for the strength of entanglement and therefore a measure of the non-locality of the state, is the so-called Bell parameter, indicated by the symbol S. In the absence of entanglement, the Bell parameter can have values between 0 and 2. In that case, the correlations between each of the twin-photons is purely classical. They are no different from the correlation between the colour of someone's left and right eye; if the left eye is brown, the right eye is also brown, and the colour is fixed for each individual eye. When entanglement occurs, the value of the Bell parameter becomes larger than 2. That would compare to a correlation between the colour of someone's left and right eye, where both eyes have the same colour, but the colour for each eye is not fixed. Since this does not happen in our everyday life, this type of correlation is hard to imagine. An explanation for this behaviour with twin-photons is provided by quantum mechanics in the form of entanglement.

Nowadays, values of the Bell parameter slightly less than or equal to 2.8 are measured without much effort. In Chapter 7, we theoretically predict that a new approach, namely by using the aforementioned spiral phase plates, could uncover the strongest entanglement ever, with $S = 3.2$. The idea is to see to what extent the twin-photons posses a *broken* vortex. In this case, not only the direction in which the spinning occurs is entangled, but also the orientation of the break in the vortex. It appears that, if one photon is detected with a certain vortex and a certain orientation of the break, the other photon possesses the complementary vortex with the same orientation of the break. In Chapter 8, we describe an experiment in which we finally, after much hard work, manage to measure and report the strongest entanglement up until now, namely $S = 3.0$.

Samenvatting

Het onderzoek dat beschreven wordt in dit proefschrift, richt zich op de verstrengeling van ruimtelijke vrijheidsgraden van fotonen, met behulp van optische dislocaties. In deze samenvatting leggen we de hoofdonderwerpen van dit proefschrift uit, namelijk 'optische dislocaties' en 'quantum verstrengeling', en verklaren gerelateerde termen als 'fotonen'.
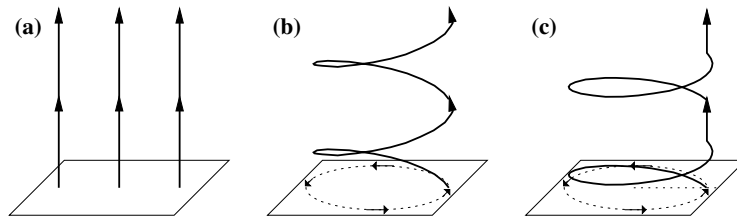
Figuur 1: *De analogie met een wateroppervlak en het gedrag van een lichtbundel. (a) Een volledig strak oppervlak correspondeert met een parallelle lichtbundel. (b) Een draaikolk in het oppervlak (gestippelde curve met draairichting aangegeven door de kleine pijlen) zorgt ervoor dat de stralen rondkolken. (c) Bij een gebroken draaikolk draait het licht rond, springt dan even, draait vervolgens weer rond enzovoorts. De breuk (gestippelde horizontale lijn) in de draaikolk (gestippelde curve) begint in het midden en gaat naar rechts.*

Optische dislocaties

Golven in licht

Licht wordt in de klassieke natuurkunde als een golfverschijnsel beschouwd. Als we ons een lichtbundel voorstellen die van onder naar boven beweegt, dan kunnen we ons een horizontaal vlak binnen die bundel voorstellen als bijvoorbeeld een wateroppervlak. Als het oppervlak perfect strak is, dan correspondeert dat met een lichtbundel waarin de lichtstralen allemaal parallel zijn. Dit is geschetst in fig. 1(a). Als er in het wateroppervlak een bepaald golfpatroon ontstaat, dan correspondeert dat met een bepaald gedrag van de lichtbundel. Het is mogelijk dat er in het wateroppervlak dislocaties, ook wel ontwrichtingen genoemd, optreden. In dit proefschrift wordt voornamelijk onderzoek gedaan naar lichtbundels met dislocaties. Het effect van deze dislocaties is te merken in het bundelprofiel, dat verandert naarmate het licht zich voortplant.

Dislocaties

De draaikolk

Een bekende dislocatie in een wateroppervlak is de draaikolk. In het midden van de draaikolk is het oppervlak ontwricht; terwijl al het water zich om deze plek heen beweegt, is er geen beweging op die plek zelf. De draaikolk kan ook optreden in een lichtbundel. Terwijl de lichtbundel zich voortplant, kolkt het licht om de ontwrichting heen, zoals aangegeven in fig. 1(b). Deze ontwrichting wordt ook wel een verdraaiïng of schroefdislocatie genoemd. Deze kan in een lichtbundel gegenereerd worden met behulp van een spiraalfaseplaat (zie fig. 2(a)). Als een normale lichtbundel (zie voor het profiel fig. 2(b)) door de spiraalfaseplaat gaat, ontstaat er na voortplanting een donkere plek op de plaats van de ontwrichting, zoals te zien in fig. 2(c).

In hoofdstuk 4 onderzoeken we de relatie tussen de 'snelheid' waarmee het licht rondkolkt en de plaats waar de draaikolk wordt gecreëerd in de lichtbundel. Het blijkt dat hoe verder de draaikolk uit het centrum van het bundelprofiel staat, hoe langzamer het licht zal
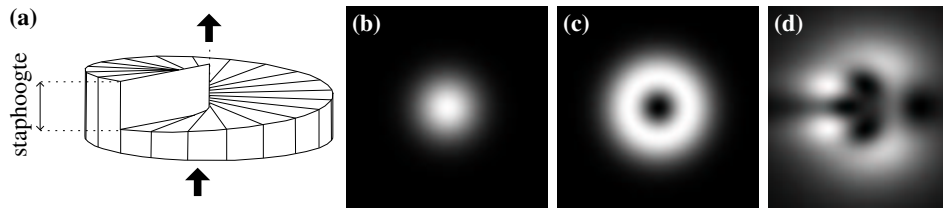
Figuur 2: *Draaikolken in lichtbundels. (a) Een spiraalfaseplaat kan, afhankelijk van de staphoogte, twee soorten draaikolken maken. (b) Een normale lichtbundel heeft een eenvoudig profiel. (c) Het profiel van een lichtbundel met een draaikolk ziet er, na voortplanting, uit als een donut, terwijl (d) het profiel van een bundel met een gebroken draaikolk er ingewikkelder uit ziet (de donut is gebroken).*

rondkolken. In datzelfde hoofdstuk onderzoeken we ook wat er gebeurt met het licht als er zich twee draaikolken in de lichtbundel bevinden, die of dezelfde of de tegenovergestelde kant op draaien, en onderzoeken hoe het bundelprofiel er ver weg uit ziet in die gevallen.

Aangezien spiraalfaseplaten (zie fig. 2(a)) een belangrijk element van het beoogde onderzoek vormen, was het van groot belang dat we over spiraalfaseplaten van uitstekende kwaliteit zouden beschikken. In hoofdstuk 5 wordt een nieuwe methode beschreven voor het maken van zeer nauwkeurige spiraalfaseplaten. In dat hoofdstuk testen we de platen op allerlei eigenschappen en merken op dat het mogelijk is om met de gefabriceerde spiraalfaseplaat ook een *andere* ontwrichting te maken, namelijk de gebroken draaikolk.

De gebroken draaikolk

Afhankelijk van de staphoogte van de spiraalfaseplaat (aangegeven in fig. 2(a)), is het mogelijk om een zogenaamde gebroken draaikolk in het licht te veroorzaken. Er bestaat geen equivalent van de gebroken draaikolk in een wateroppervlak. Het verschil met een gewone draaikolk is, dat de kolk nu een breuk bevat. Het licht kolkt rond en zodra het de breuk bereikt, verspringt het, waarna het weer verder gaat met de kolkende beweging. Dit is geschetst in fig. 1(c). De gebroken draaikolk wordt onderzocht in de hoofdstukken 5 en 6. Na voortplanting van een lichtbundel met een gebroken draaikolk blijkt het profiel een rijke structuur te hebben (zie fig. 2(d)). De overeenstemming van de theorie en de experimentele resultaten is zeer goed. Hoofdstuk 6 laat zien dat het experimenteel ook zeer goed mogelijk is om een gebroken draaikolk op te heffen met een identieke gebroken draaikolk die in de tegengestelde richting draait. Op grond van alle metingen kan worden geconcludeerd dat de geproduceerde spiraalfaseplaten van uitstekende kwaliteit zijn.

Quantumverstrengeling

Licht als golfpakketje

Hiervoor hebben we gesproken over licht als een golf. In de quantummechanica wordt licht echter geheel anders beschreven. Licht kan namelijk opgebroken worden in de kleinste, discrete hoeveelheden van energie, alsof het deeltjes waren. Deze 'quanta' worden fotonen
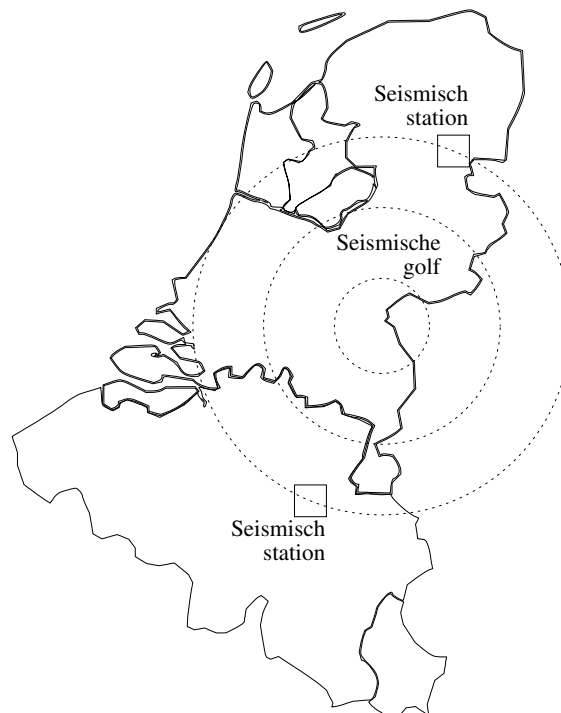
Figuur 3: *Een seismische golf die ontstaan is in het oosten van Nederland. Deze golf wordt door beide seismische stations waargenomen. Als de seismische golf een quantummechanisch fenomeen zoals een foton was geweest, zou slechts één van de stations hem kunnen waarnemen, waarna de golf onmiddellijk verdwijnt.*

genoemd.

Het merkwaardige van deze fotonen, en van de quantummechanica in het algemeen, is dat een enkel energiepakketje zich gedraagt als een golf en zich dus uit kan spreiden over de ruimte, maar slechts één maal en op één positie waargenomen kan worden. Dit is eigenlijk nauwelijks voor te stellen. Laten we ter vergelijking eens nadenken over een seismische golf die ontstaat bij een aardbeving in het oosten van Nederland, zoals te zien in fig. 3. De seismische golf breidt zich uit en zal door seismische stations in Nederland en België worden waargenomen. Echter, als deze seismische golf een foton was geweest, dan zou slechts één van de stations de golf hebben kunnen meten en niet allemaal, zoals dat normaal gebeurt bij seismische golven. Op het moment dat de 'quantumaardschok' door één van de seismische stations wordt waargenomen, verdwijnt deze in zijn geheel. Aardschokken zijn niet quantum en worden dus door alle stations waargenomen, zonder te verdwijnen. Fotonen zijn wel quantum en gedragen zich anders: als golf om de uitbreiding te beschrijven en als deeltje om de waarneming te verklaren; één deeltje kan immers slechts door één station gemeten worden.

Vóór detectie beschrijft het golfkarakter van het foton dus hoe het foton is 'uitgesmeerd' over de ruimte. Beter gezegd, het golfkarakter beschrijft eigenlijk de *kans* om het deeltje op

Bundel
moederfotonen

Tweelingfotonen
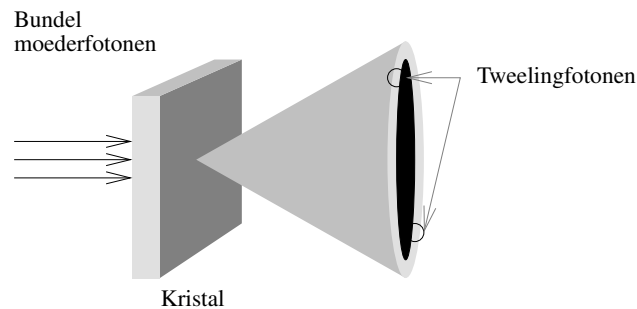
Kristal

Figuur 4: *De splitsing van een moederfoton in tweelingfotonen in een kristal. Deze verlaten het kristal in de vorm van een kegel. Bij waarneming komt elk van de tweelingfotonen ergens op de ring terecht, zodat ze tegenover elkaar liggen.*

een bepaalde plaats waar te nemen. Dit betekent dat het foton zich in een 'opeenstapeling' van toestanden bevindt, waarbij elke toestand een mogelijk pad beschrijft. Dit noemt men superpositie. Voor een klassiek deeltje, zoals een voetbal of een knikker, bestaat dit niet. De kans om de knikker op een specifiek pad te vinden is niet uitgesmeerd, aangezien de knikker op ieder gegeven moment zich slechts op één plaats bevindt; de knikker is altijd in een toestand waarin het slechts één pad op elk moment volgt en niet meerdere paden tegelijkertijd. Het is daarom uitermate moeilijk voor te stellen dat een foton zich in een superpositietoestand kan bevinden. Desondanks is dit effect van fundamenteel belang voor het quantummechanische deel van dit onderzoek.

Verstrengeling

Alhoewel een foton ook een deeltjeskarakter heeft, is het onder bepaalde omstandigheden mogelijk om een foton in tweeën te splitsen. Hierbij wordt een 'moederfoton' (bijvoorbeeld een ultra-violet foton) omgezet naar twee 'dochterfotonen' (bijvoorbeeld een infrarood foton). Dit proces vindt plaats in een kristal en heet 'spontane parametrische splitsing'. De eis hierbij is dat de energie van de twee dochterfotonen samen optelt tot die van het moeder foton. Dit kan uiteraard op vele verschillende manieren. Het interessantste geval vindt plaats als de dochterfotonen ieder precies de helft van de energie van het moederfoton oppakken; de dochterfotonen zijn in dat geval identiek, net als een ééneiïge tweeling. Deze 'tweelingfotonen' komen bij het splitsingsproces zoals gebruikt in hoofdstuk 2 als een kegelvormige bundel uit het kristal. Het profiel van deze bundel is dus een ring, zoals te zien in fig. 4. Het golfkarakter van elk van de tweelingfotonen beslaat dus de gehele ring, maar bij waarneming komt elk foton ergens op deze ring terecht.

Aangezien deze fotonen op hetzelfde moment en onder dezelfde omstandigheden geboren zijn, vertonen ze sterke correlaties. In hoofdstuk 2 demonstreren we er één van; de tweelingfotonen bevinden zich altijd tegenover elkaar op de ring, ongeacht welk van de twee fotonen het eerst waargenomen wordt (zie ook fig. 4).

Het gevolg hiervan is dat de ruimtelijke informatie over elk foton, bijvoorbeeld of het een ontwrichting bevat, niet vast ligt voor detectie. Wat *wel* vast ligt, is de *gezamenlijke* ruimtelijke informatie. Dientengevolge bevindt ieder foton zich in een superpositie van ruimtelijke

toestanden, op een dusdanige manier dat de gezamenlijke informatie behouden blijft. Zo zit bijvoorbeeld elk van de twee fotonen in een superpositietoestand van allerlei ontwrichtingen, zoals draaikolken. Mocht het ene foton na inslag op het meetapparaat, een linksdraaiende draaikolk blijken te hebben, dan zal het andere foton *op datzelfde moment* onmiddellijk uit zijn superpositie vallen en direct in een complementaire, rechtsdraaiende draaikolk vervallen. Ondanks dat de fotonen ver van elkaar zijn verwijderd, resulteert de meting van het ene foton in een onmiddellijke, impliciete meting van het andere foton. Het is alsof de twee fotonen, alhoewel fysiek gescheiden, nog steeds met elkaar verbonden zijn; ze zijn *verstrengeld*.

Deze verstrengeling is in hoge mate een tegenintuïtief effect. Dit heeft te maken met het feit dat een *lokale* gebeurtenis, dat wil zeggen, een gebeurtenis die zich in een beperkt deel van de ruimte afspeelt en maar op één foton betrekking heeft, *toch* invloed heeft op het andere foton, dat zich in een ander ver weg gelegen deel van de ruimte bevindt. Verstrengeling wordt daarom wel gezien als het bewijs van het 'niet-lokaal' zijn van quantummechanische toestanden; in dit geval beslaat de toestand *twee* fotonen die zich *willekeurig ver* van elkaar kunnen bevinden, met als voorwaarde dat ze eens een interactie hebben gehad, zoals hun gezamenlijke geboorte. Hoe sterker de verstrengeling is, hoe sterker het niet-lokale gedrag van de toestand is.

Verstrengeling is in de afgelopen 20 jaren al vaak gemeten en zodoende is ook de niet-lokaliteit bewezen. Een maat voor de sterkte van de verstrengeling en dus ook een maat voor niet-lokaliteit, is de zogenaamde Bell-parameter, aangegeven met het symbool S. Bij de afwezigheid van verstrengeling kan deze Bell-parameter liggen tussen 0 en 2. In dat geval zijn er wel correlaties tussen de fotonen, maar deze zijn klassiek. De correlaties zijn op dat moment niet anders dan de correlatie tussen de kleur van iemands linker- en rechteroog; als het linkeroog bruin is, dan is het rechteroog dat ook, maar de kleur ligt individueel al vast. Bij verstrengeling zal de waarde hoger dan 2 worden. Dat zou vergelijkbaar zijn met de correlatie tussen de kleur van de ogen waarbij beide ogen dezelfde kleur moeten hebben, maar de kleur van ieder oog op zich nog niet vast ligt. Aangezien dit nooit gebeurt in het dagelijks leven, is dit moeilijk voor te stellen. Een verklaring voor dit gedrag bij de tweelingfotonen wordt dus gegeven door de quantummechanica in de vorm van verstrengeling.

Tot nu toe worden waarden van de Bell-parameter iets kleiner dan of gelijk aan 2.8 zonder veel moeite in het lab gemeten. In hoofdstuk 7 laten we theoretisch zien dat met een nieuwe benadering, namelijk met behulp van de eerder besproken spiraalfaseplaten, een verstrengeling aangetoond kan worden die *sterker* is dan eerder is geobserveerd, namelijk een verstrengeling met $S = 3.2$. Dit idee is gebaseerd op het feit dat we kijken in welke mate de tweelingfotonen een *gebroken* draaikolk bevatten. In dit geval is niet alleen de draairichting van de draaikolk in het foton verstrengeld, maar ook de oriëntatie van de breuk. Het blijkt dat als het ene foton gedetecteerd wordt met een bepaalde draaikolk en een bepaalde oriëntatie van de breuk, het andere foton de complementaire draairichting met een breuk in dezelfde richting heeft. In hoofdstuk 8 beschrijven we een experiment waarin we uiteindelijk, met veel moeite, de sterkste verstrengeling die ooit gemeten is, rapporteren, namelijk met $S = 3.0$.

List of publications

- *Laser with thresholdless intensity fluctuations*, N. J. van Druten, Y. Lien, C. Serrat, S. S. R. Oemrawsingh, M. P. van Exter, and J. P. Woerdman, Phys. Rev. A **62**, 053808 (2000).

- *Observation of transverse modes in a microchip laser with combined gain and index guiding*, N. J. van Druten, S. S. R. Oemrawsingh, Y. Lien, C. Serrat, M. P. van Exter, and J. P. Woerdman, J. Opt. Soc. Am. B **18**, 1793–1804 (2001).

- *Two-dimensional wave-vector correlations in spontaneous parametric down-conversion explored with an intensified CCD camera*, S. S. R. Oemrawsingh, W. J. van Drunen, E. R. Eliel, and J. P. Woerdman, J. Opt. Soc. Am. B **19**, 2391–2395 (2002).

- *Production and characterization of spiral phase plates for optical wavelengths*, S. S. R. Oemrawsingh, J. A. W. van Houwelingen, E. R. Eliel, J. P. Woerdman, E. J. K. Verstegen, J. G. Kloosterboer, and G. W. 't Hooft, Appl. Opt. **43**, 688–694 (2004).

- *Half-integral spiral phase plates for optical wavelengths*, S. S. R. Oemrawsingh, E. R. Eliel, J. P. Woerdman, E. J. K. Verstegen, J. G. Kloosterboer, and G. W. 't Hooft, J. Opt. A **6**, S288–S290 (2004).

- *Violation of local realism in a high-dimensional two-photon setup with non-integer spiral phase plates*, S. S. R. Oemrawsingh, A. Aiello, E. R. Eliel, G. Nienhuis, and J. P. Woerdman, arXiv:quant-ph/0401148 v4 (2004).

- *How to observe high-dimensional two-photon entanglement with only two detectors*, S. S. R. Oemrawsingh, A. Aiello, E. R. Eliel, G. Nienhuis, and J. P. Woerdman, Phys. Rev. Lett. **92**, 217901 (2004).

- *The intrinsic orbital angular momentum of paraxial beams with off-axis imprinted vortices*, S. S. R. Oemrawsingh, E. R. Eliel, G. Nienhuis, and J. P. Woerdman, J. Opt. Soc. Am. A (2004), to appear.

107

- *A two-detector measurement of beyond-Bell photon pairing*, S. S. R. Oemrawsingh, X. Ma, D. Voigt, E. R. Eliel, G. W. 't Hooft, and J. P. Woerdman, in preparation for submission to Nature.

Curriculum vitæ

Sumant Sukdew Ramanujan Oemrawsingh werd op 12 juni 1977 geboren in Paramaribo, Suriname. In 1995 behaalde hij zijn diploma aan het Stedelijk Gymnasium te Leiden en begon aansluitend aan de studie natuurkunde aan de Universiteit Leiden, waar hij in 1996 zijn propædeuse behaalde. In 1999 studeerde hij af in de experimentele natuurkunde. Het afstudeerproject, onder leiding van dr. N. J. van Druten en prof. dr. J. P. Woerdman, behelsde de transversale mode formatie in microlasers onder invloed van twee verschillende golfgeleiders in een trilholte.

In september 1999 trad hij in dienst van de Stichting Fundamenteel Onderzoek der Materie (FOM), om promotieonderzoek te verrichten in de groep 'Quantum Optics & Quantum Information' onder leiding van prof. dr. J. P. Woerdman. Het onderwerp betrof de verstrengeling van ruimtelijke vrijheidsgraden van fotonen en viel aanvankelijk onder directe begeleiding van dr. S. F. Pereira, na één jaar overgenomen door dr. E. R. Eliel. Het proefschrift bevat de resultaten van dit onderzoek.

Nawoord

Uiteraard is dit proefschrift tot stand gekomen met de hulp en inbreng van meerdere mensen, die ik bij deze graag wil bedanken. Het experiment zou niet eens bestaan zonder de mensen van de Fijnmechanische Werkplaats. Met name zou ik Ewie de Kuiper en Koos Benning willen bedanken, voor wie het gecompliceerde apparaat in fig. 8.8 nog maar een koud kunstje was. Natuurlijk waren ook Arno van Amersfoort, René Overgauw en Leendert Prevo onmisbaar met hun kennis over elektronische apparatuur en computers. Voor administratieve problemen en 'vraagjes' kon ik altijd vertrouwen op de behulpzaamheid van Anneke Aschoff en Henriette van Leeuwen.

Veel van het experimentele werk werd verlicht door de aanwezigheid en inbreng van de studenten Jasper Kok, tijdens zijn korte IEN periode, en Wouter van Drunen, Jeroen van Houwelingen en Xiaosong Ma, tijdens hun laboratorium stage.

De aangename sfeer, en later ook de leuke filmavonden, werden mogelijk gemaakt door mijn collega promovendi, Krista Joosten, Alexander van der Lee, Marnix Willemsen, Steven van den Berg, Yngve Lien, Jos Dingjan, Hayk Haroutyunyan, Javier Loaiza, Jorrit Visser, Erwin Altewischer, Thijs Klaassen, Peter Lee, Nikolay Kuzmin en Graciana Puentes. Ook wil ik de post-docs hartelijk bedanken. Mijn experimentele vaardigheden heb ik geleerd van Klaasjan van Druten tijdens mijn afstudeerperiode en van Silvania Pereira, die mij begeleidde in het begin van mijn promotieonderzoek. Sergio Dutra stond altijd klaar om zijn kennis te delen, met Andrea Aiello had ik vele interessante discussies over parabolen en spirografen, Cyriaque Genet filosofeerde graag met mij over van-alles-en-nog-wat en met Dirk Voigt's hulp en inbreng heb ik het belangrijkste experimentele resultaat van dit proefschrift behaald.

Tot slot wil ik mijn zus Sangini en mijn moeder bedanken, die mij altijd gesteund en gestimuleerd hebben.

111